Detection and Classification of Power System Disturbances Using Discrete Wavelet Transform and Pattern Recognition

By

Aminat Rasheed

in partial fulfilment of the requirements for the degree of

Master of Science
in Electrical Engineering

at the Delft University of Technology,
to be defended publicly on Wednesday August 14, 2019.

Supervisor: Dr. ir. M. Popov
Thesis committee:
Prof. dr. P. Palensky, IEPG, TU Delft
Dr. M. Ghaffarian Niasar, DCE&S, TU Delft
Dr. Jose Chavez, IEPG, TU Delft

TU Delft

Acknowledgement

My sincere appreciation goes to my supervisors Prof Marjan Popov and Dr. Jose Chavez for their support and guidance during this project. I would also like to use this opportunity to thank my committee members and everyone that has contributed to this research directly and indirectly, I am very grateful. To my ever-supportive friends and colleagues, I say a very big thank you! You have been very supportive all through the way and I am grateful for all your encouraging words in making the whole process memorable.

And to my family members for their unending support, love and sympathetic ears, you guys rock! May God continue to bless you.

Aminat Rasheed
Delft, August 2019

Abstract

In order to enhance the reliability of power systems, a continuous monitoring of the network to detect and clear disturbances is crucial. Fast detection and isolation of disturbances can prevent equipment damage, downtime and other adverse effects associated with their occurrence. The focus of this project is on the detection and classification of two non-linear, complex and severe disturbances: ferroresonance and arcing faults. These disturbances are detected and classified by continuous signal processing of the three-phase voltage and current signals. The models of these disturbances are simulated in EMTP and the three-phase voltage and current are extracted. The extracted data are pre-processed using the discrete wavelet transform (DWT) to extract fault signatures and features used in classifying the disturbances. A decision tree classifier is trained with the extracted features and it is able to detect and classify a disturbance as either ferroresonance or arcing faults using an adaptive time based on the disturbance class. The computational burden in the detection and classification process is reduced by using the superimposed component of the voltage and current to detect transient inceptions prior to classification. Adaptive dead time is adopted to classify the sustained period of the ferroresonance signals and to detect the extinction time of the secondary arc. The results show that the proposed methodology can detect the different ferroresonance modes and arcing faults with 99.8 % accuracy within 100 ms and classify the sustained modes afterwards.

Contents

List of Figures

List of tables

1 Introduction

The power system is one of the oldest and the most complicated man-made system on earth. Due to the demand for greener and more sustainable ways of generating electricity, the system is currently undergoing a lot of changes. The dependence on electricity for virtually all our day to day activities necessitate continuous development in power system to ensure continuity of supply, a reliable and resilient network. Power systems protection is a branch of electrical power engineering in charge of protecting the power systems against faults by isolating the faulty part from the rest of the network to prevent down times and blackouts. The protection devices misoperation can have catastrophic impacts on power system infrastructures and personnel, in some cases may result in a cascade event ending in a large blackout. As more renewable energy sources are integrated into the power system, the dynamics of the system is changing, and the traditional protection devices and schemes need to be faster, more resilient and adaptive in order to ensure continuous supply of electricity and reliability of the network grid.

The impact of a disturbance on power systems network is dependent on the event nature, the voltage level at which it occurs and the impact on the connected network downstream. Although the power system is protected by primary and back up relays, some disturbances are not easily identified. Integration of distributed energy sources into the power network is growing and expected to grow in the future, the power network must be able to handle all kind of disturbances to ensure continuity of service to the users. A resilient monitoring system is therefore needed to complement the action of protection relays and to securely protect the network from disturbances. In this project, severe disturbances like ferroresonance and arcing faults are investigated and classify within few cycles from their occurrence. This is necessary because the traditional protection devices are unable to detect short circuits caused by arc fault early enough to prevent electric fire [1].

Ferroresonance is a non-linear and a complex disturbance caused by the interaction between the non-linear inductance in the network and the capacitance. The transformers in the network are more vulnerable to this disturbance due to the high non-linear magnetizing inductance of the transformer core. The occurrence of this disturbance is unpredictable due to its non-linear and random behavior, it jumps from one state to other [2]. Another interesting aspect of ferroresonance is that a physical capacitance is not necessary for its occurrence, it could be a stray capacitance in the network [3]. It is usually initiated by changes in the network due to switching actions, however, the same network parameter can give different steady-state modes of ferroresonance due to its non-linear nature. The disturbance is associated with high sustained overvoltage and overcurrent in some cases due to saturation of the transformer core. Consequently, the whole network downstream of the transformer will be affected and this can cause a huge revenue loss to consumer and electricity system operators. Increase penetration of power electronic controlled renewable energy sources could increase the capacitive elements in the network and makes the network more vulnerable to ferroresonance.

Other interesting disturbance in power systems is an arc fault. A lot of research has been conducted in understanding this phenomenon. Although an electric arc is necessary for switching operation in a power system, an undesired arc sustained with enough voltage and current, can cause destruction of equipment, insulation breakdown and fire in some cases. In this thesis, a method that can detect ferroresonance and an arcing fault is proposed. The methodology can classify different modes of ferroresonant oscillations and arcing faults. This method is based on fast wavelet transform and pattern recognition algorithm.

1.1 Motivation for the research

In power system, there are protection relays to detect and trip in case of classical faults, however cases with highly irregular electrical signals like ferroresonance can go undetected if the system survives the disturbance. Sustained disturbance without detection could cause overcurrent and overvoltage that can damage electrical equipment. In some of the ferroresonance cases reported in the literature, the high sustained overvoltage leads to damage of the transformer. Once the ferroresonance is in sustained mode, there is a continuous overvoltage and overcurrent with a high distortion until the connected equipment is damaged when the source is not isolated on time. Ferroresonance can be prevented by providing adequate damping in the network and switching off the voltage source. Therefore, on-time detection of this disturbance can prevent equipment damage and stress due to sustained overvoltage and overcurrent.

Majority of the faults on transmission network are single-phase to ground faults [4] and usually associated with arcing. Understanding of the dynamic arc interaction with the power systems can help in improving the detection method of this disturbance. Investigation of arcing faults, especially the secondary arc characterized with low current can helps in coordination of a single-phase auto-recloser (SPAR). Real-time monitoring of these disturbances can help in maintenance activities. If the occurrence of disturbance is undetected, it will be difficult to provide a mitigating action or preventive measures. Even though the awareness about disturbances occurrence can help the operators to perform corrective actions, knowing the non-failure modes disturbances give an insight on how to manage the event and preventive maintenance planning. Therefore, this demands classification of these disturbances.

Most of the disturbance detection schemes in literature either focus on the classification of classical faults, power quality classification, ferroresonance or arcing, none focuses on the classification of these two transients with the same algorithm. Protection relays in the network can isolate classical faults but no relays have been developed to detect and clear ferroresonance disturbance based on author's knowledge. These factors motivated this thesis work to achieve the objectives discussed in the next section.

1.2 Research Objectives

The main objective of this project is to develop and algorithm that takes the three-phase voltage and current at the bus node to detect non-linear disturbances like ferroresonance and arcing within 5 cycles from their occurrence. Another objective of this research is to investigate different modes of ferroresonance, primary and secondary arcing faults. Understanding of these disturbances is necessary to develop a robust detection schemes and classify the modes correctly. The developed algorithm will be assessed for real-time implementation. This research will contribute to the development of a resilient monitoring system for power system disturbances. These objectives are achieved by:

- Modeling of different ferroresonance modes in ATPDraw (Alternative Transient Program), an Electromagnetic Transient Program (EMTP).
- Modeling of primary and secondary arcing faults in ATPDraw and analysis of different arc models.
- Extraction of different data combination of ferroresonance and arcing model in EMTP.
- Analysis of voltage and current waveform with discrete wavelet transform to extract features for classification.

- Develop a classification algorithm using supervised learning scheme: decision tree, support vector machine and k-nearest neighbour.
- Offline development of the algorithm for real-time classification.

1.3 Methodology

The first phase of this project is modeling of ferroresonance and arcing faults in ATPDraw to extract data (electrical variables). The next phase, detection and classification, is achieved by applying wavelet transform and machine learning to the extracted data. This phase is divided into three sections: Pre-processing or signal analysis stage, detection stage and classification stage. The offline training of the classification algorithm is done in MATLAB. The online scenario is simulated with a for-loop in MATLAB to observe the performance of the algorithm. Figure 1.1 shows the step-by-step approach of the methodology.

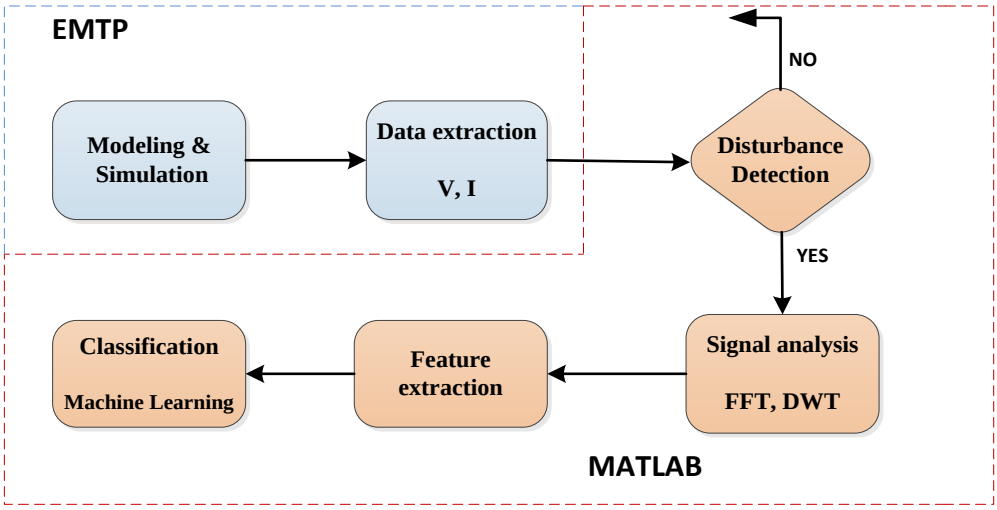

Figure 1.1: Flow chart of the proposed methodology

Three phase models of ferroresonance and arc fault are developed in ATPDraw and the parameters of the network are changed to generate different scenarios. Then, the three-phase voltages and currents are extracted from the different simulated cases. In order to ensure the algorithm can be implemented in real-time application, the system is assumed to be a causal system with only the present and saved past values known. One cycle of the previous data samples is saved and analyzed at a time to reduce memory space. The signal analysis stage is achieved with both Fast Fourier transform (FFT) and Discrete Wavelet Transform (DWT). The FFT is used for initial classification of the different modes of ferroresonance and spectral component analysis of arcing fault signals. This helps in determining the section (steady-state, transient and sustained period) of the data samples to analyze for different ferroresonance modes.

The superimposed component, change in current and voltages, are used as the fault signatures to determine the inception of transient before classification of the disturbances. In order to reduce the computational burden and save memory, the classifier is activated when a disturbance is detected. An algorithm for wavelet decomposition is developed in MATLAB to obtain the coefficients used in extracting features for the classification algorithm. In addition, the high time resolution of the DWT is used for time localization of the disturbances. An algorithm is developed for feature extractions and database generation. The extracted features from manipulation of the DWT are labeled and then used as an input to train the classification algorithm. The trained classifier then processes new data and classify the disturbances into their corresponding classes. The classification process is further optimized to

reduce redundant data (repeated classification) by using an adaptive dead time during the real-time simulation with a for-loop in MATLAB.

1.4 Outline of Thesis

The background of this thesis work, the objectives, the motivation and the contributions are discussed in Chapter 1. For correct detection and classification, detailed models of the disturbances are needed due to non-availability of real measurements. The modeling and simulation of ferroresonance is discussed in Chapter 2. While the detailed modeling and literature review of arcing faults are explained in Chapter 3. The spectral analysis of the signal is essential in order to obtain disturbance signatures for the classification algorithm. Pre-processing of the extracted data from the simulation file is also needed for separation of steady-state and transient state. The signal processing techniques used in this thesis are explained in detail in Chapter 4. In addition, the feature extraction and selection are also explored and discussed in Chapter 4. Once the disturbance has been successfully detected, the classification algorithm is activated. The detection and classification technique used in this thesis are explained in Chapter 5. The optimization approach to reduce computational burden are also discussed. Chapter 6 presents the conclusions, recommendations and future work.

1.5 Contribution of the thesis

The main contribution of the thesis work is the development of an advance algorithm to detect and classify power system disturbances using the three-phase voltage and current from the network within 5 cycles. A single algorithm that detects the occurrence of ferroresonance and arcing faults using the system voltage and current and classify the fault using machine learning is developed. The algorithm is also assessed for real-time implementation. A detailed model of a primary and a secondary arc and different arc models are also explored in this thesis. In future, more disturbances are expected to be analyzed by this algorithm. A template for generating new datasets in order to increase the type of disturbances the algorithm can detect is also developed in this thesis.

2 Ferroresonance - Modeling and Simulation

Ferroresonance, as the name suggests, is a resonance condition between the capacitive element in the network and a non-linear inductance of a ferromagnetic equipment like a transformer and a reactor. This non-linear oscillating phenomenon is due to the interaction between the non-linear inductance and the capacitance element in the network. Unlike the linear resonance which is with a deterministic frequency of oscillation, ferroresonance is a complex, a non-linear and an unpredictable resonant condition. The frequencies of oscillation are not deterministic and depend on the initial operating conditions. This disturbance is likely to occur when a non-linear inductor is fed with a capacitive element in series. The major difference between a linear resonance and a ferroresonance state is the non-linear attribute of the inductor, the inductance is not constant during the resonant condition. As such, different ferroresonance modes can occur with a different capacitance value and a source frequency. The behavior has several possible solutions and can occur in transmission and distribution networks irrespective of the voltage level. The capacitance needed for ferroresonance occurrence could be the grading capacitance of the breaker, the stray capacitance to the ground, the compensation capacitance (capacitor banks), the capacitance of the transmission lines and cables etc. The different forms of capacitance mentioned above are readily available in power system as well as non-linear inductance like transformer core. Therefore, a proper study should be done considering different network configurations during the planning phase of a power system expansion/development to ensure the system is ferroresonant free. The traditional power systems is not fully protected against ferroresonance and this disturbance may affect the operation of the relays. Moreover, the surge arrestor might not be able to withstand the high overvoltage for a long time when the disturbance occurs [5].

Ferroresonance does not happen out of the blue, it is usually triggered by changes in network topology like switching, power system faults occurrence or clearance of faults. This disturbance is usually associated with high overvoltage and overcurrent that can cause equipment damage and undue stress on the insulation. High harmonic contents, especially the odd harmonics, are usually produced and injected into the network when a fundamental ferroresonance occurs. If the source of the ferroresonance is not switched off, this sustained overcurrent due to transformer saturation can cause overheating of the transformer and could subsequently cause explosion of the transformer. Therefore, ferroresonance could be a threat to security of supply of electricity.
In this chapter, a three-phase model of a ferroresonant circuit used for simulating different modes are discussed. The impact of parameter changes on the modes of the ferroresonance are also explained. Different network configurations that could cause ferroresonance are highlighted, and the mitigating factors to prevent its occurrence are discussed.

Depending on the network topology, resonance could be parallel or series. A series resonance is excited by a voltage source while a parallel resonance is excited by a current source. Even though the power systems is entirely supplied by voltage source, the source could act like a current source when a voltage source is placed behind a high resistance. A typical series linear resonant and ferroresonant circuits are shown in Figure 2.1 and Figure 2.2 respectively. For a linear resonant circuit, the resonance occurs when the system is tuned to the natural resonant frequency of the circuit. By applying Kirchhoff law,

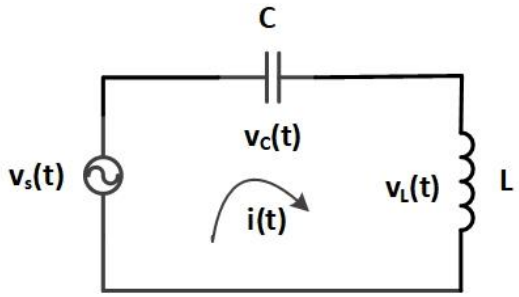

Figure 2.1: Series resonant circuit

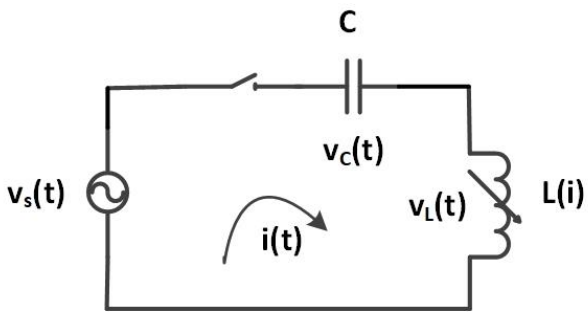

Figure 2.2: Ferroresonant circuit

during the steady-state condition, equation (2.1) is valid.

$$V_s = I \cdot \left(\omega_s L - \frac{1}{\omega_s C}\right) = I \cdot \ (X_L - X_C) \tag{2.1}$$

During the resonance condition, the capacitive and inductive reactance are equal assuming zero damping in the circuit. The resonant frequency can thus be computed as:

$$f_R = \frac{1}{2\,\pi\sqrt{LC}} \tag{2.2}$$

The circuit is more capacitive when the source frequency f_s is less than the system frequency while the inductive reactance, X_L dominates when $f_s > f_R$, resonant frequency is less than the system frequency. The magnitude of the voltage across the L and C reach their peak at resonant, with their values greater than the source voltage. In contrast, ferroresonance does not occur at a fixed frequency. The non-linear inductor can have different values during transformer saturation period. This implies that different capacitance values can potentially cause ferroresonance at a given frequency [6]. Replacing the linear inductance in Figure 2.1 with a non-linear inductance gives a ferroresonant equivalent circuit. Similar analysis can be applied to this case in order to determine the operating point of the circuit. During the steady-state operation at the power frequency, the equation of the circuit in Figure 2.2 ignoring the losses is given as:

$$V_s = I \cdot X_L(I) - \ I \cdot \frac{1}{\omega_s C} \ = I \cdot X_L(I) - I \cdot X_C \tag{2.3}$$

where: X_c is the circuit reactance at power frequency, $X_L(I)$ is the current dependent variable reactance of the ferromagnetic material.

The non-linear reactance $X_L(I)$ of the saturable magnetic core is a function of the current and depends on the number of turns and the dimension of the core [3]. The flux linkage versus current waveform is shown in Figure 2.3 while the graphical solution to equation (2.3) is shown in Figure 2.4.

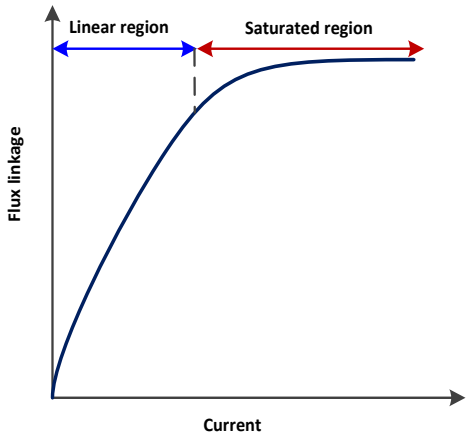

Figure 2.3 Flux vs current characteristics of ferromagnetic material

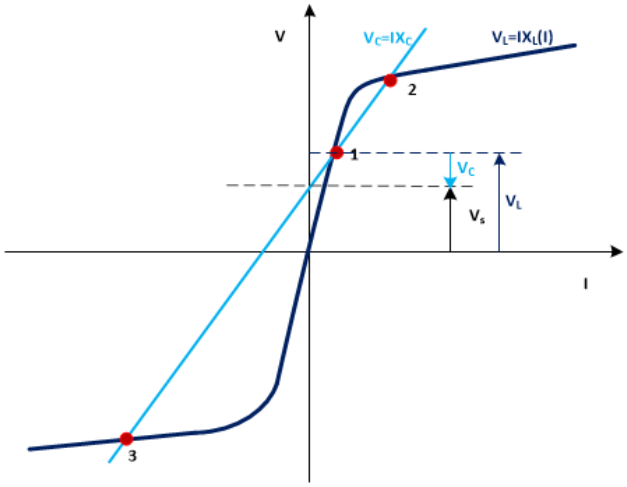

Figure 2.4 Graphical solution of series ferroresonant circuit

Three possible states: state 1, 2, and 3 can be identified in Figure 2.4. Point 1 in the graph represents the linear region of operation of the magnetic core. This represents a steady-state operation of the circuit in which the relationship between the voltage and the current is linear. The voltage across the non-linear inductor, V_L is the sum of the supply voltage and the capacitive voltage, $V_s + V_C$ as seen in Figure 2.4. The circuit is inductive in this case. A slight increase or decrease in the current leads to high change in inductive voltage due to its steepness and also a small change in capacitive voltage. In order to find the equilibrium point, the current will return to its original value.
The second possible solution is the point marked 2 on the graph. This point is the unstable point of operation. A small change in the current leads to a high capacitive voltage but slight increase in inductive voltage. The steepness in capacitive voltage is not balanced by the inductive voltage, so the current will keep increasing or decreasing away from the point depending on the direction of the initial change.
The third solution is the point marked 3 on the graph. This is the non-linear point of operation of the circuit. The capacitive voltage is the sum of inductive voltage and the source voltage. This state is the ferroresonant state and it's also stable. Equilibrium is maintained in a similar way to point 1.

2.1 Literature Review on Ferroresonance

Different studies have been carried out in understanding ferroresonance phenomenon in power systems since the word was coined in 1920 by P Boucherot [7]. The different circuit configurations that are vulnerable to ferroresonance occurrence are discussed in [8] including experimental and real life cases. In order to correctly detect this disturbance and the different modes of the sustained period, an accurate modeling of the circuit parameters especially the transformer is paramount. Detailed modeling of the elements of a ferroresonant circuit is discussed in [6]. The transformer, the transmission lines and other circuit parameters are very important in initiation of ferroresonance. Analysis of ferroresonance using bifurcation diagram and Poincare plot are discussed in [6], these graphical representation give additional criteria for classifying ferroresonance modes in conjunction with the periodicity of the signal. Ferroresonance can occur at any voltage level provided the basic elements needed in a ferroresonant circuit are present. More explanation on the analytical approach of ferroresonance can be found in [3] while the detailed explanation of the phenomenon is discussed in [9]. A detailed explanation of ferroresonance occurrence is provided in [9, 10]. A case study of ferroresonance occurrence on the low voltage side of a transformer in a 22 kV PV system distribution network is discussed in [11]. Similar to the medium voltage (MV) and high voltage (HV) cases, the occurrence depends on the network parameters and sudden changes in the network like switching events. Ferroresonance affected the step-

up transformer used for the grid connection of the 500 kW rooftop PV network during a single phase switching. However, ferroresonance does not occur when all the three phases were switched together. Increasing the PV installed capacity, the capacitance of the transmission line, the distribution transformer (ferromagnetic) and single-phase switching can cause ferroresonance on the LV side of the transformer.

One of the major reasons why this disturbance is studied is to detect its occurrence on time and provide mitigating solutions to reduce its impact on the network. The mitigating solutions to this disturbance has also been discussed in literature. Suppression of ferroresonance with a shunt reactor is investigated in [12]. Increasing the damping or introduction of damping also helps in limiting the vulnerability of power systems to ferroresonance as discussed in [10]. Some of the mitigating factors are case specific depending on the network arrangement susceptible to ferroresonance.

Similarly, research has been done on the detection of ferroresonance in power systems and classification from other switching transients like capacitor switching, transformer switching and load switching. Geev Mokryaniet al. in [13] used Stockwell transform, S-transform, for feature extraction and support vector machine (SVM) for distinguishing this disturbance from other transients. The authors in [14, 15, 16] used discrete wavelet transform for signal decomposition and feature extraction. However, the author in [17] used Multi-Layer Perceptron (MLP) for classification, Learning Vector Quantizer(LVQ) neural network was used in [14] while decision tree was used in [15]. The application of wavelet transformation for detection of ferroresonance is discussed in [2, 16]. The approach discussed in [16] is not robust enough to classify ferroresonance modes. Moreover, wavelet decomposition presents a high value at the inception of all transients and not unique to only ferroresonance occurrence.

Most of the methods discussed above focused on distinction of ferroresonance from other transients' conditions, however, the classification of the different modes of ferroresonance is explored and implemented in this thesis work. The detailed explanation on the approach is explained in Chapter 5.

2.2 Impact of Ferroresonance Occurrence on Power System

Ferroresonance, like other disturbances has negative impacts associated with its occurrence on power systems. The most common impacts discussed in literatures are highlighted below:

- Overvoltage and overcurrent.
- Overheating of the transformer core due to saturation and high current.
- Equipment failure due to high stress.
- Insulation and dielectric breakdown due to a high sustained overvoltage and overcurrent.
- Highly distorted waveform with large harmonic and subharmonic contents affect power quality.
- Loss of supply due to equipment breakdown. This can also affect the reliability of the network as well as the security of supply.
- Low humming noise due to occurrence of ferroresonance. The operators noted a loud noise when a fundamental ferroresonance of 2 p.u. occurred due to switching of a line in 400 kV substation as reported in [18].
- Explosion of a transformer due to sustained fundamental ferroresonance has also been reported in [19]. This was caused by energization of a potential transformer at the de-energized bus bar through the grading capacitance of the circuit breaker of a live bus bar. The sustained high current on the primary side of the transformer resulted to this failure.

Even though surge arrestors can surge the overvoltage in power system, long sustained overcurrent and overvoltage of ferroresonance disturbance can destroy the arrestor due to overloading. Over rating the surge arrestor could prevent its damage but this also increases the chances of damaging other components in the network due to ferroresonance overvoltage. This also reduce the protection level of the system to lightning overvoltage. These negative impacts necessitate fast detection of ferroresonance and isolation of the disturbance before causing damages to the electrical equipment. Knowledge of the modes of ferroresonance could also help in planning and maintenance activities to reduce its likelihood of occurrence and/or prevent future occurrence.

One practical example of ferroresonance caused by the interaction of a shunt capacitor bank with the non-linear inductance of an unloaded or lightly loaded transformer is depicted in Figure 2.5. This case shows a possible occurrence of ferroresonance when one or two phases of the three packs of single-phase transformer are disconnected or switched. The neutral path in the figure provides the connection between the circuit capacitance and the inductance. The zero-sequence path from the capacitor bank and the source are coupled together and this provides path from the closed phase C (potential external energy source in this case) to the open phase A and B through the transformer core to the capacitor bank. Therefore, a complete loop is formed.

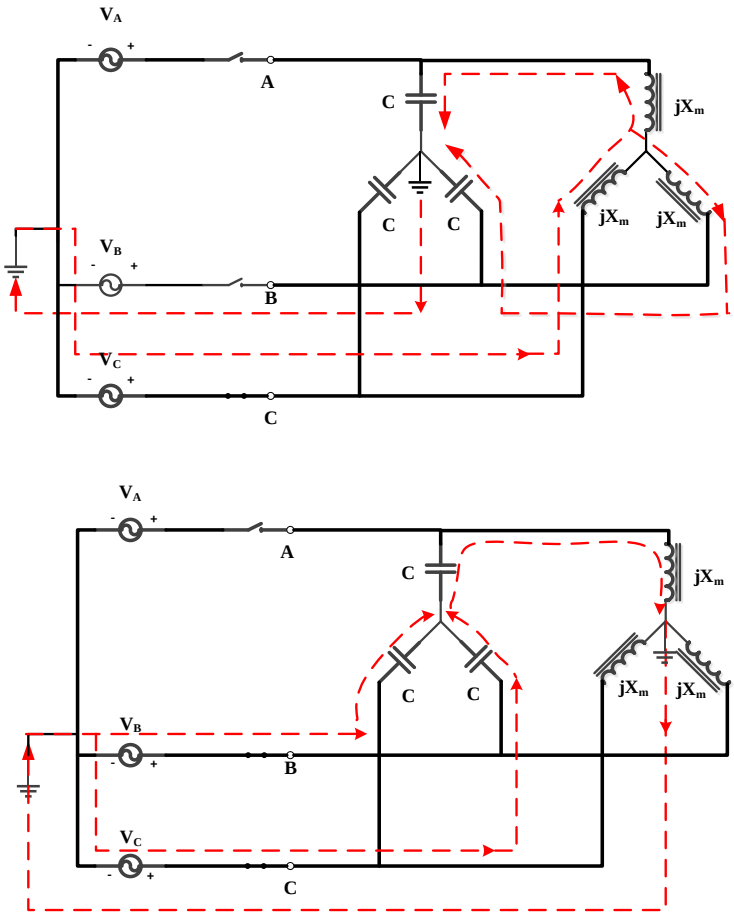

Figure 2.5 Possible ferroresonance connection with shunt capacitors

In the second part of Figure 2.5, the neutral connection is on the transformer side. The path is dependent on the arrangement of the network elements and construction of the transformer core. The influence of neutral connection and transformer core construction are not be investigated in this thesis.

2.3 Types of ferroresonance

Similar to the linear resonant circuit, ferroresonance could also be parallel or series one depending on network configuration. However, the series resonant condition is more common in the transmission network while the parallel is common in the distribution network with ungrounded or resonant neutral connection [3]. Only the series ferroresonance is considered and analyzed in this thesis. Ferroresonance can be divided into two stages: the transient period that last for few cycles and the sustained period that continues until the feeding source is switched off [2]. The waveform of the transient period is affected by the circuit parameters while the sustained period is similar for the same modes of ferroresonance. Figure 2.6 shows a ferroresonance waveform and different sections: steady-state period, transient period and sustained period. The sustained period of the ferroresonance is what is classified into different modes and these modes are discussed in the subsequent section.

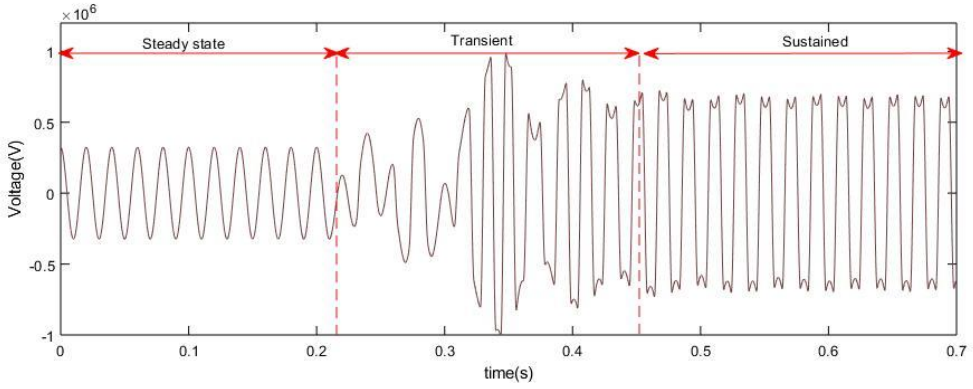

Figure 2.6 Ferroresonance partition

2.4 Different Modes of Ferroresonance

Ferroresonance classification into different modes is based on the sustained period of the disturbance. It can be classified using the sustained current and voltage waveform; most especially by using the spectral components of the voltage waveform in the sustained period. The periodicity of the waveform and the frequency composition are used for the classification. Figure 2.7 shows the different modes of ferroresonance based on the periodicity and the frequency spectrum. The classification method in CIGRE report on resonance and ferroresonance in power networks [3] is adopted in this thesis.

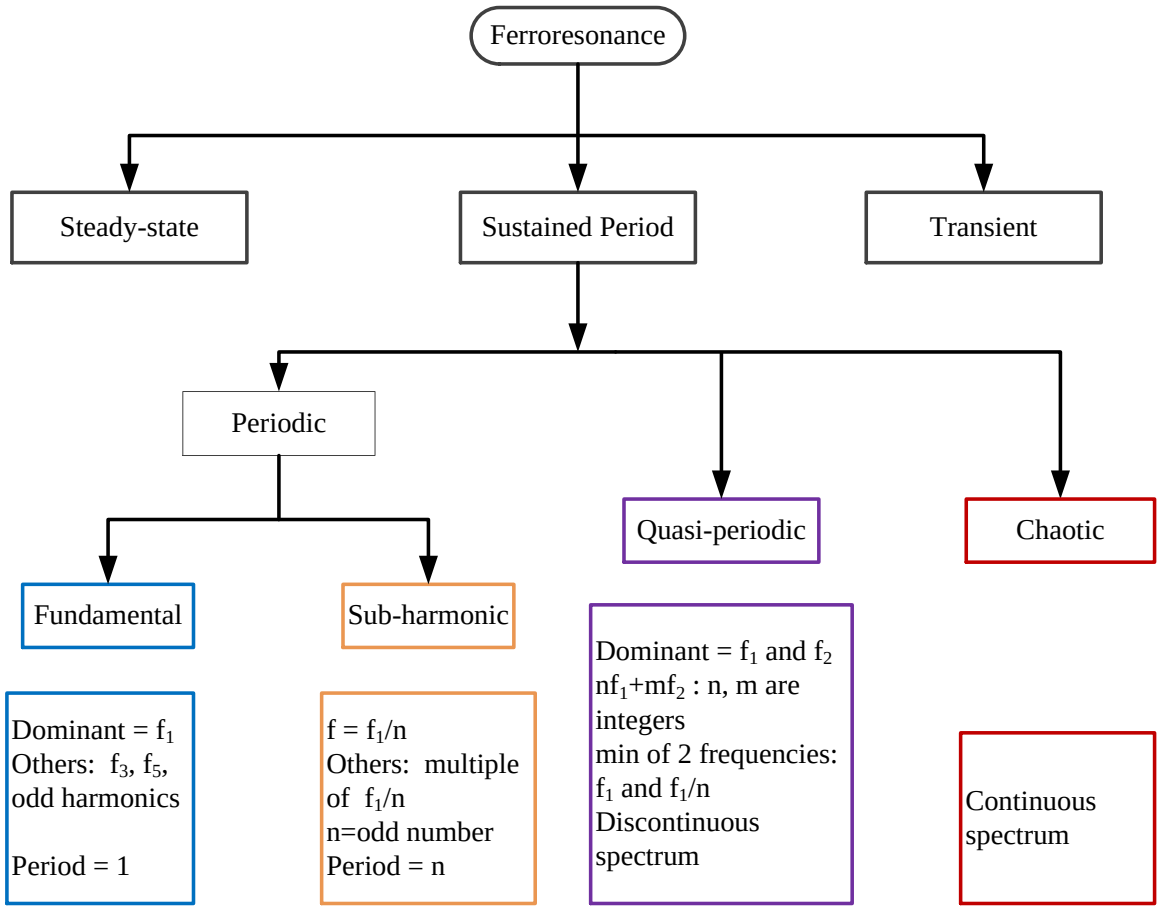

Figure 2.7 Classification of ferroresonance modes

The mode of ferroresonance is dependent on the point of operation or intersection of the other circuit properties (voltage and current of other circuit parameters) with the saturation curve of the transformer. The first level categorizations are the periodic and the non-periodic ferroresonance as shown in Figure 2.7. In a periodic ferroresonance mode, the waveform repeats in a definite pattern and the frequency of oscillation could be a multiple or a sub multiple of the fundamental frequency. The non-periodic modes are the quasi-periodic and the chaotic modes of oscillation. Quasi-periodic ferroresonance oscillation is not periodic, it has a minimum of two frequencies which are the fundamental frequencies and lower subharmonic frequencies. It continuously shifts between periodic modes without settling to anyone. Chaotic ferroresonance has an unpredictable waveform and a continuous frequency spectrum. It is sometimes studied with chaos theory. Overvoltage and overcurrent are the major problems associated with the fundamental ferroresonance while the subharmonic mode has voltage usually less than the system voltage. However, the subharmonic components could affect the operation of electronic devices. The amplitude of the current in this mode is also less than in the fundamental mode. The spectral components of the different modes are discussed below.

2.4.1 Fundamental Ferroresonance

The dominant frequency is the fundamental frequency of the grid and it is usually accompanied by other harmonics that are odd multiple of the fundamental frequency, 3rd, 5th etc. The voltage magnitude is usually higher than the rated voltage of the system and could cause a high stress on the equipment if not isolated on time. Figure 2.8 shows a typical fundamental ferroresonance voltage waveform obtained from simulation while Figure 2.9 shows a generic frequency spectrum.

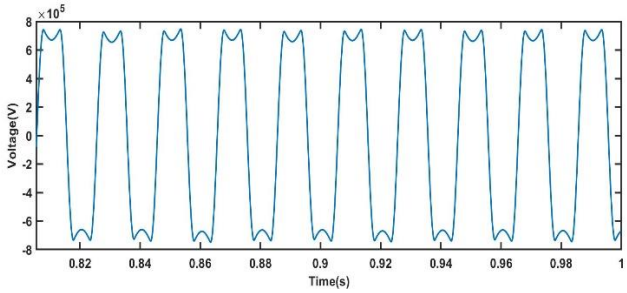

Figure 2.8 Example of fundamental ferroresonance voltage waveform

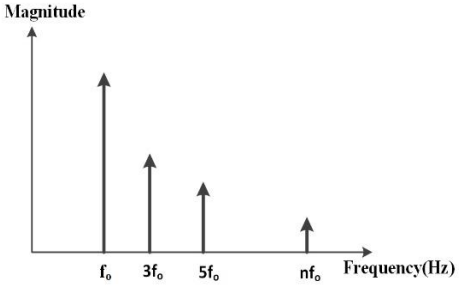

Figure 2.9 Typical fundamental ferroresonance frequency

2.4.2 Chaotic Ferroresonance

The chaotic ferroresonance has a broad band frequency spectrum with an unpredictable behavior. It has sharp peaks at system frequency and a continuous frequency spectrum. The time domain signal is not periodic and has no definite shape or pattern. According to [3], it is not a common ferroresonance mode in power system and no practical case has been reported so far in extra high voltage (EHV) substation. It is only predicted in literature and Figure 2.10 shows the voltage waveform. As explained above, the frequency spectrum is broad with peaks at fundamental and subharmonic frequencies. The frequency spectrum is shown in Figure 2.11.

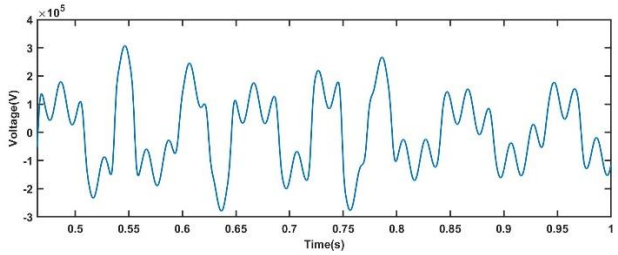

Figure 2.10 Chaotic ferroresonance voltage waveform

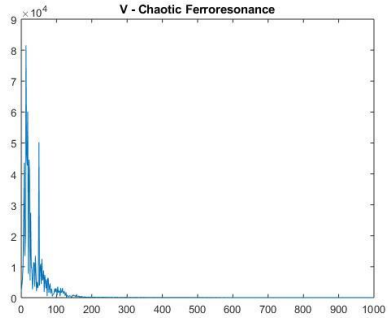

Figure 2.11 Chaotic ferroresonance frequency

2.4.3 Subharmonic Ferroresonance

The subharmonic ferroresonance mode is also periodic but has a longer period of oscillation than the grid. It has harmonics which are usually odd sub-multiple of fundamental frequency $\frac{f_o}{n}$. f_o is the fundamental frequency, 50 Hz in this case and n is an integer that determines the period of the subharmonic ferroresonance. For instance, if the dominant frequency is $\frac{f_o}{n}$, the subharmonic mode is period-n. The spectrum is also discontinuous. Figure 2.12 shows a typical subharmonic ferroresonance voltage waveform while Figure 2.13 shows a generic frequency spectrum.

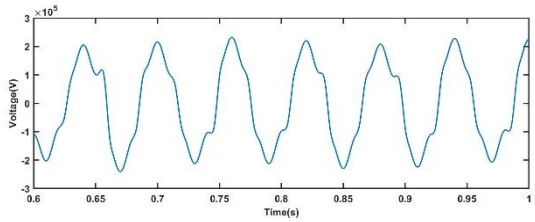

Figure 2.12 Subharmonic ferroresonance voltage waveform

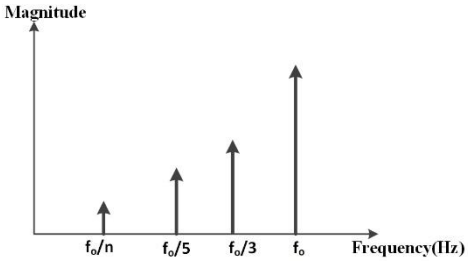

Figure 2.13 Subharmonic ferroresonance spectrum

2.4.4 Quasi-periodic

The quasi periodic fundamental ferroresonance is not totally chaotic and neither is it periodic. It has a combination of the fundamental and the subharmonic frequencies in its frequency spectrum. There is at least one lower subharmonic mode in combination with the fundamental frequency. It has a discontinuous frequency spectrum. Figure 2.14 shows a typical subharmonic ferroresonance voltage waveform while Figure 2.15 shows a typical frequency composition.

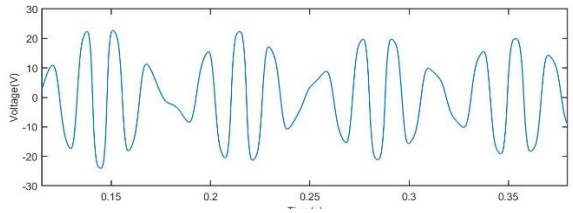

Figure 2.14 Quasi-periodic ferroresonance voltage waveform

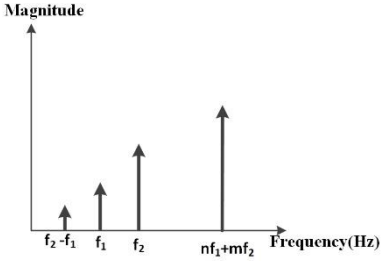

Figure 2.15 Quasi-periodic ferroresonance spectrum

Ferroresonance does not need an external source to occur. The charge stored in the capacitor in a ferroresonant circuit could sustain the oscillation for some periods depending on the period of oscillation of the disturbance. The voltage magnitude of the oscillation is damped out after every polarity change due to a high circuit loss when the transformer is saturated. Introduction of an external energy source represented by $v_s(t)$ in Figure 2.2 changes the narration about the oscillation decaying. If the effect of the voltage source and stored capacitive energy exceed the circuit I^2R loss, then the oscillation is sustained indefinitely. The presence of an external voltage source could also affect ferroresonance oscillation frequency. Some examples of the network configurations prone to ferroresonance are:

- Uneven phase operation in a network with shunt compensations.
- Single phase switching in a multi circuit right of way with a shunt compensation.
- Combination of the grading capacitor of a breaker and Voltage Transformer (VT). The grading capacitors of circuit breakers are used for even distribution of voltage after breaking. The grading capacitor supply the energy needed to maintain the sustained ferroresonance.

2.5 EMTP Model of Ferroresonance

The EMTP model used in this thesis is the model of a case reported in Ireland during commissioning test of a line bay in a new 400 kV substation. This ferroresonance case was caused by the energization of the voltage transformers through the grading capacitor of the circuit breaker [18]. A 'live test' was conducted by energizing the voltage transformers through the bus bar as shown in Figure 2.16 with the line disconnector opened. The circuit breaker was then opened to de-energize the line VT's and this

switching sequence results in ferroresonance oscillation. The equivalent ferroresonant circuit of the model is shown in Figure 2.17.

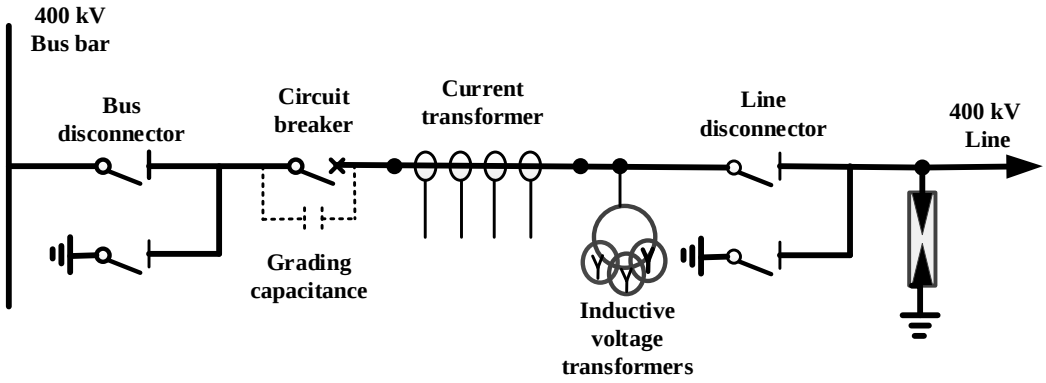

Figure 2.16 400 kV Substation Circuit

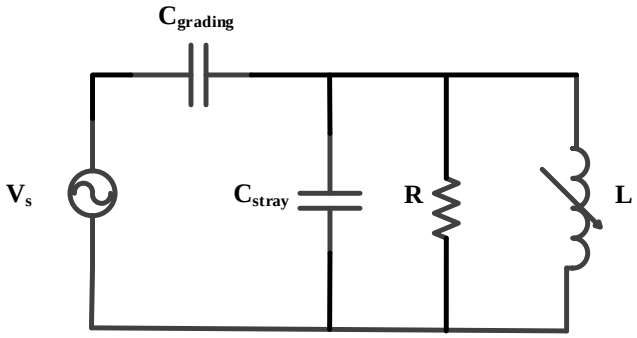

Figure 2.17 400 kV Line Bay Equivalent Circuit

The grading capacitance of the breaker is in series with the 400 kV source. The stray capacitance in the circuit is the disconnected line bay capacitance to the ground. While the magnetizing inductance and the losses of the voltage transformer in Figure 2.16 are represented by R and L respectively in Figure 2.17. The voltage transformer is represented with three single phase VTs with the secondary winding connected in 'Wye' configuration, and the tertiary winding in an open delta closed with 0.5 Ω resistor. The graphical representation of this model in ATPDraw is shown in Figure 2.18. According to [10], for a ferroresonance to occur the following elements are needed based on field experience and research:

- Nonlinear inductance.
- Capacitance.
- Low losses.
- an external source of energy.

The default parameter used in the ATP Model are shown in Table 2-1

Table 2-1 Default circuit element values for fundamental and translational chaotic ferroresonance EMTP model

Source voltage, V_s	324 kV
Grading capacitor	600 pF
Stray capacitor	270 pF
Magnetizing losses	50 $M\Omega$
Switching time of the breaker	0.2078 s

In order to generate difference scenarios, the circuit parameters that influence ferroresonance are changed. Increasing or decreasing each of these parameters has different impacts on the onset of the sustained period, the duration of the transient period and the sustenance or damping of the oscillation.

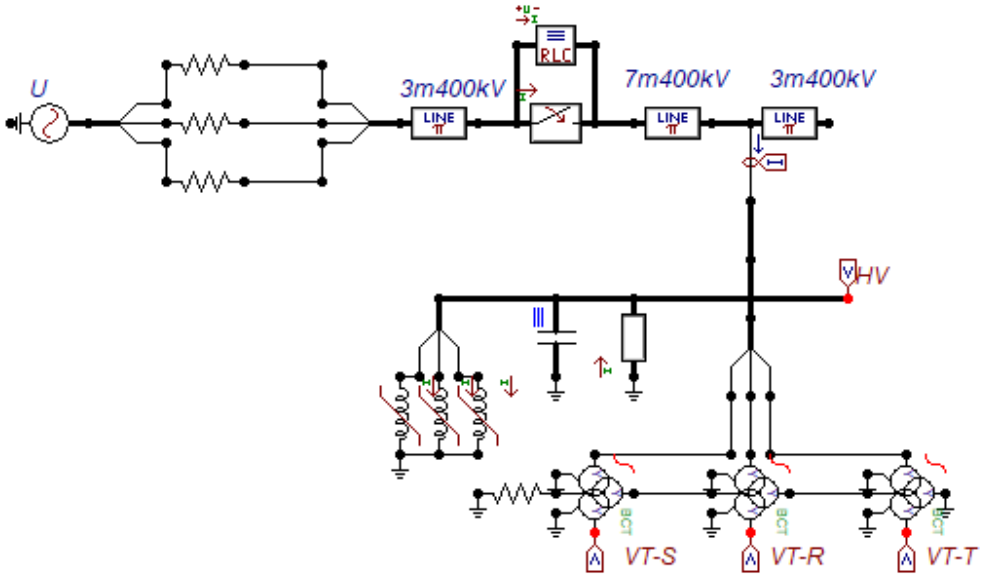

Figure 2.18 EMTP Model: Ferroresonance Circuit

The model in Figure 2.18 is used for investigating the fundamental, the subharmonic and the transitional chaotic (very close to chaotic ferroresonance in pattern and frequency spectrum) ferroresonance modes. Another model presented in Figure 2.19 is used for generating quasi-periodic ferroresonance signals. This case is simpler compared to the 400 kV line switching in Figure 2.18.

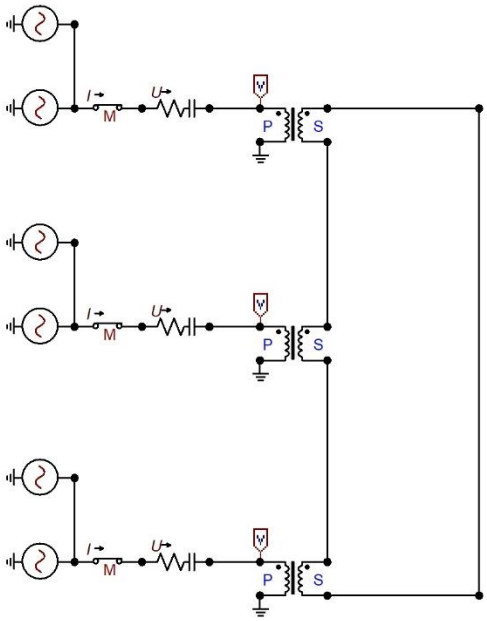

Figure 2.19 EMTP Model 2: Quasi-periodic ferroresonance

The voltage and the current waveforms of the different ferroresonance modes obtained by changing the circuit parameters in Table 2-1 are shown below. Fundamental ferroresonance voltage (V) and current (I) are shown in Figure 2.20 and Figure 2.21 respectively.

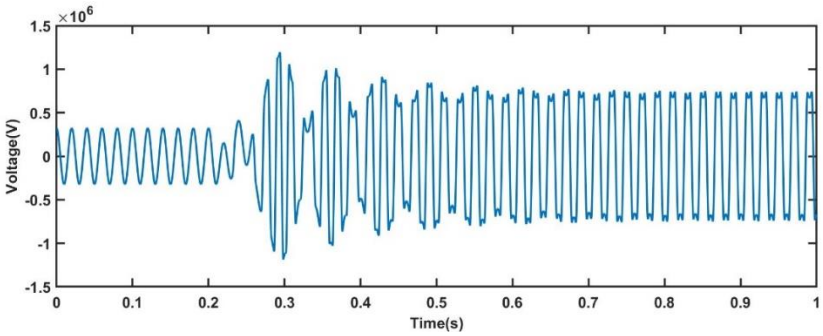

Figure 2.20 Fundamental ferroresonance voltage waveform

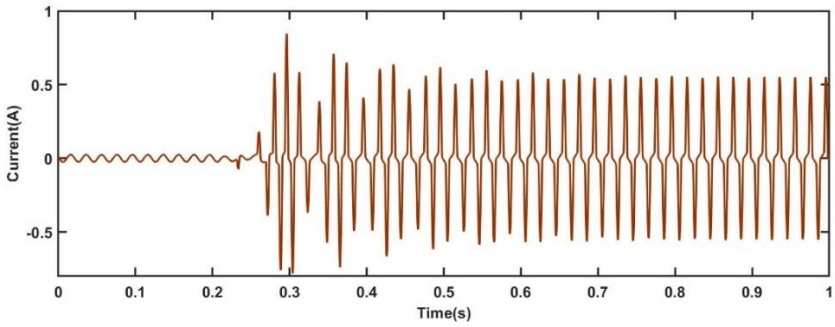

Figure 2.21 Fundamental ferroresonance current waveform

Subharmonic mode V,I waveforms are depicted in Figure 2.22 and Figure 2.23 while the quasi-periodic V and I generated from Figure 2.19 are shown in Figure 2.24 and Figure 2.25 respectively.

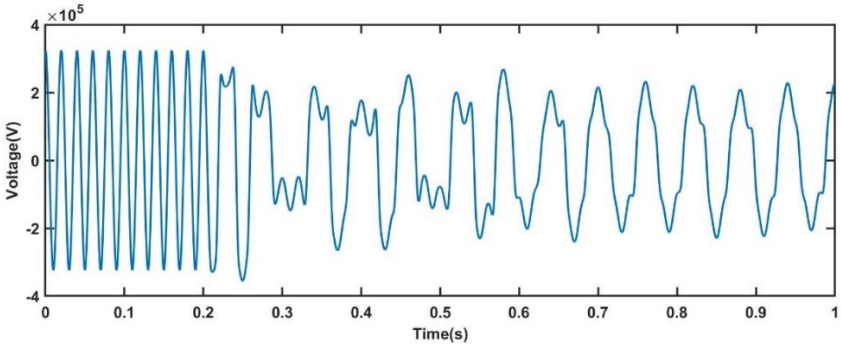

Figure 2.22 Subharmonic ferroresonance voltage waveform

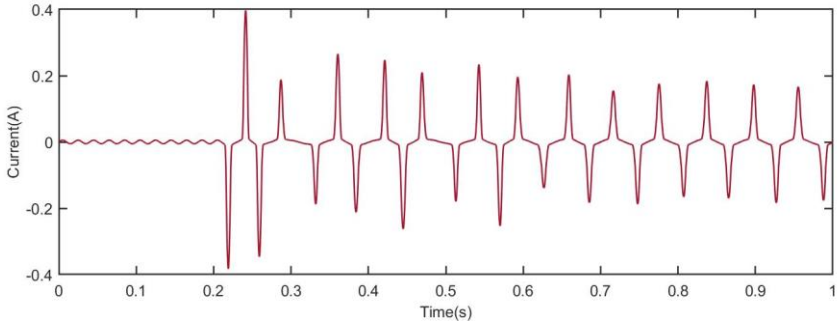

Figure 2.23 Subharmonic ferroresonance current waveform

The waveform in Figure 2.26 is termed chaotic because the signal has no specific pattern and the sustained period amplitude is not uniform compared to the other cases. For instance, quasi-periodic mode, which is also not periodic, shares the property of both subharmonic and fundamental

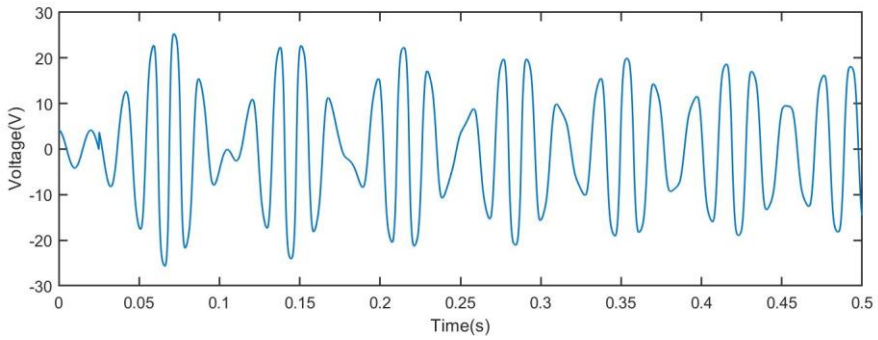

Figure 2.24 Quasi-periodic ferroresonance voltage waveform

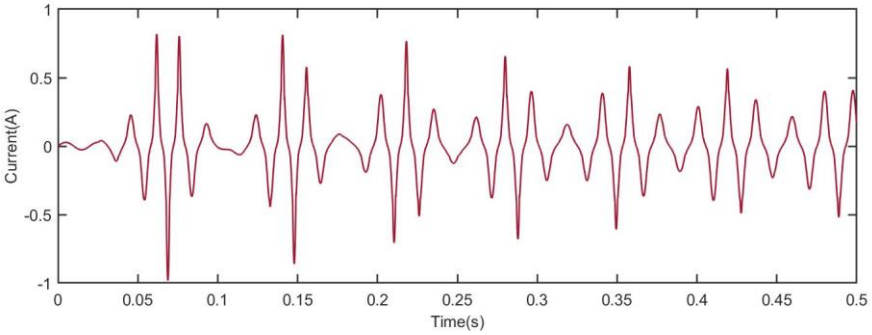

Figure 2.25 Quasi-periodic ferroresonance current waveform

ferroresonance. However, the translational chaotic signal has a broad frequency spectrum and even though the current seems periodic, the period per each cycle differs.

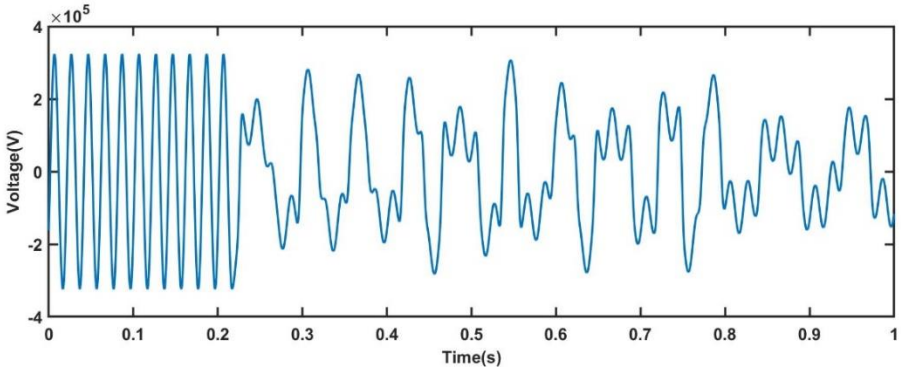

Figure 2.26 Chaotic ferroresonance voltage waveform

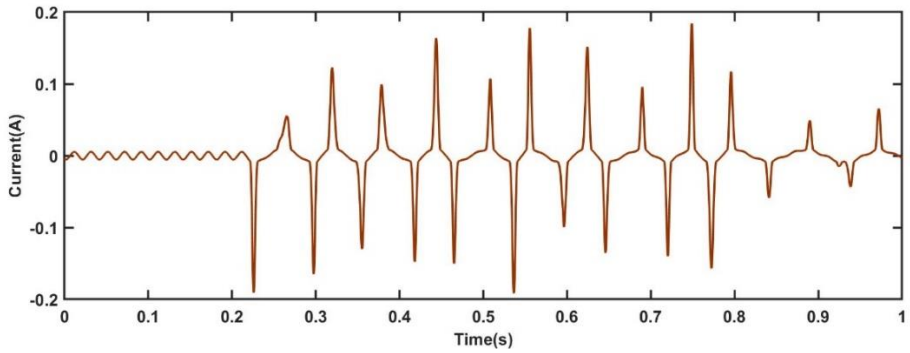

Figure 2.27 Chaotic ferroresonance current waveform

2.5.1 Impact of capacitance

The lower the value of the capacitance, the lesser the likelihood of ferroresonance occurrence. Figure 2.28 shows the graphical solution of the effect of increase and decrease of capacitance values on the onset of ferroresonance. The value of the capacitance is equivalent to the size and the thickness of the dashed blue lines, the higher the capacitance, the higher the gap between the dashes.

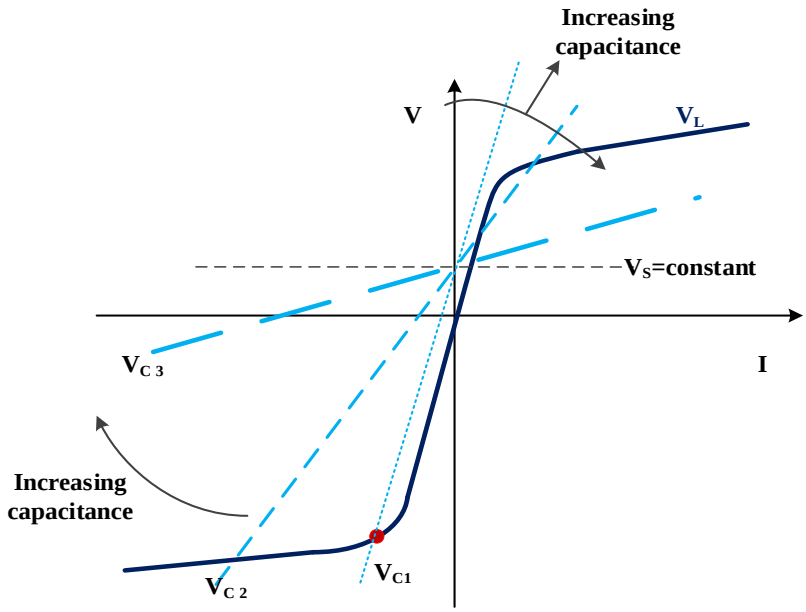

Figure 2.28 Impact of reducing & increasing capacitance

It can be observed from the plot that a very high and a very low capacitance values will not result in ferroresonance. The critical value of capacitance for ferroresonance occurrence is the value of C for the line V_{C1} in Figure 2.28 . This is a ferroresonant state, at this point, the initial normal operating state and unstable state in Figure 2.4 disappear. A slight increase or decrease around this value result in ferroresonance. If the capacitance is high enough like in V_{C3} case, the ferroresonant and unstable state disappear, and the circuit operates in a normal state. The grading capacitance of the breaker is also changed in the EMTP model to observes the impact on ferroresonance. The voltage waveform for different grading capacitors from the default value of 600 pF to 120 pF, 300 pF and 1200 pF are shown in Figure 2.29. The value of the grading capacitor affects the magnitude of the sustained ferroresonance; higher capacitance gives higher voltage magnitude as seen in Figure 2.29. Reducing the capacitance value in the network mitigates ferroresonance inception. The results from the EMTP model also corroborate the scenarios depicted in Figure 2.28. The capacitance voltage line intersects the

magnetizing curve V_L in the linear region when the capacitance value is low. The sustained mode of ferroresonance is avoided when the grading capacitance is reduced to 180 pF and 60 pF from 600 pF. Other circuit parameters: the source voltage, the shunt capacitance and the switching time are kept constant including the magnetizing loss of the transformer. As can be observed from Figure 2.29, at very high capacitance value of 1200 pF, the ferroresonant waveform shows more quasi-periodic oscillation compared to other cases. Similar results are observed for 1300 pF and 1400 pF.

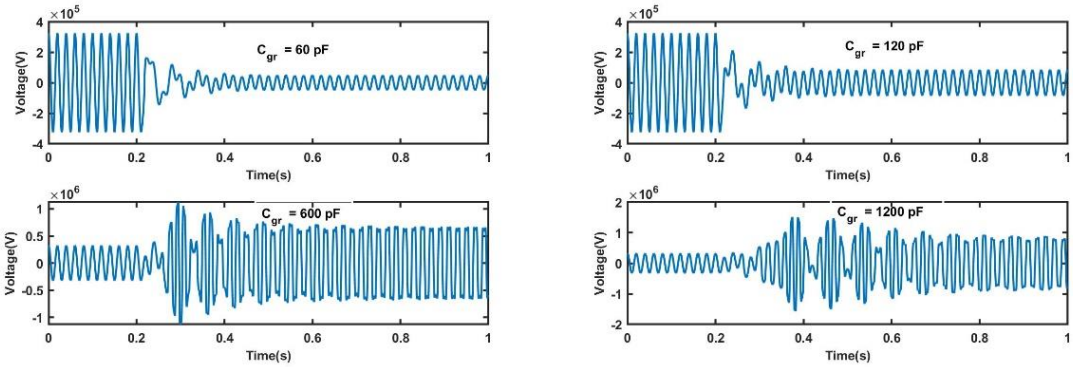

Figure 2.29 Ferroresonant voltage for different capacitance values

2.5.2 Impact of resistance

The introduction of more damping to the system can increase the losses and prevent the occurrence of ferroresonance. As discussed above, one of the conditions needed for ferroresonance occurrence is low losses. The case study of 400 kV line switch that resulted in ferroresonance also behaved differently when a 0.5 Ω resistor was connected to open delta of the transformer based on the VT's manufacturer recommendation. More information about this can be found in [18]. Ferroresonant state is sustained when the circuit loss is exceeded by the supply from the external source (if present), otherwise the oscillation will be damped down to a steady-state operation or the onset of ferroresonance prevented. Figure 2.30 explained this concept when damping is introduced into the ferroresonant circuit in Figure 2.2. The solution to the circuit with R is:

$$V_s = \mathrm{R} \cdot I + jX_L(I) \cdot \mathrm{I} - \mathrm{j}\, X_C \cdot I \tag{2.4}$$

$$V_s^2 = (\mathrm{R}I)^2 \ + (IX_L(I) - \mathrm{IX_C})^2 = (\mathrm{R}I)^2 + (\mathrm{U_L(I)} - \mathrm{IX_C})^2 \tag{2.5}$$

$$V_s^2 - (\mathrm{R}I)^2 = (\mathrm{U_L(I)} - \mathrm{IX_C})^2 \tag{2.6}$$

$$\sqrt{V_s^2 - (\mathrm{R}I)^2} = |\mathrm{U_L(I)} - \mathrm{IX_C}|^2 \tag{2.7}$$

The solution to equation (2.7) is plotted in Figure 2.30 with two values of circuit losses, R_1 and R_2 in which $R_1 > R_2$. Analogous to the previous cases, point 1 is the normal linear state, point 2 is the unstable state while point 3 is the ferroresonant state. It can be observed from the graph that a higher value of R prevented the circuit from going into ferroresonant state.

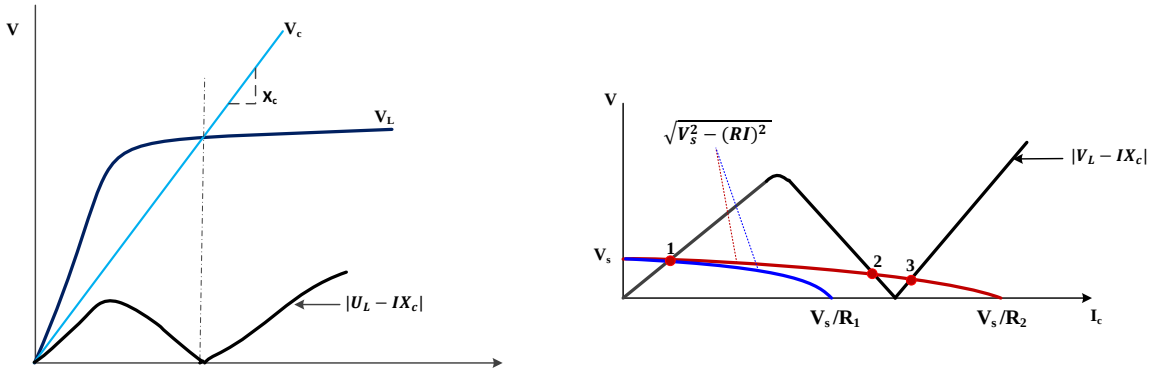

Figure 2.30 Impact of damping on ferroresonance occurrence

The quantitative solution above over simplified the complex ferroresonant phenomenon and it is not valid for operation in the saturated region of the inductance (ferroresonant state) due to high harmonic contents. The analysis considers only the power frequency and the steady-state operation; however, it gives a good indication of the phenomenon [3].

2.5.3 Impact of voltage source

Increasing the magnitude of the source voltage increases the duration and the peak of the transient period. Figure 2.31 depicts the effect of the source voltage on ferroresonance occurrence. The thin dash line through the origin in Figure 2.31 represents the case with no external source. The V_s line intersect the inductance voltage curve at the point prone to ferroresonance marked with red dots. It can be inferred that ferroresonance can occur even in the absence of an external energy source. Increasing the source voltages moves the line $V_s + V_c$ away from the normal and unstable state, and the only possible solution is the ferroresonant state marked point 3. This indicates that ferroresonant state is self-sustained and higher voltage magnitude increases the vulnerability because the intersection is on the saturated region of the curve. The value of the source voltage in the EMTP model in Figure 2.18 is varied from 324 kV up to 140 % increase with 10 % increase in each step. The voltage waveform changes with the voltage rating, starting with a quasi-periodic mode before settling finally to a fundamental mode. Only the case in which $V_s = 340.2$ kV that does not result in ferroresonance in this voltage range.

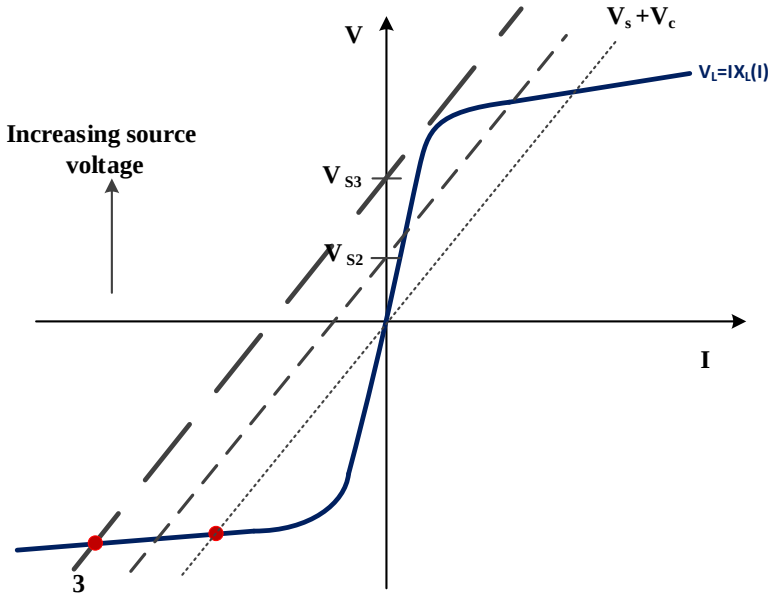

Figure 2.31 Impact of increasing source voltage

2.6 Mitigation of ferroresonance

The likelihood of ferroresonance occurrence can be prevented by avoiding switching techniques that could aid formation of a ferroresonant circuit: a series combination of capacitance with a non-linear inductance with low losses and/or low loading.
Reducing the length of the de-energized transmission line connected to the transformer can helps in mitigating the risk of ferroresonance. The critical length of MV cable $L_{critical}$ in meter is discussed in [3].
Another important mitigating solution is to increase the damping by introducing more losses (load resistance) to the susceptible transformer. Even-though, this pose a huge energy loss due to I^2R during normal operating state, it ensures that there is no sufficient energy from the external source to sustain the circuit in ferroresonant mode. Other mitigating factors are explained in [3].

2.7 Conclusion

This chapter summarizes the main characteristics of ferroresonance, the possible causes and the network topologies that are susceptible to ferroresonance. The mitigating factors to reduce the risk of this disturbance are also discussed. The best line of defense against ferroresonance is to understand the phenomenon and do a proper predictive study during the design phase to avoid its occurrence. However, this is not always the case, and this necessitate the detection and elimination of this severe disturbance. Ferromagnetic materials are needed for this non-linear disturbance to happen. In addition to the non-linear inductance of saturable magnetic core, capacitance, external energy source and low losses are needed for the inception and sustaining the oscillation. It can be concluded that ferroresonance can occur at any voltage level provided the circuit elements needed for its initiation are present. However, increasing the voltage increases the risk of ferroresonance while increasing the circuit losses reduces the risk. The different modes of ferroresonance, which are dependent on initial circuit parameters prior to ferroresonance inception, are discussed and the classification is based on periodicity and frequency spectrum of the waveform. The four common modes of ferroresonance are investigated are: fundamental, subharmonic, quasi-periodic and chaotic modes. The mode a ferroresonant oscillation settles to is influenced by system parameters and initial conditions.

3 Arcing - Modeling and Simulation

An electric arc is a continuous discharge, a non-linear electrical phenomenon that occurs regularly in power systems. When a switching action occurs in a power system, the current is not interrupted immediately but flows through an arc until a current zero is reached. When the current is suppressed before a current zero, it can cause abnormal overvoltage due to the exchange of energy between the capacitive elements and inductive elements in the network. Although an electric arc is necessary in the operation of switching devices, but an undesired electric arc can have a detrimental effect on power system transmission and distribution networks and on electronic loads. The temperature associated with an electric arc is very high; it can melt the insulation and cause undue stress to the electrical equipment. This chapter discusses the literature review of different arc models and the results obtained from the implementation of some of these models. In order to develop a good detection scheme for arcing faults, it is paramount to have a good understanding of an electric arc behavior. One of the cost-effective ways of achieving this is by simulating different arc behaviors in an electrical network and studying the patterns. In electrical power systems, faults on the transmission lines have reverberating effects on the distribution network and connected nodes. Although the transmission network has n-1 contingency in most cases, it is important to improve the fault detection and clearing time in order to improve the reliability of the network. Majority of the faults that occur on the transmission lines are single phase to ground arcing faults [4], therefore, a single phase to ground fault is investigated in this chapter. Fast detection and classification of this fault can help in minimizing downtime and improve the security of supply.

There are other reasons why understanding and studying an arc behavior is important in power systems, for instance, in a low voltage network, a lot of cases of electric fire has been reported to be caused by electric arc. In addition, nearly 80 % to 90 % of the fault on transmission lines are single phase to ground faults that involve arcing. Majority of these faults are transient in nature and need coordination of an auto-recloser to reconnect the network after fault elimination for continuous operation. Closing of an auto-recloser on a fault could cause a high overvoltage and overcurrent that can be detrimental to the operation of the network. An uncontrolled electric arc is destructive because the arc continuously draws current from a fixed voltage supply [20]. Different black box arc models are investigated as well as an elongated arc in the air, primary and secondary arc behaviors. High impedance arc fault is also explained in this chapter. For the detection of a secondary arc extinction time, a detailed model in ATPDraw and its analysis is presented in this chapter. The behavior of an electric arc is affected by environmental conditions, however, only the thermal property of the arc is modelled. The environmental and dielectric conditions are not considered. The thermal model gives a good approximation to the behavior of an electric arc and it is suited for investigation of the phenomenon.

3.1 Contribution of Arc Detection to Power System Protection

When a fault occurs in a power system, it could be transient or permanent and both are usually associated with an arc. Understanding the arc behavior and proper detection can thus help in detecting these kinds of faults. For instance, a high impedance fault could go undetected due to a low current which makes it difficult for classical protection devices to operate. These types of faults could also create a low resistance to ground and cause a high current earthing fault [21]. Most system operators use a single-phase auto-recloser (SPAR) to detect and isolate temporary faults on the network to prevent downtime and improve reliability of the network. The switching device clears the fault by opening the faulty phase(s). An auto-recloser works by opening when a fault is detected in the network and the opening time usually marks the beginning of the secondary arc. After a certain preset time (or adaptive in some

cases), the auto-recloser re-energizes the line(s) by re-closing. Understanding and detecting the secondary arc fault signatures can help in improving the operation of SPAR and preventing it from closing on secondary arc. The secondary arc harmonic signatures was used in [22] for the implementation of an adaptive auto-recloser.

The influence of an electric arc on the operation of distance protection relays cannot be overemphasized. The distance protection relays make use of resistance calculation to localize faults and trip the circuit. The value of an arc resistance when a fault occurs can impair the accuracy of operation of the relay. Warrington formulated an empirical formula for calculating the non-linear arc resistance using the root mean square (RMS) current of the fault as shown in equation (3.1). An improved model was developed in [23] and a new formula was formulated (equation (3.2)) in order to improve the accuracy of the calculated arc resistance.

$$\mathrm{R_A} = \frac{28710}{I^{1.4}} \cdot L \tag{3.1}$$

where R_A is the arc resistance in Ω, I is the RMS arc current in A and L is the length of the arc in m.

$$\mathrm{R_A} = \frac{2\sqrt{2}}{\pi} \frac{E_A \cdot L}{I} \tag{3.2}$$

where E_A is the arc voltage gradient in V/cm, L is the length of the arc in cm.

An electric arc model is also important to analyze the interruption capability of circuit breakers. However, the physical arc model that involves fluid dynamic is used for designing circuit breakers while the thermal model is sufficient for analyzing arc faults as reported in [1, 22, 24]. This is because different circuit breakers use different medium in quenching electric arcs formed between their contacts

3.2 Primary and Secondary Arc

An arc fault is a common phenomenon in a single phase or other types of faults especially occurring on transmission lines [4]. Switching arc of a disconnector or a breaker usually accompanies the faults in the network. This type of arc fault is usually associated with a high fault current and the period from the arc fault inception till the instant when the circuit breaker isolates the faulty phase is referred to as primary arc. The time constant of the arc and the arc length are assumed to be constant during the primary arc. In some cases, the arc is elongated for a longer period in the air as discussed in [25]. The elongation of the arc in the air could be caused by the circuit parameters but mostly influenced by the atmospheric conditions. The primary arc is followed by a secondary arc that is initiated after isolation of the fault on the transmission lines. A secondary arc is formed by the coupling between the healthy phase(s) and the faulty phase due to the mutual capacitance and inductance between the phases. It is sustained by the energy trapped in the inductive and capacitive elements in the network that is released after the fault isolation. The primary arc generally shows a deterministic behavior unlike the secondary arc that behaves randomly. The randomness is influenced by the external factors around the arc channel like the wind speed, the surrounding air, the thermal buoyancy and the electrodynamics forces [26, 27, 28].

The coupling causes a low current to flow and a higher voltage magnitude compared to the primary arc phenomenon. In contrast to the primary arc, the secondary arc length is not constant, and it depends on the external conditions and also on some of the arc parameters. There are many arc models in literature that characterize the relationship between the arc length and the secondary arc parameters. Understanding the secondary arc behavior is necessary to coordinate auto-recloser from operating on permanent faults. This could lead to oscillation and could affect the system stability [27]. If a robust arc detection scheme is implemented, the delay time before closing SPAR can be dynamic and adaptive. This further necessitates the detection of an arcing fault. An electric arc is also a source of harmonics

injection into the network, and as there are many electronic devices that are sensitive to harmonics in the network, a more robust way to detect is important.

3.3 Low Current Arc

A high impedance arc and a series arc are types of electric arcing faults characterized by low current. The series arc is initiated when a fault path exists between the load and the source. It could be caused by an accumulated dust particle and loose connections in the network. Due to the network configuration during the arc occurrence as shown in Figure 3.1, a series arc only occurs on a single phase. This arc has been extensively studied in low voltage system and the different detection schemes are discussed in [29, 30, 31]. The arc waveforms especially the current waveform is dependent on the type of connected loads.

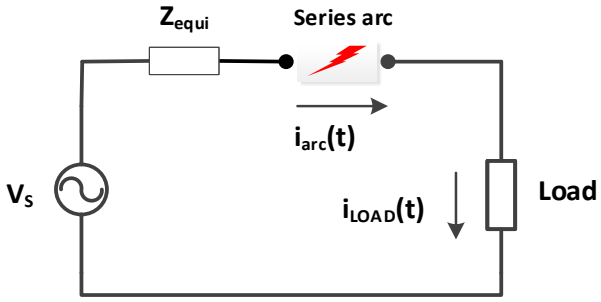

Figure 3.1 Series Arc topology

Low current electrical arcs are also detrimental to the switch gears and other equipment in power systems when they are not detected on time before they developed into short circuits. They have a low current magnitude, similar to the load current. This causes difficulties for conventional protection devices to detect them and to clear the fault respectively.
A high impedance arcing fault is also another low current arc usually investigated in the distribution and the transmission networks. The fault is caused when a tree branch or animals or other high resistance objects make contact between the phase conductor and the ground on the transmission lines. Many detection strategies are discussed in [21, 32]. The non-linearity of the arc resistance and low current causes difficulties to easily locate and detect these arcing faults. A high impedance fault (HIF) could be caused by a fallen conductor touching the ground or indirect connection to ground through trees or other objects. Although HIFs do not cause severe damage to the network immediately, live conductor poses a risk to people and properties in contact. Trees are the major cause of this fault especially for long transmission lines in forests. A staged test with tree branches, leaves and sand are conducted in [33] for the detection of HIF. The experimental results were compared to ATP simulations. It was observed that the tree leaves could cause a fire due to simultaneous arcing points. The moisture content of the objects also affects the magnitude of the measured current; moisture content increases the magnitude of the current compared to dry objects like dry sand.
A common observation in low current arcing faults is the shoulder (a short interval during current build up phase [33]) and the dependence of the observed waveform on the objects in case of HIF and on the connected load in case of a series arc. The distortions are source of harmonics into the network and a continuous injection could affect the operation of electronic loads in the network.

3.4 Black box arc model

Arc models used for simulating different arc scenarios explained above are divided into three categories: black-box models, physical models and parametric models [34]. The black box model is a simple

mathematical equation that describes the relationship between the arc conductance and the network parameters. Three black box models are analyzed and discussed in this section.
The classical arc models are based on the theory of energy conservation, considering the arc as an energy burning phenomenon exchanging heat with the environment. According to the power balance principle, the power inflow must be the same as the power outflow. Thus, the arc equation can be formulated as:

$$\frac{dQ}{dt} = \mathrm{P_{in}} - P_{out} \tag{3.3}$$

where Q is the energy stored in the arc channel measured in J, $\mathrm{P_{in}}$ is the thermal energy inflow and P_{out} is the thermal energy outflow. The thermal energy of an electric arc due to the thermal dissipation is given by:

$$p_{in} = u \cdot i = u \cdot \frac{u}{R} = u \cdot u \cdot g = gu^2 \tag{3.4}$$

The basic classical arc model equation is:

$$\frac{1}{g}\frac{dg}{dt} = \frac{1}{\tau}\left(\frac{gu^2}{P_{out}(g)} - 1\right) \tag{3.5}$$

where g is dynamic arc conductance, τ is the time constant and u is the voltage. The thermal energy outflow P_{out} is model dependent and it is determined for different arc models discussed below.

Cassie and Mayr arc models are widely implemented black box arc models for the simulation of low and high current arc in circuit breakers and overhead line faults [4]. The arc model is based on the principle of energy balance coupled with some simplifying assumptions about the arc occurrence. Cassie arc model is suited for studying the arc conductance behavior during a high current interval while Mayr model is suited for the arc behavior around a current zero [25, 27, 28]. In some cases, these two arc models are combined for better results as done in [24]. Consequently, the equivalent arc resistance is series connected and calculated as in equation (3.6):

$$\frac{1}{g} = \frac{1}{g_m} + \frac{1}{g_c} \tag{3.6}$$

where g_m and g_c are arc conductance from Mayr and Cassie arc equation respectively.

Mayr assumed that the arc energy loss is a heat transport thermal flow. The power loss or cooling power of the arc is equally assumed to be constant. The temperature of the arc column varies exponentially, as the conductance of the arc depends on the temperature of the arc. Furthermore, the cross-section of the arc column is assumed to be constant. The arc conductance is uniform within the arc column and also depends on the stored energy Q. The relationship between g and Q is:

$$g = k\, e^{Q/Q_o} \tag{3.7}$$

k and Q_o are constant parameters. Substituting equation (3.7) in the general arc equation, the formula shown below is obtained.

$$\frac{dQ}{dt} = Q_o \frac{1}{g}\frac{dg}{dt} \tag{3.8}$$

$$\frac{1}{g}\frac{dg}{dt} = \frac{1}{Q_o}\,(gu^2 - p_o) = \frac{p_o}{Q_o}\left(\frac{gu^2}{p_o} - 1\right) \tag{3.9}$$

$$\frac{1}{g}\frac{dg}{dt} = \frac{1}{\tau}\left(\frac{ui}{p_o} - 1\right) \tag{3.10}$$

where $\tau\left(\frac{Q_o}{p_o}\right)$ is the time constant and p_o is the constant arc cooling power.
Cassie on the other hand assumed that the current is relatively a high current, and the cooling power is due to convection. The arc voltage and the temperature are assumed to be constant, but a varying arc

column cross-sectional area is assumed. The arc resistance is adjusted in the variable arc column to obtain the arc current. The cooling power in this case is:

$$p_o = g\, u_o^2 \tag{3.11}$$

where u_o is the reference voltage drop. The general Cassie equation is thus formulated as:

$$\frac{1}{g}\frac{dg}{dt} = \frac{1}{\tau}\left(\frac{u^2}{u_o^2} - 1\right) \tag{3.12}$$

Another popular black box arc model is the Hochrainer equation formulated as:

$$\frac{dg}{dt} = \frac{1}{\tau}(G - g) \tag{3.13}$$

This arc model is derived using the control theory.

One of the main challenges with the black box arc model is selecting the values of the parameters. According to the authors in [23], the general dynamic arc equation is formulated as:

$$\frac{dg}{dt} = f(g, i, u, \pi) \tag{3.14}$$

where g is the time varying arc resistance and π is the set of unknown model parameters that must be selected from test data. The model parameters used in the simulation discussed in the subsequent section are obtained from the empirical data published in [35]. The authors in [26, 35] used the Hochrainer model to investigate secondary arc.

3.5 Arc Models

In order to detect an arcing fault and classify it, this thesis focuses on two major arc phenomena. The first one is the elongated arc in the air. Although the length of the arc is assumed to be constant during the high fault current primary arc, the length could be affected in some cases as discussed in [25]. The detection of this arc fault is included in the final classification algorithm proposed in this thesis. The other arc model considered is the primary and secondary arc model initiated by a single phase to ground fault on a 230 kV transmission line.

3.5.1 Long Arc in the air model

A modified version of the elongated arc in the air in [25] is implemented for the detection of long arc in the air. Figure 3.2 shows the ATPDraw model and the validated arc parameters presented in [25] are used.

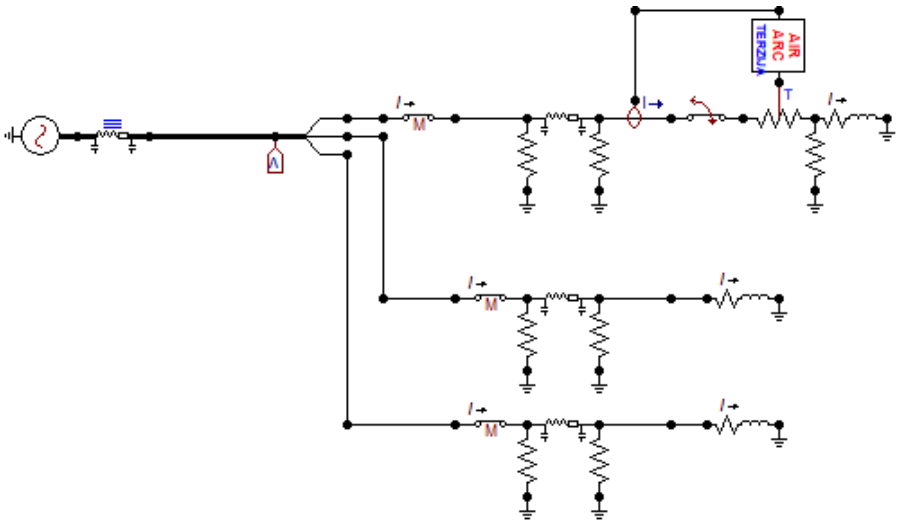

Figure 3.2 EMTP Model - Elongated Arc Fault in the Air

The electric parameters of the arc are simulated in EMTP and a type 91 TACS (Transient Analysis of Control Systems) resistor is used to model the dynamic behavior of the arc resistance. A three-phase model is used in analyzing the arc behavior when a single phase to ground fault occurs on phase A. In order to validate the arc model in [25], the authors compared the current and the voltage waveforms obtained from the simulation to experimental results. A correlation of 0.93344 was obtained from the comparison. This proves that the arc model is close to real arc phenomenon, thus the waveforms from the model give adequate properties that can be used for arc fault detection.

Figure 3.3 shows the arc voltage (left) and the arc current (right) obtained from the modified arc model in Figure 3.2. The arc voltage is very distorted and close to a rectangular waveform. However, the arc current is not affected except the slight displacement (DC component) at fault inception. The arc voltage has a high harmonic contents and part of it propagated to the line voltage and caused some distortion as shown in the waveform on the left in Figure 3.4. The closer the observation point is to the source of harmonic injection, the higher the distortion level observed. The fault location, the fault current magnitude and the network topology determine the impact of the distortion on the signals. At the fault inception, the length of the arc is determined by the static length of the breaker, the switching device or the distance between the arc columns. As can be seen in Figure 3.5, the arc length affects the magnitude of the arc voltage. The arc voltage increases as the arc length increases and the relationship between them is determined by the arc voltage gradient E_A measured in V/cm. The impact of the arc elongation is not obvious in the current as seen in Figure 3.3. The arc model is quasi-dynamic and more information about the model derivation can be found in [4, 25]. The arc voltage is formulated as shown in equation (3.16).

$$v_{a0}(t) = (U_a + U_b \frac{I_o}{i_b(t)} + R_\delta |i_b(t)|)\, sgn(i_a) + \zeta \tag{3.15}$$

$$v_a(t) = v_{a0}(t)\left[1 + Ae^{B(t-T_i)}\, h(t-T_i)\right] \tag{3.16}$$

$$i_b(t) = \begin{cases} \mathrm{I_o}, & |i_a(t)| < 0 \\ |i_a(t)|, & |i_a(t)| \geq 0 \end{cases} \tag{3.17}$$

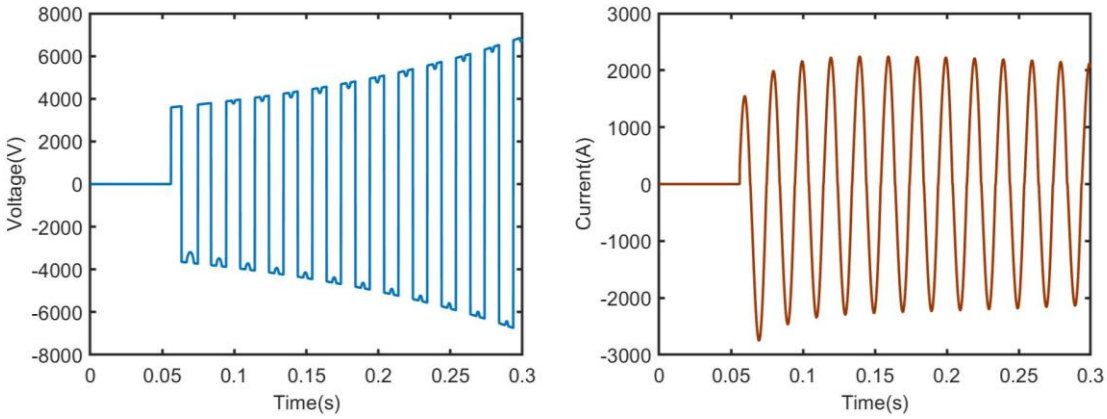

Figure 3.3 Arc voltage and arc current (left to right)

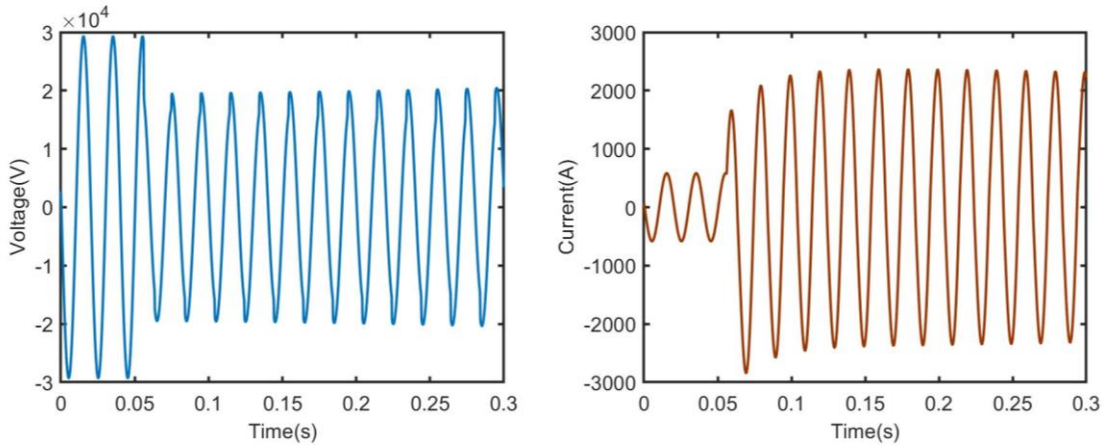

Figure 3.4 Line voltage and current: Elongated air arc

The arc resistance increases as the length increases and this implies that the time varying conductance of the arc, g, should decreases with time. Figure 3.5 shows the time varying arc conductance over time. An electric arc is with a resistive nature, the arc voltage and the arc current are in phase as shown in Figure 3.5.

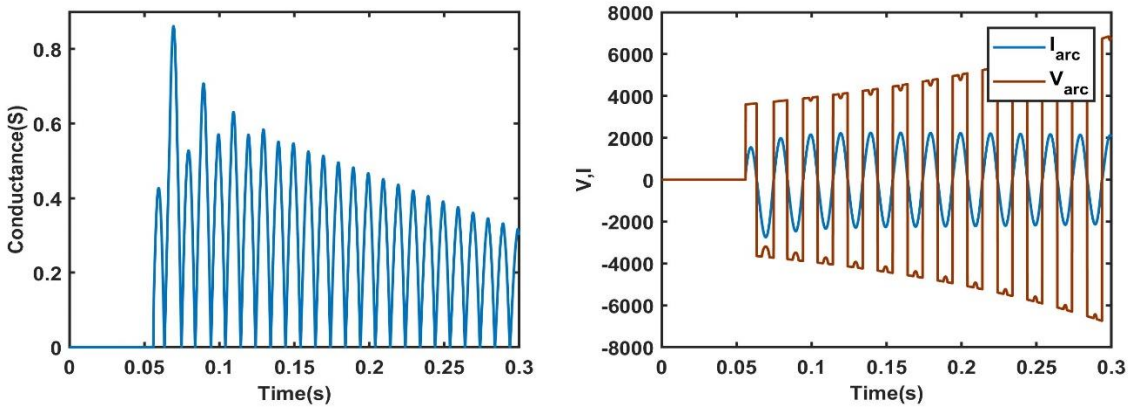

Figure 3.5 Elongate air arc conductance, voltage and current waveform

As stated in [27] and confirmed by the simulations, the value of the THD (Total Harmonic Distortion) measured in the system voltage is influenced by the interaction between the network impedance and the electric arc phenomenon during the fault. The pollutant is the square wave of the arc voltage with dominant odd harmonics. According to [25], the total harmonic distortion (THD) of the simulated line voltage was approximately 5 % when the 3rd to the 11th harmonic orders were considered. A THD between the ranges of 3.05 % to 5.23 % of the line voltage is obtained in this project. However, the THD value up to 3.62 % is observed for the arc current compared to 2.05 % in [25]. The arc parameters and the circuit parameters are changed to generate different scenarios, these values are used for detection and classification later. The ratings of the connected loads and the fault resistance are also changed. The higher the fault resistance, the lower the fault current and the arc current.

3.5.2 Modeling of primary and secondary arc

The arc model used for the primary and the secondary arc investigation is based on the theory of energy balance in the arc column, the Hochrainer arc model is implemented. This describes the arc in the open air by a differential equation that determines the instantaneous arc conductance. Kizilcay and Pniok work from 1991 described the two periods of arcing. The secondary arc has some elongation properties with the arc reaching 10 times its original length due to the magnetic forces and the environmental conditions [36]. The mathematical model of the arc is described by equation (3.18).

$$\frac{dg}{dt} = \frac{1}{\tau}(G - g) \tag{3.18}$$

where τ is the time constant of the arc, g and G are the instantaneous and the static arc conductance respectively. Because the arc is assumed to be burning freely in the air, there is a slight deviation from the black box model, the arc voltage is assumed not to be constant [36]. It is assumed to be dependent on the arc length and the instantaneous short circuit current flowing through the arc, the arc current. It is defined as:

$$u_{st} = (u_o + r_o|i_{arc}|)l_{arc} \tag{3.19}$$

The stationary arc conductance G is dependent on the arc current and the voltage. With the assumption that arc is resistive in nature, it is defined as:

$$G = \frac{|i_{arc}|}{u_{st}} \tag{3.20}$$

where u_{st} is the stationary arc voltage; u_o is the characteristic arc voltage per unit length; r_o is the characteristic arc resistance per unit length; i_{arc} is the instantaneous arc current; l_{arc} is the time dependent arc length.

$$G = \frac{|i_{arc}|}{(u_o + r_o|i_{arc}|)l_{arc}} \tag{3.21}$$

The time constant of the arc, τ is dependent on the arc length and their relationship is formulated as:

$$\tau = \tau_o \left(\frac{l_{arc}}{l_o}\right)^{\alpha} \tag{3.22}$$

τ_o is the initial time constant; l_o is the initial arc length; l_{arc} is the time dependent arc length; α is a negative constant between -0.1 to -0.6 [4]. This arc model developed by Kizilcay was verified experimentally and it is implemented in this section. The result obtained by varying the circuit parameters are discussed.

The arc phenomenon is a nonlinear dynamic process. It is modelled in ATP-EMTP using the MODELS language and the dynamic arc resistance is represented with a TACS device. The interaction between the electrical network, the physical network and the arc model is shown in Figure 3.6. A type 91 TACS resistor and a type 93 switch are used as the link between the network and the arc model. The simulation is modified based on the previous calculated arc resistance. The input arc current, I_f is used in calculating the value of the constant arc conductance, G, and the differential equation is solved for the value of varying arc conductance g. The inverse of this $\left(\frac{1}{g} = R\right)$ is updated as the new value of the TACS arc resistance and used in the next step-of-time calculation. The arc voltage is obtained by multiplying the arc resistance and the arc current. That way, the interaction between the network and the arc continues until the arc is finally extinguished. In most cases when an electric arc occurs in the network, it generates heat due to the high temperature. Therefore, a good approximation is to model the arc interaction with the physical network by using a resistor.

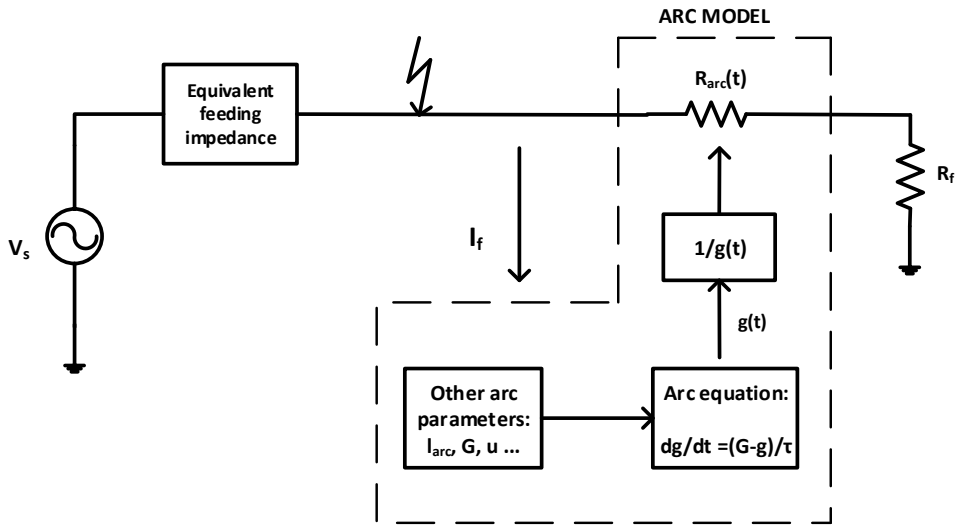

Figure 3.6 Arc interaction with power system network

The conductance of the arc is modeled as a differential equation in ATP as in equation (3.23) and the equivalent Laplace form is given in equation (3.25).

$$g + \tau \frac{dg}{dt} = \frac{i_{arc}}{u_{st}} \tag{3.23}$$

$$g(1 + s\tau) = \frac{i_{arc}}{u_{st}} = G(t) \tag{3.24}$$

$$g(t) = \frac{1}{1 + s\tau} G(t) \tag{3.25}$$

During a primary arc, the arc length and time constant are assumed to be relatively constant. The primary arc is model with equations:

$$\frac{dg}{dt} = \frac{1}{\tau_o}(G - g); \quad G = \frac{i_{arc}}{(u_o + r_o|i_{arc}|)l_o} \tag{3.26}$$

In contrast to the primary arc, the secondary arc has a dynamic behavior with varying arc length and time constant. The arc length and the time constant during the secondary arc are modelled mathematically in ATP as follows:

$$\frac{dg}{dt} = \frac{1}{\tau}(G - g); \quad G = \frac{i_{arc}}{(u_o + r_o|i_{arc}|)l_{arc}} \tag{3.27}$$

$$l_{arc} = (v_l \cdot t + 1) \cdot l_o \tag{3.28}$$

$$\tau = \tau_o - v_\tau(l_{arc} - l_o) \tag{3.29}$$

v_τ is the rate of change of the time constant. The two time constant equations, equation (3.22) and equation (3.29) are implemented and compared. Equation (3.22) is used to calculate the secondary arc time constant in [4] while equation (3.29) was used in [37]. The arc length rises due to environmental conditions and the arc conductance g is almost reduced to zero at arc extinction. This results to a high arc resistance because $r_{arc} = \frac{1}{g}$. The thermal extinction condition for the arc is set by the limits defined in equation (3.30). The secondary arc is extinguished when the rate of change of the arc resistance exceeds the limit, provided that the conductance is less than the specified value of g_{min} in equation (3.30). A minimum condition of 50 µS is used in this model. The dielectric and other external conditions are not taken into consideration in this case.

$$\frac{g_{min}}{l_{arc}} = 0.25 \ \frac{\mu\text{Ʊ}}{cm}; \qquad \frac{\max\left(\frac{dr}{dt}\right)}{l_{arc}} = 64 \ \frac{k\Omega}{s.cm} \tag{3.30}$$

The time constant decreases as the arc length increases according to equation (3.22) and (3.29). The secondary arc duration is affected by the wind speed. The higher the wind speed, the higher the elongation of the arc length and the fast air movement aids the arc extinction. Therefore, the value of time varying arc length $l_{arc}\ (t)$ influences the arc duration and extinction. In order to ensure the stability of the network, to avoid loss of synchronism and prevent arc restrike, the minimum dead time from the time circuit breaker trips [38, 39] is given by:

$$T = 10.5 + \frac{\text{kV}}{34.5} \text{ cycles} \tag{3.31}$$

where *T* is the minimum de-ionization time in cycles and kV is the line-to-line RMS voltage in kV.
The final ATP-EMTP model for primary and secondary arc is shown in Figure 3.7. The arcing results from a single phase to ground fault on phase A, at 50 % length of the transmission line. The frequency dependent model of the transmission lines is used in the model. Figure 3.8 and Figure 3.9 respectively show the voltage and the current waveform using the arc parameters: $\mathrm{u_o} = 12\ \mathrm{V/cm}$, $\mathrm{l_o} = 120\ \mathrm{cm}$, $\mathrm{r_o} = 2.20\ \mathrm{x10^{-3}}\ \Omega/\mathrm{cm}$, $\tau_\mathrm{o} = 0.001\ \mathrm{s}$, $\mathrm{g_{min}} = 5\ \mathrm{x10^{-5}\ S}$, $\mathrm{v_l} = 45\ \mathrm{cm/s}$, $\mathrm{v_\tau} = 2.85\ 10^{-7}\ \mathrm{s/cm}$. A zoomed version of the secondary arc current is presented in the second part of Figure 3.9.
At the beginning when the single phase to ground fault occurs, the breaker marked ***sa*** is closed in order to connect the physical model to the arc model. The line voltage decreases, and the current increases as shown in Figure 3.8 and Figure 3.9 respectively. The high conductance value of the arc during this period implies a low resistance and therefore a high current. Figure 3.10 depicts the arc conductance, the length of the arc and the time constant τ corresponding to the arc parameters given above. The switching from a primary to a secondary arc is coordinated by switches **SW**, **srec** and **sa** in Figure 3.7. Switch **SW** opens at the time $t_{open} = 0.2559\ s$, followed by switch **srec** on the sending end of the line to isolate the fault completely. Then the secondary arc phenomenon, modeled by differential and algebraic equations, is initiated. During this period, switch **SW** is opened while switch **sa** is closed. As can be observed from Figure 3.8, the voltage increases gradually to the recovery voltage. Although the terminal voltage is higher during the secondary arc period, the secondary arc current is low due to the low conductance (Figure 3.10) and the coupling between the phases. When the secondary arc extinction conditions modeled by equation (3.30) is met, then the switch **sa** is opened and this marks the end of the secondary arc. The breaker + Recloser box in Figure 3.7 represents the breaker that isolates the fault to mark the end of primary arc, and the recloser represents the SPAR that reconnects the network after secondary arc is extinguished.

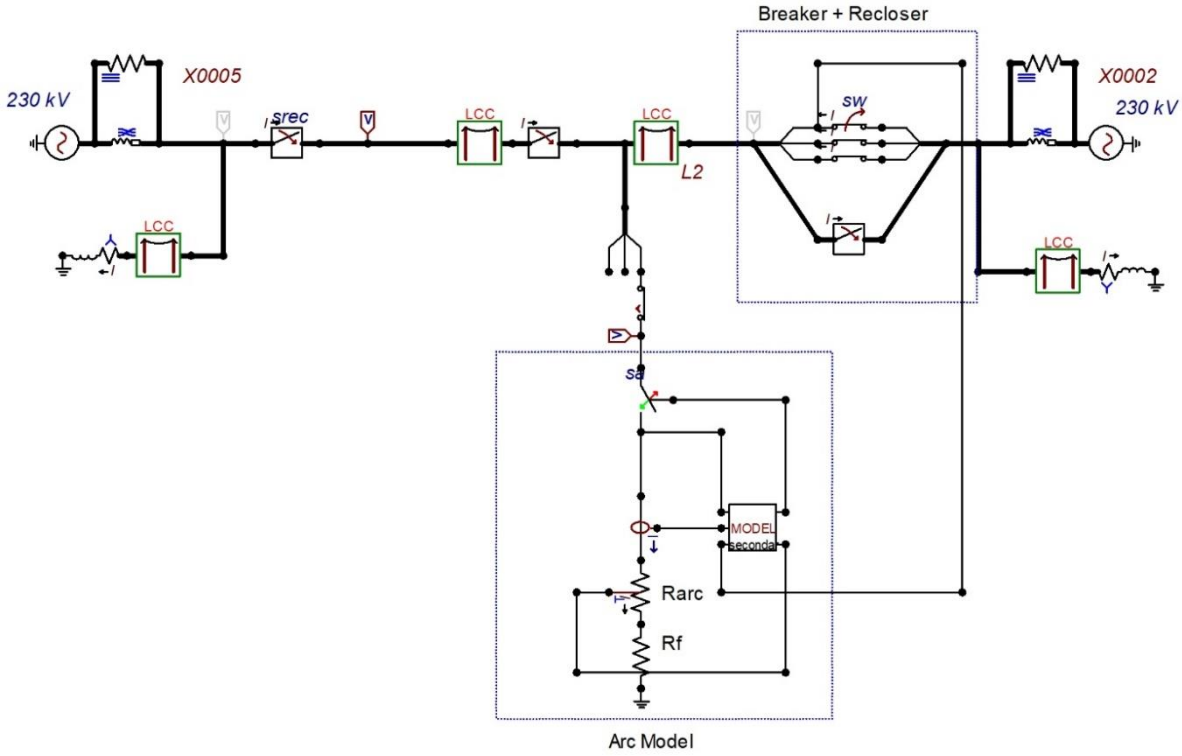

Figure 3.7 EMTP Model: Primary & Secondary Arc

3.5.2.1 Impact of parameter change on the primary and secondary arc

The effect of the circuit elements and the arc model parameters are investigated in this section. The change of the fault resistance R_f influences the magnitude of the primary arc current (fault current) and the voltage, as well as the duration of the secondary arc. As expected, the higher the fault resistance, the lower the fault current. The time of extinction of secondary arc is obvious in the zoomed secondary arc current in Figure 3.9 and the arc length in Figure 3.10. Subsequently, the arc length variation is used to illustrate the effect of the other parameters on the duration of the secondary arc. The decrease of the source voltage V_s or the increase of the static arc voltage per length u_o also reduces the duration of the arc. The impact of the source voltage and voltage gradient u_o are plotted in Figure 3.11. The arc length and the time constant have inverse relationship. When the initial time constant, τ_o decreases, the arc length increases as depicted in Figure 3.10. The current versus voltage curve of the secondary arc shown in Figure 3.12 also indicates the non-linearity of the arc.

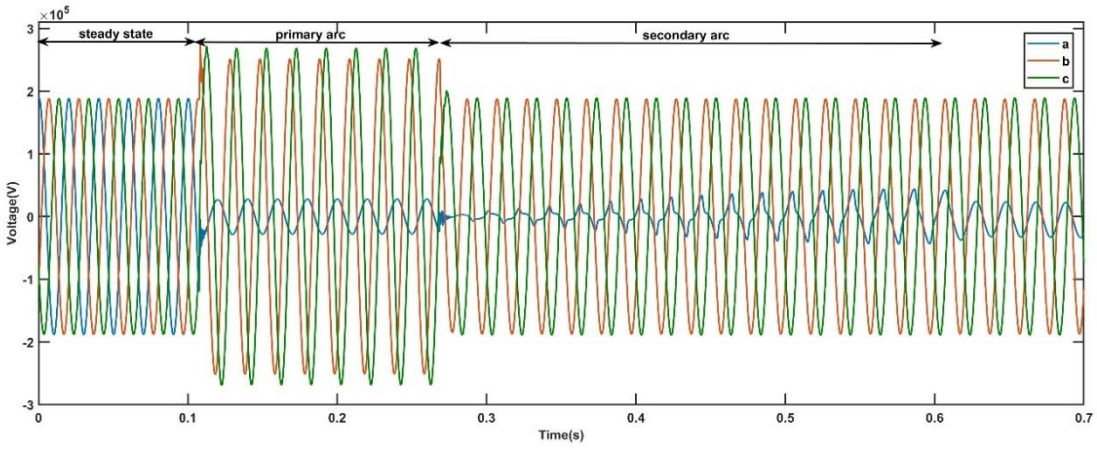

Figure 3.8 Primary and secondary arc voltage

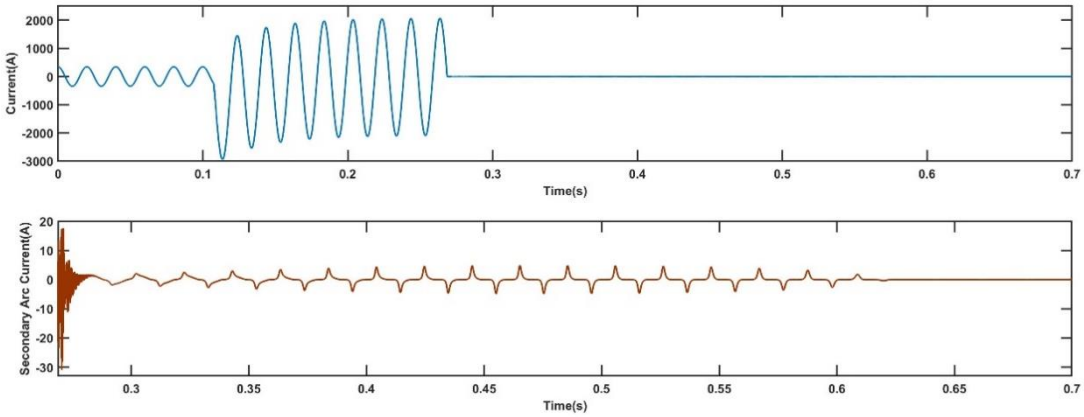

Figure 3.9 primary and secondary arc current

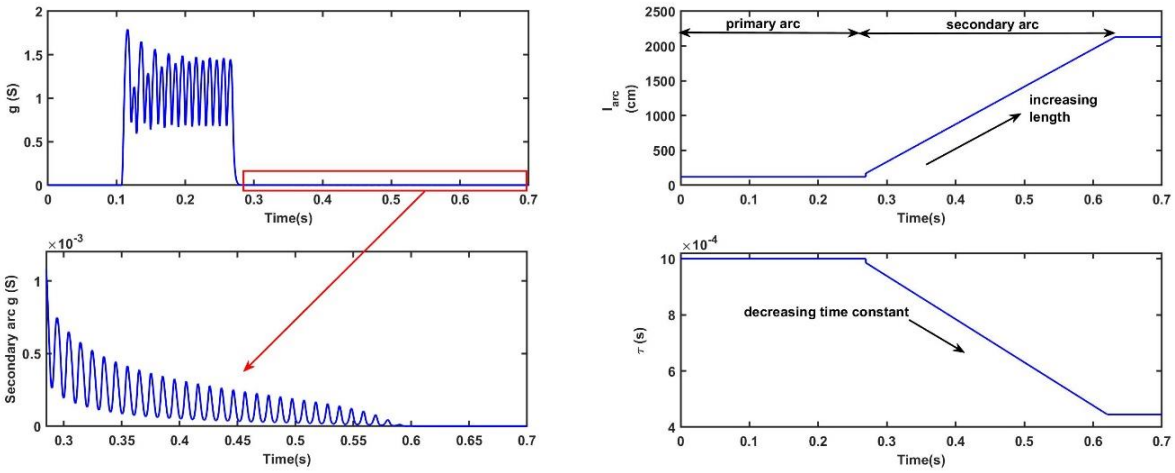

Figure 3.10 Arc conductance, length and time constant

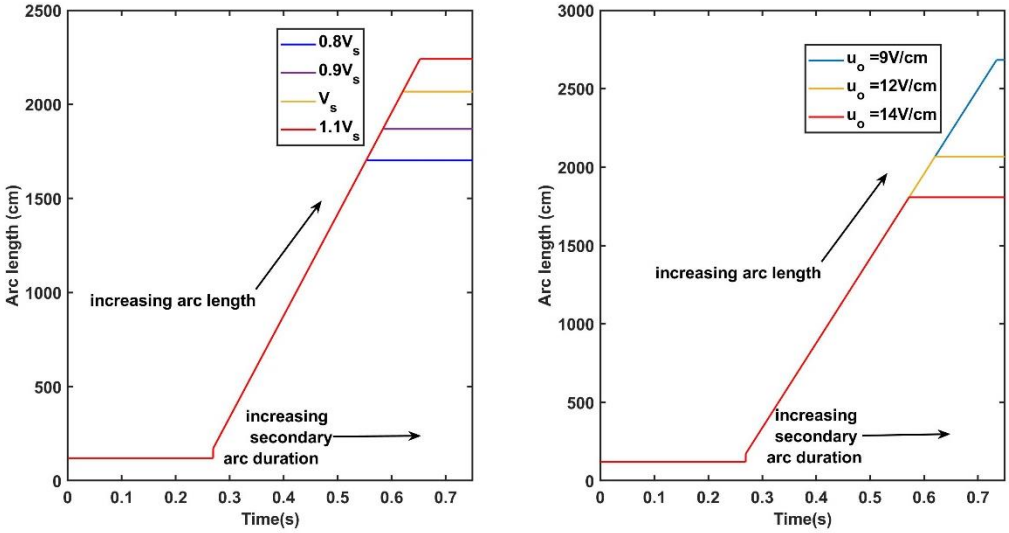

Figure 3.11 Impact of the source voltage and voltage gradient variation on the arc length and secondary arc duration

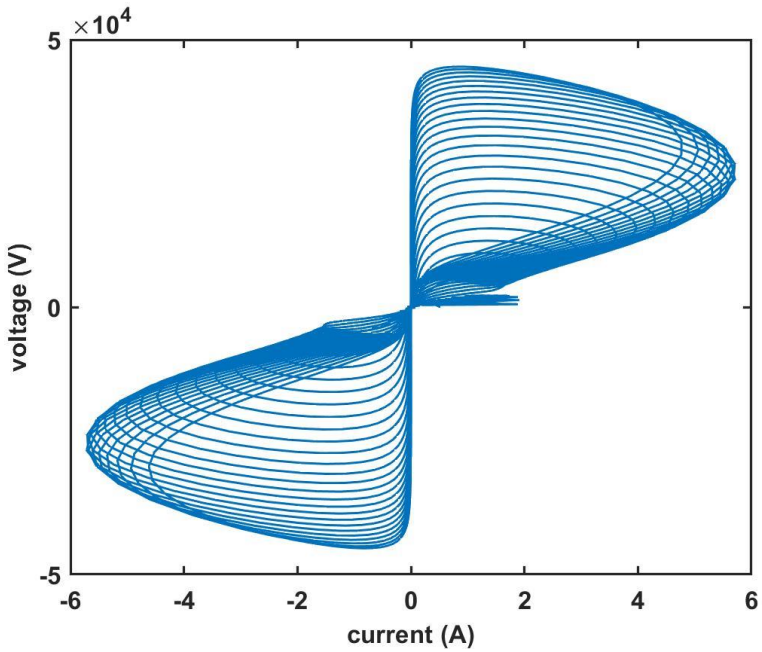

Figure 3.12 Current vs voltage curve of a secondary arc

3.6 Conclusion

The different arc behaviors are discussed in this chapter. The rate of change of the arc length affects the duration of the secondary arc. The longer the length of the arc, the shorter the secondary arc duration. Therefore, the arc extinction conditions should be carefully chosen to model the situation close to real life cases. The extinction of the secondary arc is influenced by external factors like the wind speed and the ionization of the air. When the wind speed is higher, then the arc length elongates faster, and the extinction time becomes shorter. It is also observed that decreasing the rate of change of the arc length, v_τ in equation (3.29) increases the duration of the secondary arc. The observations with the primary and the secondary arc simulations are summarized below.

- A reduced rate of the arc length results in an increased arc duration.
- An increased arc length leads to a lower arc time constant.
- Specifying the arc extinction criteria is very challenging due to the random behaviour of the arc and the arc extinction spread in literature.
- Lowering the rate of change of the arc length results in a higher magnitude of the secondary arc voltage. Reducing the initial arc length has the same effect.
- Reducing the source voltage also reduces the duration of the secondary arc, this is because capacitive coupling at the fault location reduces.

The arc model considers only the thermal property of the arc, the dielectric property and subsequent restrikes are not modelled.

4 Signal Analysis and Feature Extraction using Wavelet Transform

In most applications, the frequency domain analysis can give more insight about a phenomenon not apparent in the time domain signals. The application of signal processing has been used in many aspects of electrical power including protection relay applications, power quality analysis and harmonic analysis. The time domain waveforms obtained from the simulation of the disturbances in ATP are discussed in previous chapters. In this chapter, the discrete and fast wavelet transform are discussed as well as their applications in the feature extraction process. The feature extractions for the classification algorithm and the feature selection are also discussed. The frequency spectral and Poincare map are two of the commonly used methods for categorizing ferroresonance into different modes. The frequency spectral analysis is adopted in this thesis. Therefore, Fast Fourier transform (FFT), which gives a good frequency resolution of the signals is used for pre-classification of the ferroresonance disturbances.

4.1 Fast Fourier Transform

In order to develop an accurate classification algorithm, the initial classification of the training dataset must be done correctly. As discussed in Chapter 2, in addition to the periodicity of the waveform, the frequency spectrum of ferroresonance signals gives more insight into the mode of the disturbance. FFT function in MATLAB is used to determine the frequency component of the voltage and the current signals. Although the time resolution of the Fourier transform is poor, the frequency resolution is good enough for this analysis. The FFT function in MATLAB uses the Discrete Fourier Transform (DFT) for the transformation of a continuous time domain signal to the frequency domain. The choice of the sampling frequency and the number of samples per window affect the discretization of a continuous signal when using FFT. The number of samples per window and the sampling frequency must be an integer multiple of the fundamental frequency of the signal under analysis. i.e. When f_o is the fundamental frequency of the signal, f_s is the sampling frequency, N is the number of samples per time frame/window/period and let *m* be an integer greater than 1. Then;

$$N = m\frac{\mathrm{f_s}}{f_o} \tag{4.1}$$

The condition in equation (4.1) should be satisfied to prevent leakage at the frequency bin of the analyzed signal. Leakage is the approximation of the actual frequency spectrum of a signal by FFT when the condition in equation (4.1) is not satisfied [40]. In addition, the loss of signal information should be considered when choosing the sampling frequency. According to Nyquist theorem, the sampling frequency should be a minimum of $2f_m$, where f_m is the maximum frequency component in the signal of interest. Moreover, the computational burden increases with higher sampling frequency. Considering these factors, a sampling frequency of 10 kHz is adopted in this thesis. Furthermore, the performance of the FFT algorithm in MATLAB is improved by using a signal length that is a power of 2 or can be factorized into a product of small prime numbers. Otherwise the signal is padded with zeros to satisfy this condition. The longer the signal length, the higher the accuracy of the transformation from time domain to frequency domain [40]. To accommodate the two criteria, a signal length of 0.2 s with sample length of 2000 is selected for the spectral analysis. A different time frame is used in generating the training datasets.

4.2 Spectral Analysis of Ferroresonance with FFT

Ferroresonance pre-classification is done using the spectral property of the sustained period of the disturbance. The disturbance has three regions: the steady-state, the transient and the sustained period. The subharmonic ferroresonance is called subharmonic because of the subharmonic frequency in the sustained period. The spectral composition of each mode of ferroresonance in this project are discussed below, however, only the sustained period is analyzed.

4.2.1 Spectral composition of fundamental ferroresonance

The sustained period of the fundamental ferroresonance obtained from the simulation is shown in Figure 4.1. The sustained period wave shape is uniform and a duration of 0.2 s is chosen for this analysis. One of the major detrimental impact of the fundamental ferroresonance is the sustained overvoltage and overcurrent. The sustained voltage amplitude is approximately 690 kV which is roughly double the steady-state voltage of 324 kV. The sustained voltage can cause thermal and/or mechanical stress on the transformer when it is greater than its rated power-frequency short-duration withstand voltage.

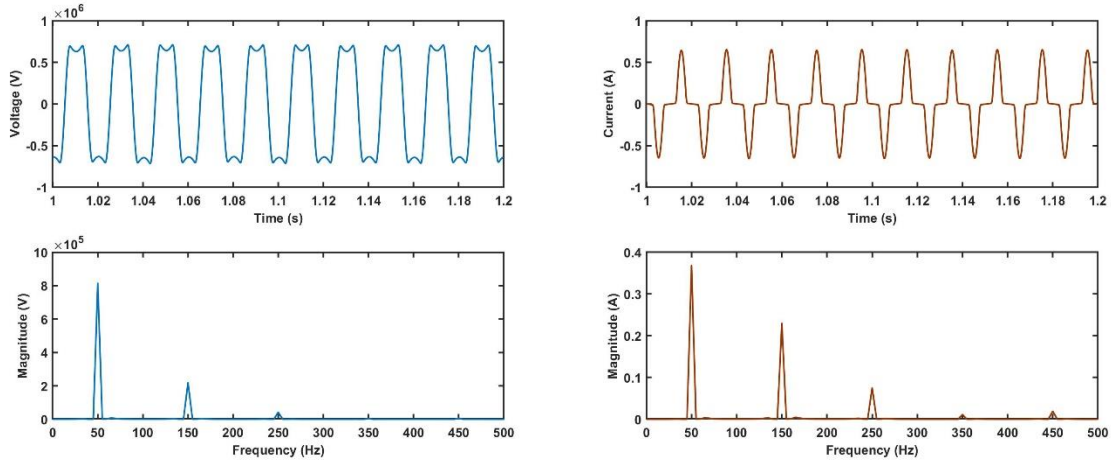

Figure 4.1 Spectral components of fundamental ferroresonance voltage and current

As seen in Figure 4.1, there is a high current spike due to the saturation of the magnetic component of the circuit. The current peak of 59.15 mA during ferroresonance is quite high compared to 5.5 mA during the steady-state. The overcurrent may cause overheating in the transformer and cause fire in some cases. Therefore, ferroresonance is a very severe disturbance that needs to be properly monitored to take control actions in order to prevent damages. The harmonic components of the fundamental ferroresonance voltage and current waveforms are shown in Figure 4.1. These are obtained by taking into account the leakage constraint with FFT in MATLAB and a proper selection of the sample points. The spectrum is dominated by the fundamental frequency component and odd harmonics. Subsequent waveforms with the same spectral components are classified as fundamental ferroresonance in this thesis. It can be observed that the 3rd harmonic component of the current is slightly higher than expected, the 3rd harmonic of current is approximately 64.9 % of the fundamental while the 5th is 25.4 %.

4.2.2 Spectral composition of subharmonic ferroresonance

The subharmonic mode of ferroresonance is dominated by sub-multiple(s) of the fundamental frequency. The period of the signal is an integer multiple, nT, of the source period. Using the period-x classification approach in [12], the subharmonic mode with a dominant frequency $\frac{f_0}{n}$ is a subharmonic of period-n. Where f_0 is the source fundamental frequency. The frequency spectra of the voltage and

the current signals are shown in Figure 4.2. It is a period 3 subharmonic ferroresonance because the spectrum has a fundamental frequency of 16.67 Hz $\left(\frac{50}{3}\right)$.

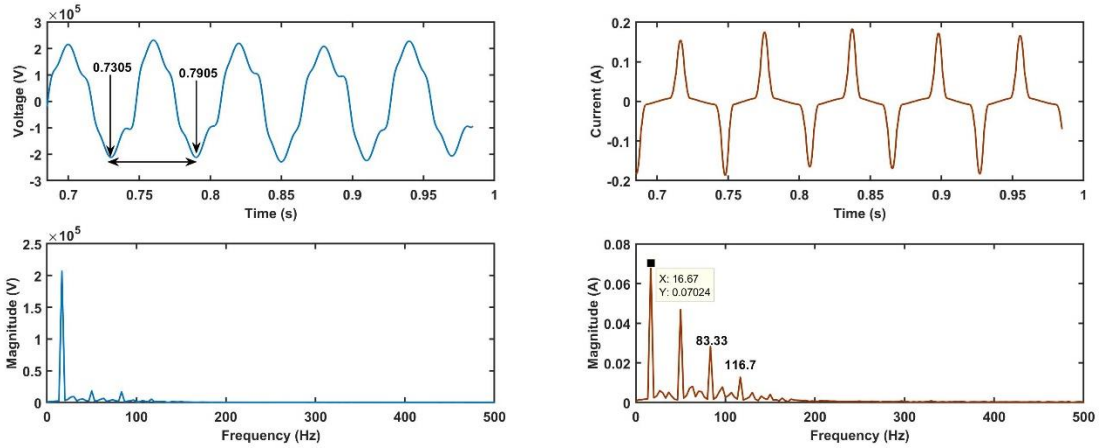

Figure 4.2 Spectral components of subharmonic ferroresonance voltage and current

4.2.3 Spectral composition of quasi-periodic ferroresonance

The quasi-periodic (QP) mode is not periodic but occurs almost regularly without an exact periodicity. The frequency spectrum of the voltage and the current are shown in Figure 4.3. There are at least two dominant frequencies in the spectrum, the fundamental (50 Hz) and one subharmonic (35 Hz). The main difference between the quasi-periodic and the chaotic ferroresonance is in the frequency spectrum. The frequency spectrum of the quasi-periodic ferroresonance is discontinuous while the chaotic mode has a continuous spectrum. The relationship between the two dominant frequencies in quasi-periodic is: $af_1 + bf_2$ where a and b are integer and a/b is an irrational real number [12]

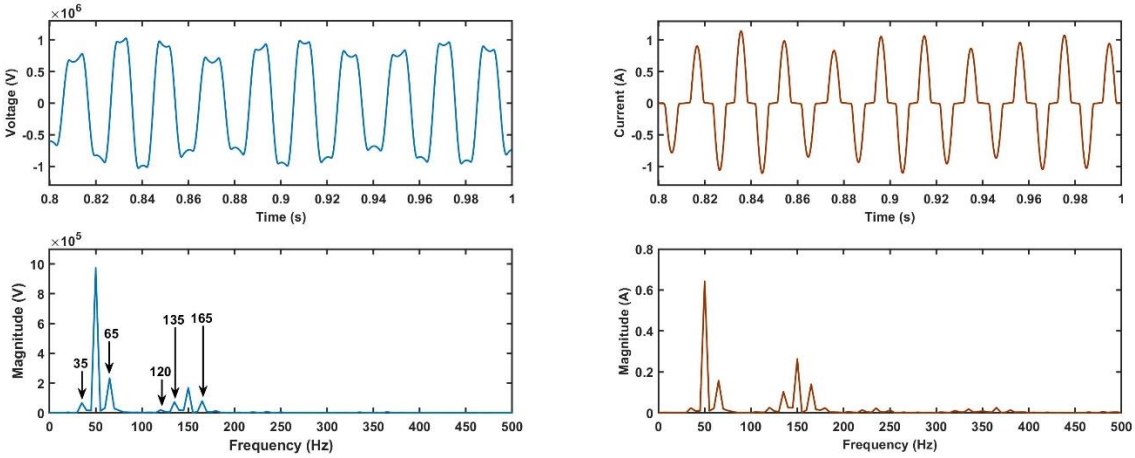

Figure 4.3 Spectral components of quasi-periodic ferroresonance voltage and current

All ferroresonance signals with spectral components similar to the one depicted in Figure 4.3 are classified as QP ferroresonance. There frequency components marked in Figure 4.3 are combinations of two dominant frequencies: f_1 =50 Hz and f_2 =35 Hz related as $af_1 \pm bf_2$. By assuming a=2 and b=1, the equivalent frequencies are: 65 Hz, 135 Hz. Other marked frequencies can be calculated in a similar manner.

4.2.4 Spectral composition of translational-chaotic ferroresonance

In the case of chaotic ferroresonance, the signal occurs randomly without a specific pattern. The signal has a transient behavior for the total duration of time without uniformity. The voltage and the current

spectral constituents are shown in Figure 4.5. Although there are some spikes at the fundamental frequency and the subharmonic frequencies, the phenomenon is still chaotic because of the broadband spectrum as shown in Figure 4.4 and Figure 4.5 There is a frequency spread between 0 to 50 Hz in the signal, it is more obvious in the current.

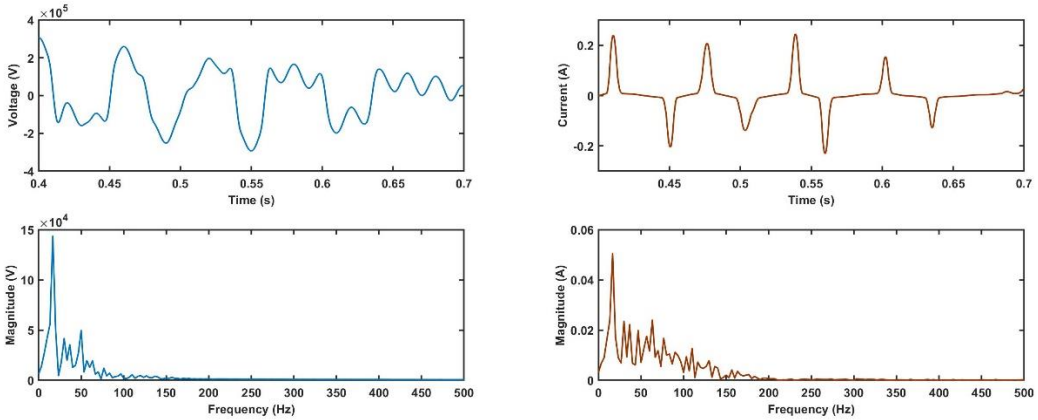

Figure 4.4 Spectral components of chaotic ferroresonance voltage and current -1

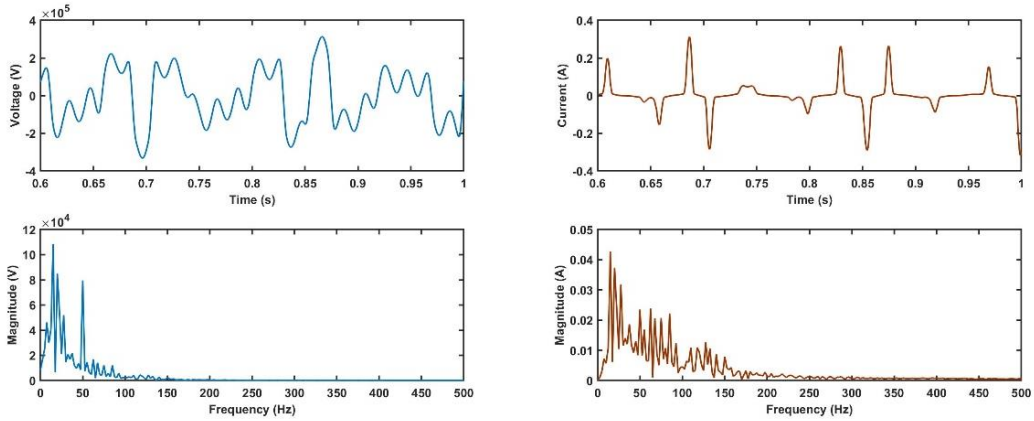

Figure 4.5 Spectral components of chaotic ferroresonance voltage and current - 2

4.3 Spectral Analysis of Arcing Signals with FFT

4.3.1 Spectral composition of elongated arc in the air

A modified version of the arc model presented in [25] is used in this thesis. The THD of the current and the voltage are compared to the original model. Figure 4.6 shows the FFT of the line voltage and the line current during the elongated arc fault in the air. The line voltage has a THD of 4.5074 % considering the 3rd to the 11th harmonic orders while the current has a THD of 2.66 %.

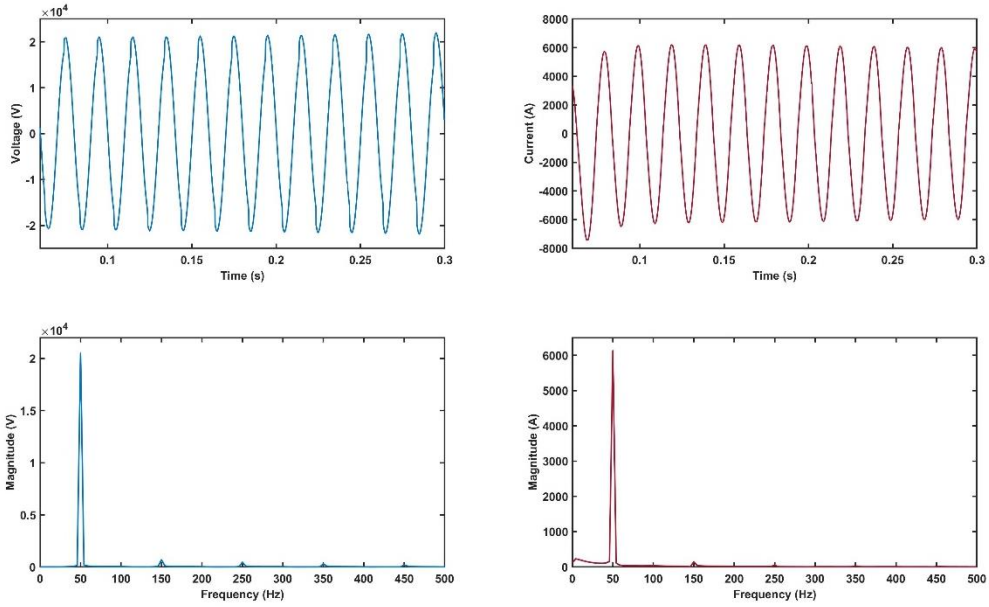

Figure 4.6 Spectral components of elongate air arc signal - voltage and current

4.3.2 Spectral composition of arcing signals: primary and secondary

The FFT of the primary arc current and voltage are presented in Figure 4.7 while Figure 4.8 shows the FFT of the secondary arc voltage and current. It can be observed from Figure 4.7 that the distortion is minimal during the primary arc compared to the secondary arc signals in Figure 4.8.

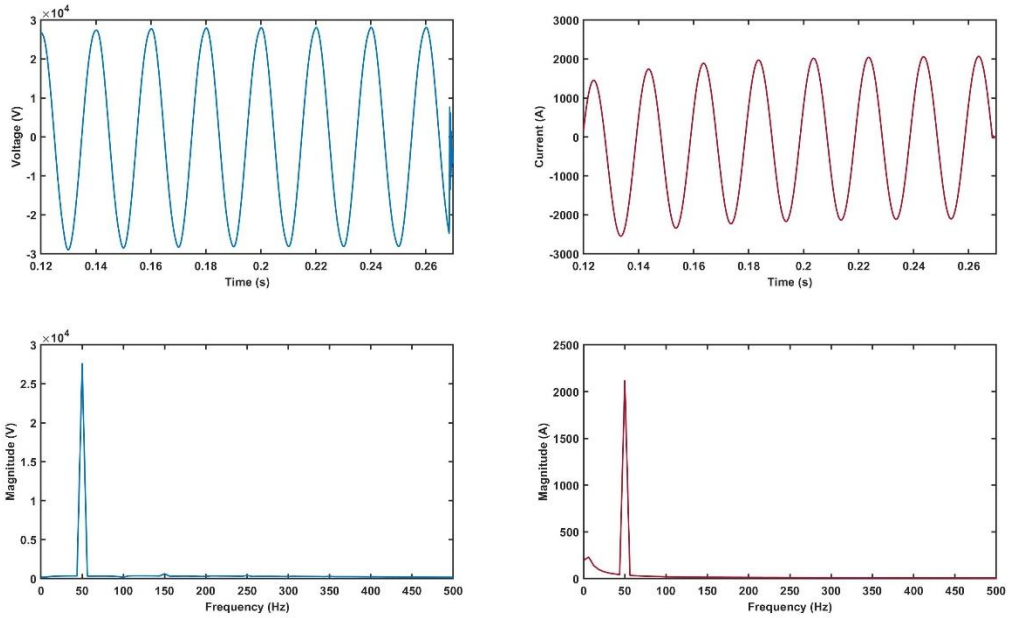

Figure 4.7 Spectral components of the primary arc signal - voltage and current

Since the secondary arc signal is caused by the capacitive and the inductive coupling between the healthy and the faulty phases, a higher harmonic content is preset in the current.

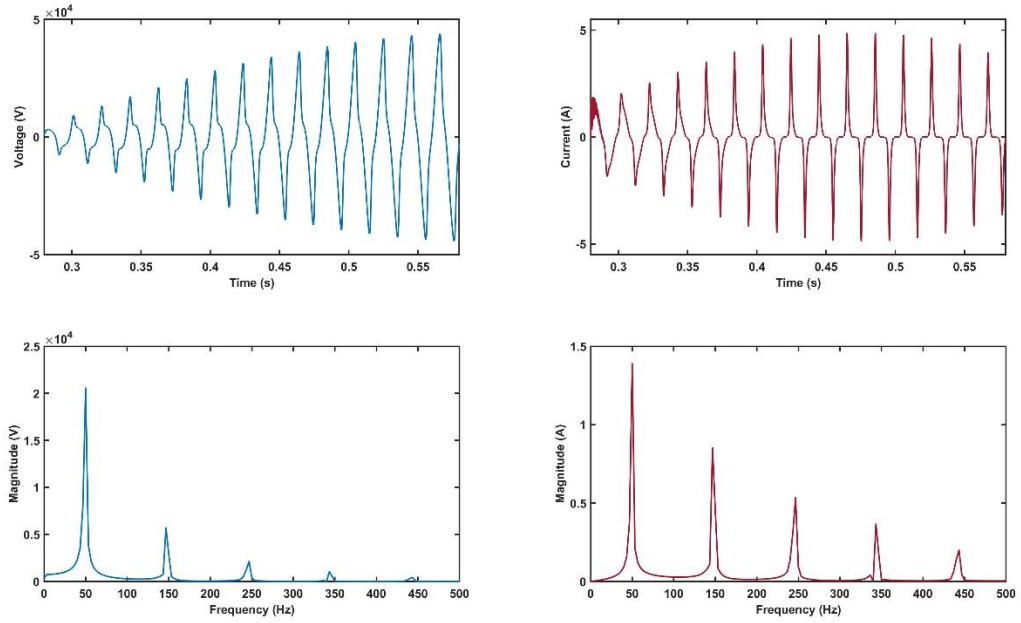

Figure 4.8 Spectral components of the secondary arc signals - voltage and current

4.4 Discrete Wavelet Transform

The Wavelet Transform (WT) has been used in many applications to transform time dependent signals into the wavelet domain. It has become popular in power systems due to its additional features over its commonly used counterpart, Short Time Fourier Transform (STFT). WT uses different scales to deconstruct a signal, which are equivalent to a low, a medium and a high frequency. This transform divides a given signal into different scales in which each scale components has a given frequency range [41]. It enables the visualization of the abrupt changes that are not obvious in the real time-series data. According to the authors in [42], the DWT is better for a non-stationary signal. WT gives better resolution in time domain because they are limited. Fourier transform on the other hand, assumes variation of the data up to infinity in order to transform the data from the time domain to the frequency domain. This data stretch to infinity makes the time localization very poor, moreover the assumption is not good for signals with sharp peaks and discontinuity. This makes DWT attractive for signals with fast peak and discontinuity because it can approximate data in finite domain. Individual wavelets are localized in space whereas individual sines and cosines are not. Frequency and space localization make the wavelet transform sparse in the wavelet domain. WT scales and dilates the mother wavelet using different resolutions at different levels to approximate a time series signal, in order to extract important features. The Continuous Wavelet Transform (CWT) of a signal $x(t)$ using a mother wavelet $\psi(t)$ is defined as:

$$\mathrm{WT(a,b)} = \frac{1}{\sqrt{a}} \int_{-\infty}^{\infty} x(t)\, \psi^{*}\left(\frac{t-b}{a}\right) dt \tag{4.2}$$

where $\frac{1}{\sqrt{a}}$ is a normalization vector, $\psi^{*}(.)$ is the complex conjugate of the mother wavelet $\psi(.)$, b is the translation factor while a is the scale or the dilation factor. DWT is obtained by discretizing the CWT and reducing the redundant data generated from the CWT. The mother wavelet is dilated discretely by the scale parameter and translated by the translation parameter a_o^u , $nb_o a_o^u$ respectively. u and n are integers; a_o and b_o are fixed values in which $a_o > 1$ and b_o >0. The DWT is defined mathematically as:

$$W(u,k) = \frac{1}{\sqrt{a_o^u}} \sum_n x[n]\, \psi^* \left(\frac{k - n b_o a_o^u}{a_o^u} \right) dt \tag{4.3}$$

A special case and the most popular implemented version of the DWT is the dyadic DWT in which a dyadic scale where $a_o = 2$ and $b_o = 1$ is used for discretizing the CWT. It is very useful when the time and the frequency localization are important in the analysis of a signal. Unlike the Fourier transform and the STFT, the resolution at different scales can be adapted for better time or frequency resolution. The STFT provides a uniform time resolution at all frequency. Additional advantage of using the DWT is the Multi-Resolution Analysis (MRA) of the fast wavelet transform that allows a high time resolution at a lower scale (high frequency) and a low time resolution at a higher scale (low frequency). Figure 4.9 shows the comparison between the frequency (scale) and the time resolution for the two transforms. The boxes represent the relationship between the frequency (scale) and the time. The STFT provides a time localization as seen in the figure, however, it is not adequate for signals with frequency changes [43, 44]. The area and dimension of the boxes at different frequency levels are the same for STFT while the area is constant in DWT but with different dimensions at different scales. Box 1 in the figure has a shorter width (high time resolution) and a longer height (low frequency resolution) at a high frequency (lower scale). The time resolution and the frequency resolution can be varied depending on the application and the feature of interest.

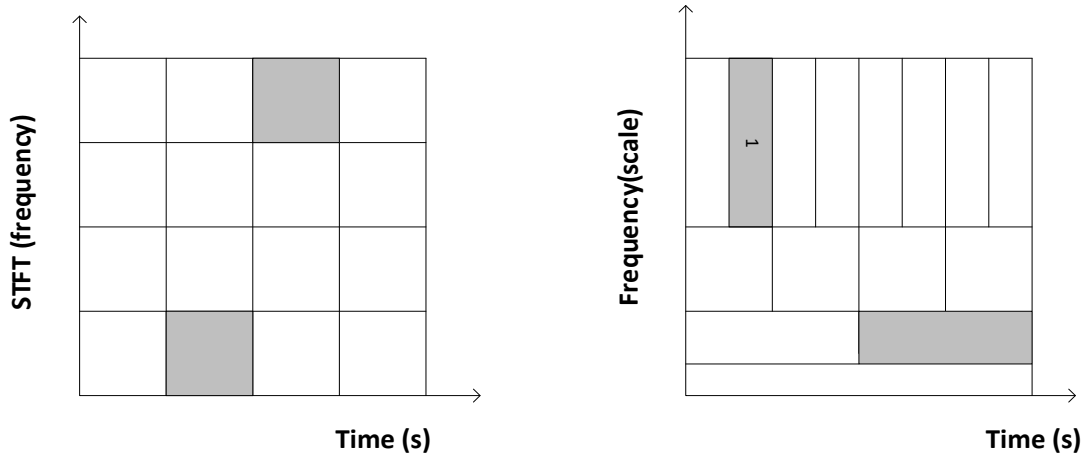

Figure 4.9 Frequency versus time plot for STFT & DWT

4.4.1 Literature Review on Wavelet Transform

Although WT was first introduced by a geophysicist J. Morlet for analyzing Seismic data [45], it has been widely used in power systems for the detection and classification of different power system disturbances. The application of the WT in detecting power quality disturbances are discussed in [46, 47]. The square of the wavelet coefficients were used by the authors in order to detect, localize and classify the different power quality disturbances. Another important criterion is the data compression feature of the DWT. The down sampling of the signal by 2 after filtering through the high and low pass filters enables the removal of redundant data. Consequently, the data size is reduced. This approach was used in [48] to reduce the data size for the power quality analysis. Not only is this transform used for detection, but also for power measurement as discussed in [49, 50]. The authors in [50] used the coefficients of voltage and current signals for RMS measurements and to estimate power/energy while Croes et all uses the WT to estimate the instantaneous active and the reactive power [49].

A transient signal especially in power systems is usually a non-stationary signal, the frequency of which changes with the time. The ability of the WT to use different mother wavelets (with different shapes) enables it to be a good fit for analyzing this signal [44]. Since the time localization is also important in some transient analysis, a lot of researches have used this WT feature in investigating transients in power

system [51, 52, 53]. Another application of the WT in power systems is in the investigation of high impedance arcing fault as discussed in [21, 33, 54, 55, 56, 57]. The DWT has also been used in investigating ferroresonance in power systems. The DWT was used in [15, 58, 17, 14, 16] to classifying ferroresonance signals from the other transients like capacitor switching, transformer switching and load switching. However, the focus of this research is on detecting ferroresonance and classifying it into different modes. Thus, an algorithm that uses DWT and pattern recognition approach to detect and classify different modes of ferroresonance and arcing faults is presented in this thesis.

4.4.2 Multi-resolution analysis: Fast wavelet transform

The Multi-Resolution Analysis (MRA) in DWT is more attractive for many applications. The DWT uses filters of different cutoff frequencies to analyze the signal at different scales [42]. The resolution is controlled by passing the signal through a series of high pass and low pass filters to analyze the signal. The high frequency coefficients are obtained by passing the original signal x[n] through a half band high pass filter g[n] and the low frequency is analyzed with a low pass filters h[n]. The scale is changed by up-sampling (increasing the signal samples by factor n) or down-sampling (reducing the signal size by factor n) [59]. The filtering of the signals through the low pass and high pass filters is equivalent to convolution of the signals. The down sampling of the signal by 2 after each filtering stage is represented by:

$$\mathrm{D[k]} = \sum_{n} x[n].\, g[2k - n] \tag{4.4}$$

$$A\mathrm{[k]} = \sum_{n} x[n].\, h[2k - n] \tag{4.5}$$

Where D[k] and A[k] are the outputs of the high and the low pass filters after down sampling by 2. g[n] and h[n] are mirror filters of each other and they are called quadrature mirror filter pair in signal processing [60]. They are related by:

$$\mathrm{g(n)} = (-1)^{1-\mathrm{n}}\, \mathrm{h}(1 - \mathrm{n}) \tag{4.6}$$

The wavelet function generates the detail coefficient associated with the high frequency while the scaling function generates the approximation coefficients related to the low frequency. The detail coefficients are appropriate for determining the fast variations in the signal while the approximation coefficients give better approximation of the signal with sparse coefficients and a compressed data. The MRA techniques in WT was introduced by Meyer and Mallat [60]. Figure 4.10 shows the decomposition level and change of frequency at different scales. It can be observed that the frequency is decreasing by order of 2^N at each scale. The maximum level of decomposition, m, of a signal of length N is determined by:

$$m = \log_2 N \tag{4.7}$$

The coefficients of the low pass (h) and the high pass filter (g) are defined depending on the mother wavelet and the number of vanishing moments. For the first level decomposition, the signal of length N is convulsed with h[n] to obtain the first level approximation coefficients of length $N + 2r - 1$ and with g[n] to obtain the first level detail coefficients of length $N + 2r - 1$; where $2r$ is the length of each filter. The obtained samples H and G (from h and g respectively) are then down-sampled by 2 to obtain A and D respectively with a length of $\frac{N-1}{2} - r$ each. For the second level decomposition, the same approach is used, however, the original signal is replaced with the first level approximation coefficient $A1$ to obtain $A2$ and $D2$.

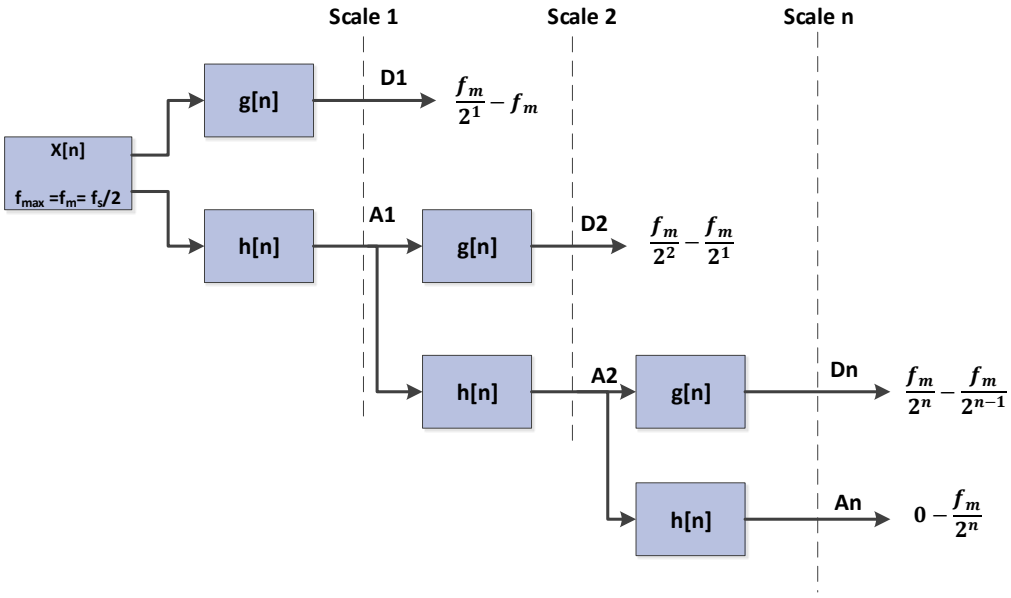

Figure 4.10 Discrete Wavelet transform decomposition

4.4.3 Choosing the mother wavelet

There are different mother wavelets and the choice of mother wavelet depends on the application. A mother wavelet must have a unity mean and a zero area. In choosing a mother wavelet, the regularity, the orthogonality (to preserve energy) and the number of vanishing moments must be considered. The similarity of the mother wavelet to the signal of interest is also important. Regularity of the mother wavelet affects the detection of an abrupt changes in the signal. Whereas a wavelet must have at least $n + 1$ vanishing moment in order to support a signal with n continuous derivatives. According to authors in [44], a shorter filter length is more suitable for transient analysis while a longer length is better for a low frequency analysis.

The common wavelet families for power system analysis especially for fast decaying signals are Daubechies and Symlets [33]. Different mother wavelets with varying vanishing moments are used to decompose the ferroresonance signals and arcing fault signals. Some of the results are depicted in the figures below. After careful consideration, Db4 is selected as the mother wavelet for this analysis. Db4 and Db6 give similar results, however, the number of coefficients is reduced by 4 when Db4 is used compared to Db6. A mother wavelet with a vanishing moment n, for instance, dbn, has a filter coefficient of length $2n$. Figure 4.11 and Figure 4.12 show a four-level decomposition of ferroresonance voltage signal using Daubechies (db4, db6), Symlets (sym4), Fejer-Korovkin filters (fk4) and Coiflets (coif2) mother wavelets.

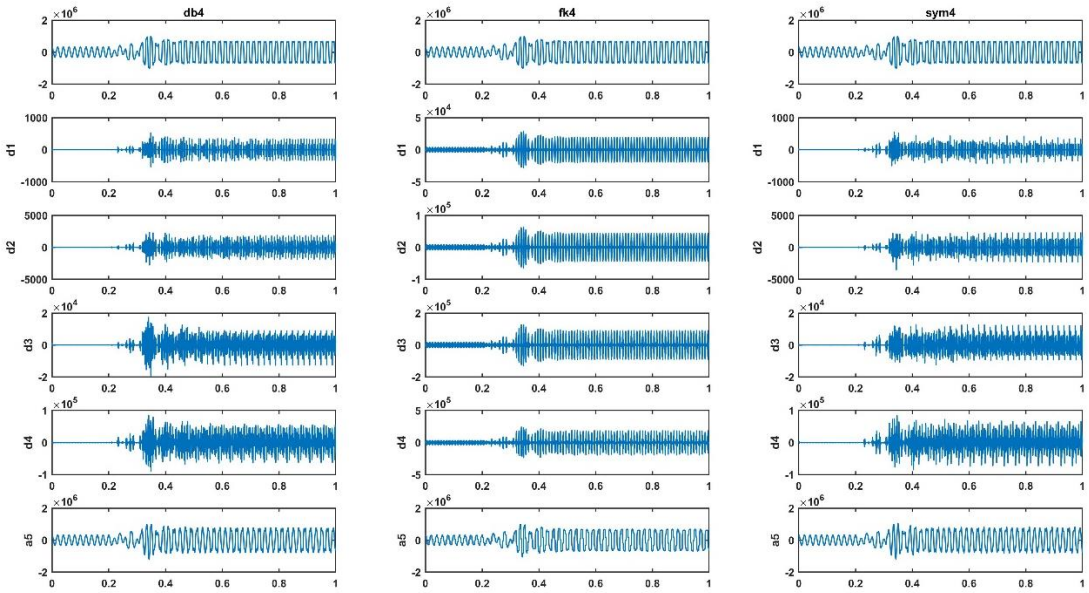

Figure 4.11 Four levels DWT decomposition of ferroresonance signal using mother wavelet 'db4', 'fk4' and Sym4

Figure 4.13 shows the decomposition of the primary and the secondary arc signal with different mother wavelets.

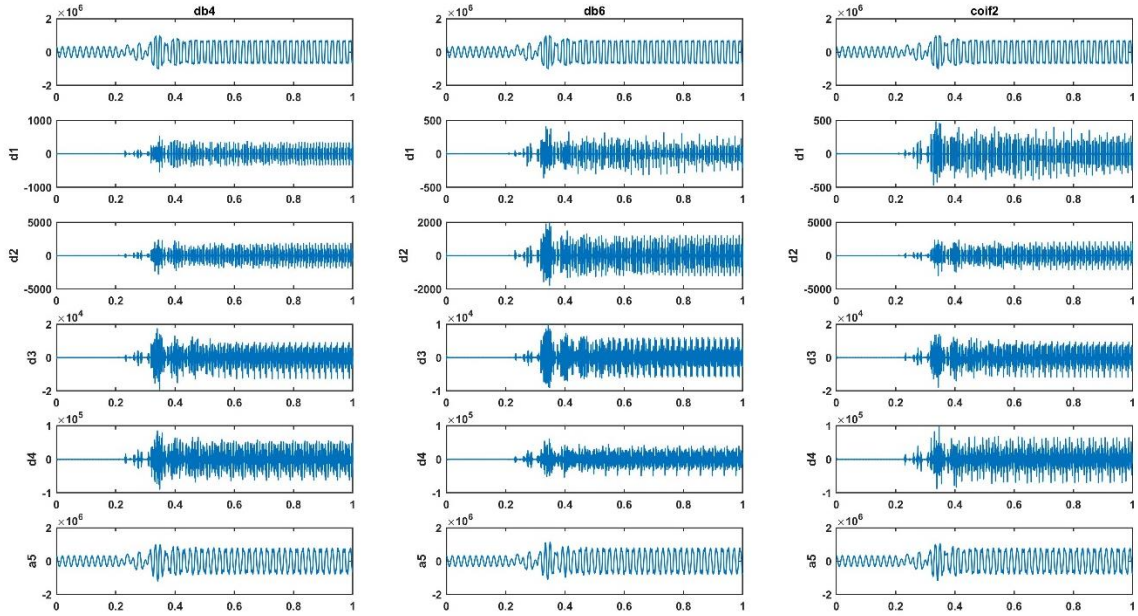

Figure 4.12 Four levels DWT decomposition of ferroresonance signal using mother wavelet 'db4', 'db6' and ‘Coif2’

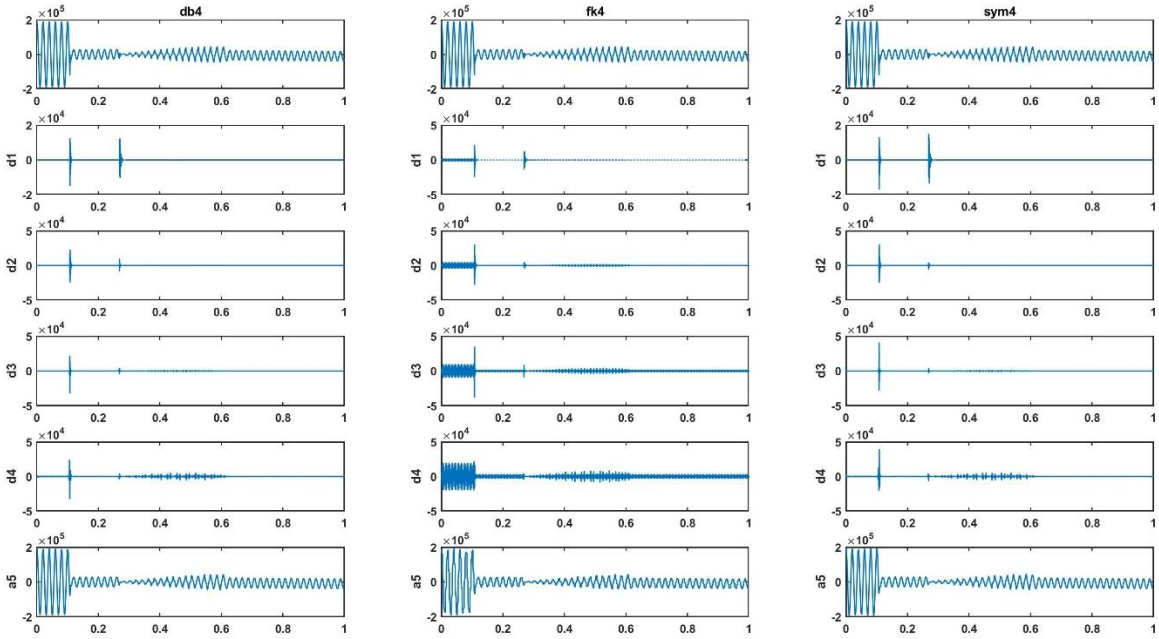

Figure 4.13 Four levels DWT decomposition of Arcing signal using mother wavelet 'db4', 'fk4' and Sym4

Three levels decomposition of the elongated air arc discussed in Chapter 2 is depicted in Figure 4.14

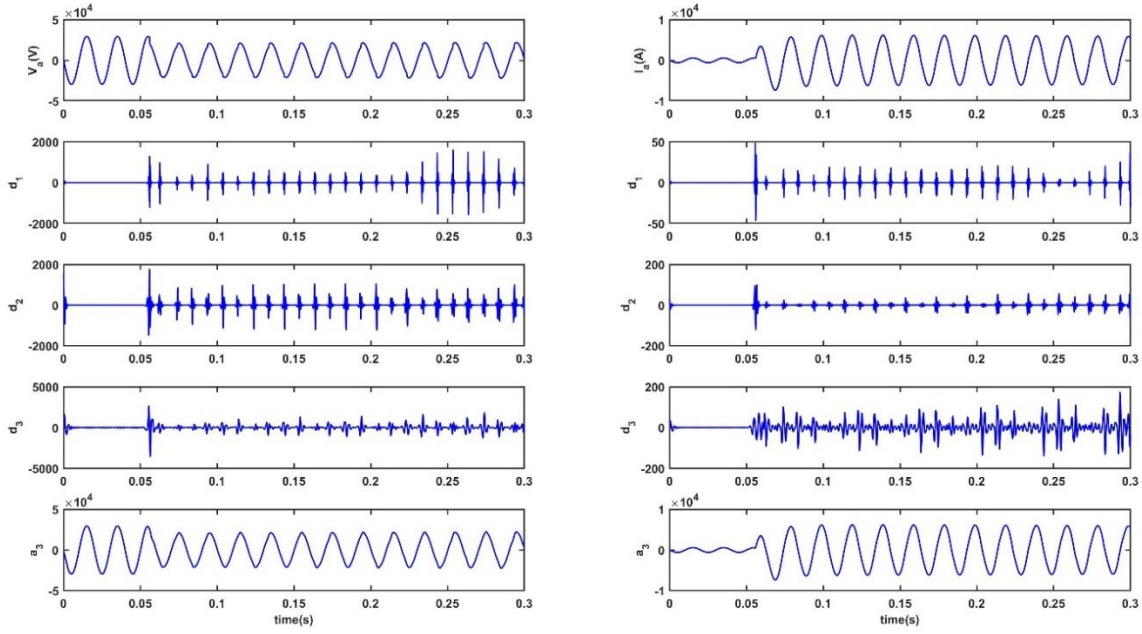

Figure 4.14 Three levels decomposition of elongated air arc voltage and current signal using db4

4.5 Feature extraction and selection

Feature extraction is an important phase in any classification algorithm, the extracted features are used as an input to the classifier. The best set of features are the ones that are closer to each other for the same disturbance class but far from other disturbances. The features space between different disturbances must be well separated in order to design a classifier with good performance [61]. Therefore, in order to extract features from the time domain signal of the voltage and current, a combination of DWT and

other statistical properties of the data are used. The DWT coefficients at different levels are manipulated in order to obtain features for the classification and the detection. The modifications considered are the energy of the coefficients, the sum of the absolute values of the coefficients and the peak of the absolute values of the coefficients. The modified signals show distinctive property that can be used to distinguish the different classes of the disturbances and some of them are discussed below. As it can be observed in Figure 4.12, Figure 4.13 and Figure 4.14, the coefficients are almost zero during steady-state operation but present spikes at the inception of the disturbance. The number of peak selected are varied from one to five to observe the impact on the classification algorithm. In order to reduce the feature space, a peak is selected from the detail and approximation coefficients of the three-phase voltage and the three-phase current signals. These make a total of twelve features per level (1 x 2 x 2 x 3).

From the Parseval's theorem, if the scaling and the wavelet function used for the DWT form an orthonormal basis, then the energy can be partitioned at different levels concentrated in the coefficients [2]. The mathematical expression is given by:

$$\mathrm{E}_x(\mathrm{k}) = \sum_{k=1}^{k_n} |D_x(k)|^2 + \sum_{k=1}^{k_n} |A_x(k)|^2 \tag{4.8}$$

where $\mathrm{E}_x(k)$ is the total energy of the signal, $\sum_{k=1}^{k_n} |D_x(k)|^2$ is the energy of the detail coefficients and $\sum_{k=1}^{k_n} |A_x(k)|^2$ is the energy of the approximation coefficients. The detail and approximation coefficients' energy over one cycle of a signal with length n are given by:

$$\mathrm{E}_d V(\mathrm{k}) = \sum_{h=k-W+1}^{k} |D_v(h)|^2 \tag{4.9}$$

$$\mathrm{E}_a V(\mathrm{k}) = \sum_{h=k-W+1}^{k} |A_v(h)|^2 \tag{4.10}$$

$E_d V$ is the energy of the detail coefficient of the voltage signal, h is used for the sliding window and W is the length of the signal over one cycle $\left(\frac{f_s}{f_o}\right)$. Similarly, the detail and approximation coefficients energy of the current signals, i_a, i_b, i_c are calculated using equation (4.9) and equation (4.10) respectively. These give a total of twelve (3 x 2 x 2) energy signals. Figure 4.15 shows the energy waveform for ferroresonance voltage signal.

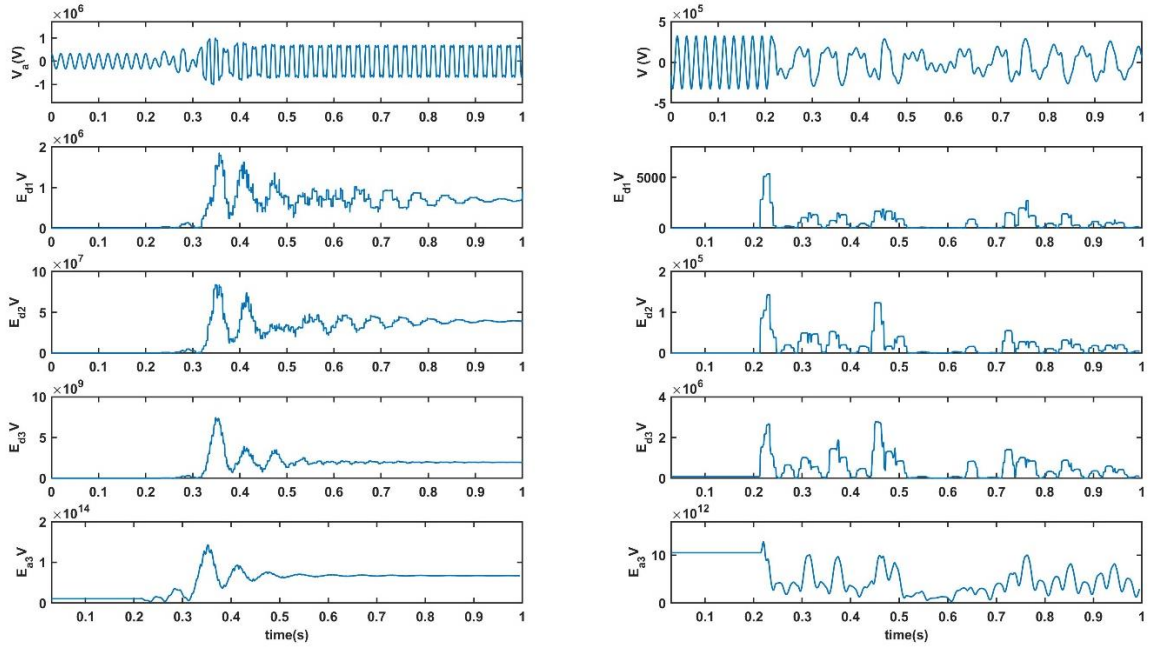

Figure 4.15 Energy of detail and approximation coefficients of ferroresonance voltage signal

Figure 4.15 shows the energy waveform for the primary and the secondary arc and elongated air arc voltage signals.

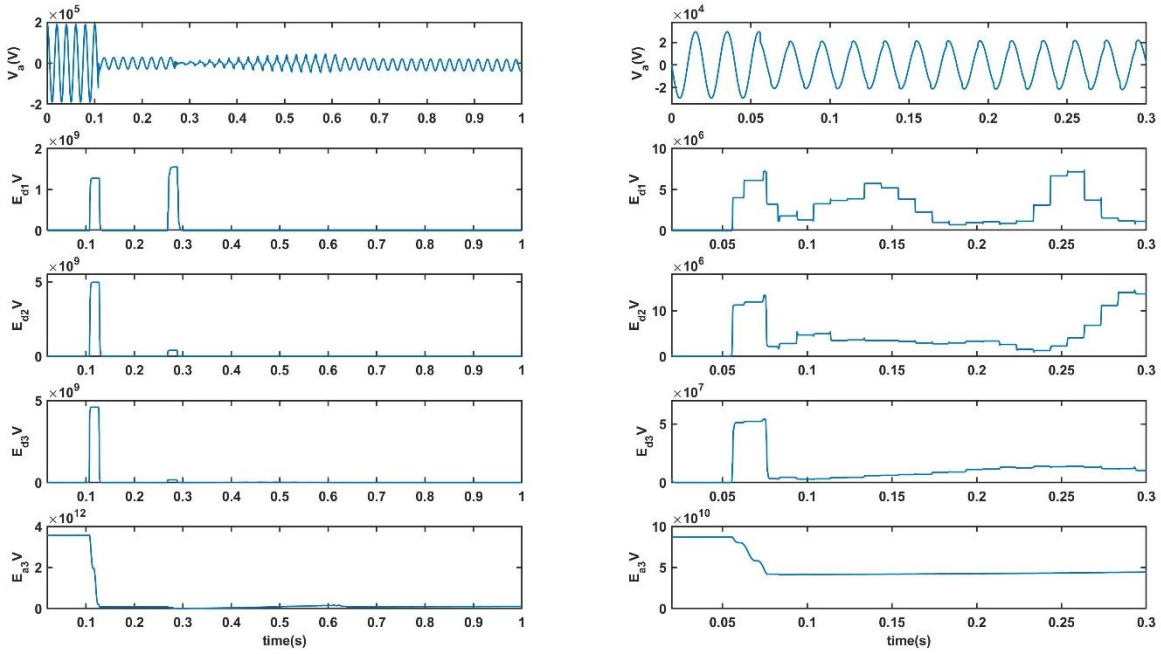

Figure 4.16 Energy of detail and approximation coefficients for: Primary and secondary arc; elongated air arc voltage signals

As it can be observed from the waveforms, the energy is constant during the steady-state period and the values fluctuate during the disturbance interval. The wave shape reflects the changes in the signal, it either increases or decreases depending on the type of the disturbance. The sum of the absolute values of the detail coefficients at different scales are also computed over a sliding window of 1 cycle. Figure 4.17 shows the waveform for the fundamental ferroresonance and the primary and secondary arc voltage signals.

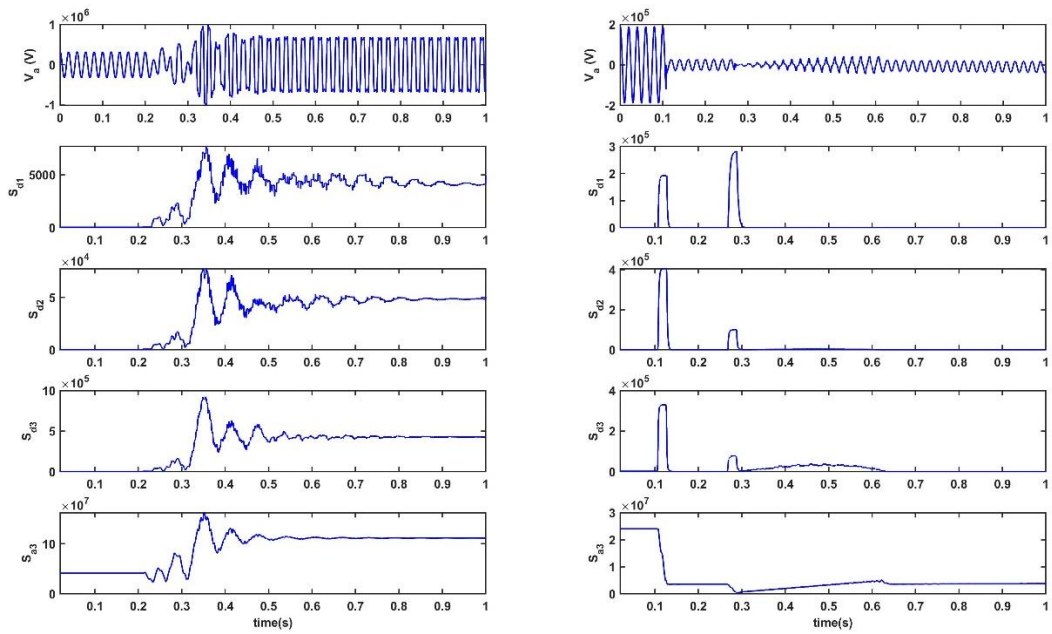

Figure 4.17 Sum of absolute values of detail coefficients over a sliding window of one cycle.

Another transform which is traditionally used for feature extraction is the Clarke transform. It transforms the signal with abc coordinates into $\alpha\beta 0$ coordinates. The mathematical expressions used for the processing of the voltage and the current signal by applying Clarke transform are given in equation (4.11) and (4.12).

$$u_{\alpha\beta 0}(t) = T_{\alpha\beta 0} * u_{abc}(t) \tag{4.11}$$

$$T_{\alpha\beta 0} = \sqrt{\frac{2}{3}} \begin{bmatrix} 1 & -\frac{1}{2} & -\frac{1}{2} \\ 0 & \frac{\sqrt{3}}{2} & -\frac{\sqrt{3}}{2} \\ \frac{1}{\sqrt{2}} & \frac{1}{\sqrt{2}} & \frac{1}{\sqrt{2}} \end{bmatrix}; \; u_{abc}(t) = \begin{bmatrix} u_a(1) & u_a(2) & \cdots & u_a(n) \\ u_b(1) & u_b(2) & \cdots & u_b(n) \\ u_c(1) & u_c(2) & \cdots & u_c(n) \end{bmatrix} \tag{4.12}$$

where n is the length of signal $u_{abc}(t)$. The RMS value of $u_{\alpha\beta 0}(t)$ over one cycle is computed and depicted in Figure 4.18. It can be observed that the value changes at the instant of the fault inception and the waveform is unique for each disturbance type. This modified signal provides information which is also used as additional input to the classifier. In order to avoid a high computational load, only the zero-sequence component is used since it provides enough information to distinguish each disturbance. Subsequently, the sum of the three-phase voltage and the three-phase current are used to obtain these components (I_o, V_o).

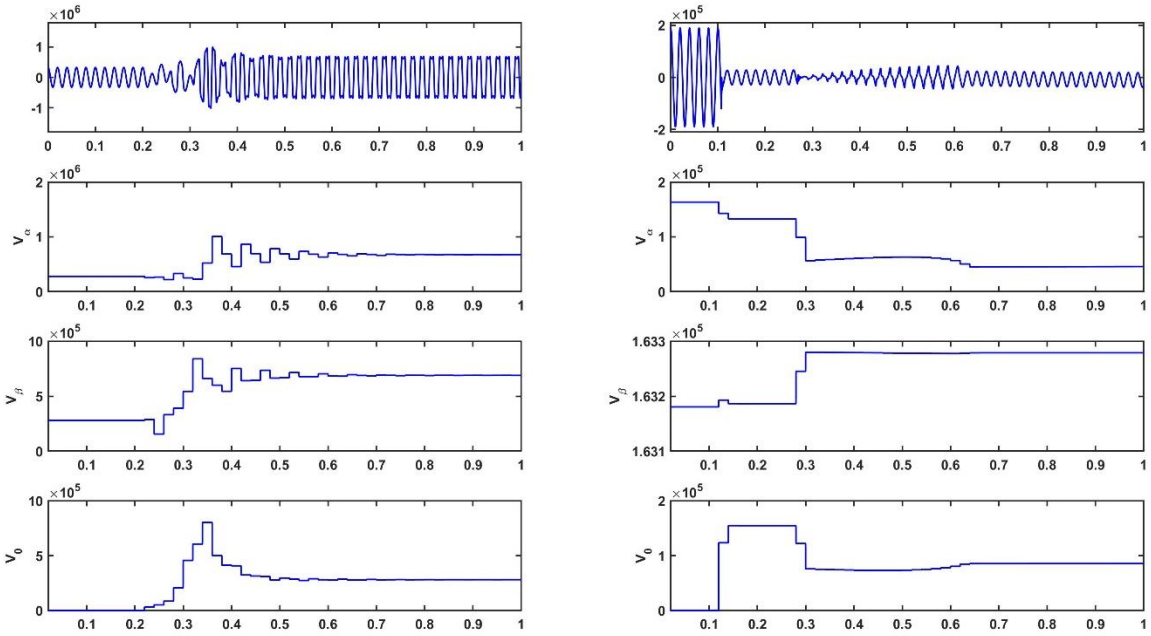

Figure 4.18 RMS value of Clarke transform coefficients over a sliding window of one power cycle: ferroresonance and arcing

From Figure 4.18, it can be observed that the zero-sequence component is zero before the disturbance inception while the $\alpha\beta$ components are non-zero and constant. For the ferroresonance signal, the zero-sequence waveform presents a constant value between 0.6 s and 1s when the ferroresonance is in the fundamental mode. Similarly, for the arcing fault signal, it can be observed that the value of V_0 ramps up at the inception of the primary arc and remains constant until the start of the secondary arc. Even though the values of $V_{\alpha\beta0}$ during the secondary arc are close to the values after the arc extinction, there are fluctuations during the secondary arc compared to constant values after the arc extinction. This feature can be used in combination with the other features to detect the arc extinction time.

For each of the features discussed above, 6 (2x3) values are extracted; three features from the three-phase voltage V_{abc} signals and three features from the three-phase current I_{abc} signals. Considering both the detail and the approximation coefficients for the peak, the energy and the sum of the coefficients extractions, there are in total 6 (2x2x3) signals per extraction. Therefore, a total of 36 (3x2x2x3) features are obtained from processing (manipulation) of the DWT coefficients per decomposition level. The features are extracted from one level in order to reduce the dimension of the feature space (feature vector). The second and the third DWT decomposition levels with frequency range of 0-2500 Hz at 10 kHz sampling frequency are considered. Similarly, a total of 6 (3x2) features can be extracted from the Clarke transform; $V_{\alpha\beta0}$, $I_{\alpha\beta0}$. These 42 features are represented in the column of the feature vector. The reduction of the dimensionality of the feature vector can improve the performance of the classifier, hence, the features are further reduced. As mentioned earlier, the zero-sequence component provides adequate information that can be used to classify the disturbances and it is also easier to determine ($I_o = I_a + I_b + I_c$). Hence, $V_{\alpha\beta}$, $I_{\alpha\beta}$ can be discarded. Similarly, only the sum of the detail coefficients of voltage signals are considered. The current signals detail coefficients are discarded, and the approximation coefficients for both the three-phase current and voltage signals are discarded as well. The remaining 33 features are further processed and used in the classification algorithm. The features selection process in MATLAB classification learner app, in statistics and machine learning tool box, is explored during the training phase. Different classifiers are trained with different combinations of features in order to obtain the optimum solution for this problem.

4.6 Conclusion

The advantages of using DWT over FFT in signal processing are discussed in this chapter. The DWT is adopted due to better time localization and its ability to represent non-stationary signal well. The regularity, the number of vanishing moments, similarity of the mother wavelet to the signal of interest are considered while choosing the mother wavelet. The multiresolution analysis of the fast wavelet transforms gives a better time resolution at high frequency, this property is used for the time localization of the disturbances. The features extraction is important for classification algorithms, as they give local information that can be used to detect and classify the disturbances. It can be concluded that the modification of the coefficients gives sufficient information that can be used in extracting hidden features from the time domain signals. Therefore, DWT is an efficient tool for feature extractions for the proposed algorithm.

5 Detection and classification algorithms

The detection techniques adopted in this thesis are discussed in this chapter. The superimposed components of voltage and current signals ($\Delta I, \Delta V$) are used as fault signatures to detect the inception of the disturbances. The DWT coefficients are used for the time localization of the disturbances and features' generation for the classification algorithm. Different optimization techniques which are adopted to reduce the computational burden and memory are also discussed. The absolute sum of the detail DWT coefficients, the peak of the absolute values of the DWT coefficients and some other statistical properties of the signals are used in generating features for the classification algorithm. The proposed algorithm can detect and classify different modes of ferroresonance and arcing signals by using the modified wavelet coefficients and zero-sequence voltage and current. The first stage comprises the detection of the fault signatures whilst the second stage deals with the application of the classification algorithm.

5.1 Proposed Detection Approach

Continuous overvoltage and saturation of a ferromagnetic equipment during ferroresonance requires a short time detection window in order to prevent equipment damages. Moreover, the system should be restored as fast as possible after secondary arc extinction to reduce the reclosing time. Therefore, a window of one cycle is used to analyze the time series signal of both disturbances. However, in order to distinguish between the different modes of ferroresonance, a shorter time window might be too small to confirm the chaotic and the quasi-periodic modes that oscillate between different modes. Therefore, a classification interval greater than one window is specified. A fast detection scheme using the superimposed component of the current and voltage is presented in this thesis. During steady-state conditions, the signal over a time interval of one period T should be equivalent to that provided one cycle earlier when there is no external influence or changes in the network. When a transient condition occurs, at least one of the voltage or current signals present a value greater than the steady-state value. Figure 5.1 shows the superimposed calculation of seven cycles of an arcing fault signal; three cycles before the arc inception and four cycles from the arc inception. As can be observed from Figure 5.1, the superimposed component presents a high value at transient inception. The marked disturbance inception time indicates the beginning of the primary arc. The superimposed value of the three-phase currents and the three-phase voltages are calculated using equation (5.1) and (5.2) respectively.

$$\Delta I_{abc}(k) = |I_{abc}(k) - I_{abc}(k-T)| \tag{5.1}$$

$$\Delta V_{abc}(k) = |V_{abc}(k) - V_{abc}(k-T)| \tag{5.2}$$

where T represents the number of samples per cycle. Similarly, the superimposed components of ferroresonance signals are also determined. A threshold is then set for the current signal and another threshold is set for the voltage signal. Since the current magnitude of all the disturbances have a wide gap, a combination of superimposed currents and voltages are used for the detection of the disturbances. Different models are used for the disturbances' simulation and at different voltage levels, therefore, ΔV are normalized with the corresponding base voltage to obtain values within the same range. The equivalent superimposed voltage component is computed as:

$$\Delta V_{abc}(k) = \frac{|V_{abc}(k) - V_{abc}(k-T)|}{V_{base}} \tag{5.3}$$

Consequently, any value above the threshold is categorized as a faulty state. The superimposed technique adopted in the detection of the disturbances is also used in protection relays to detect faults as discussed in [62]. The flow chart in Figure 5.2 shows the detection scheme.

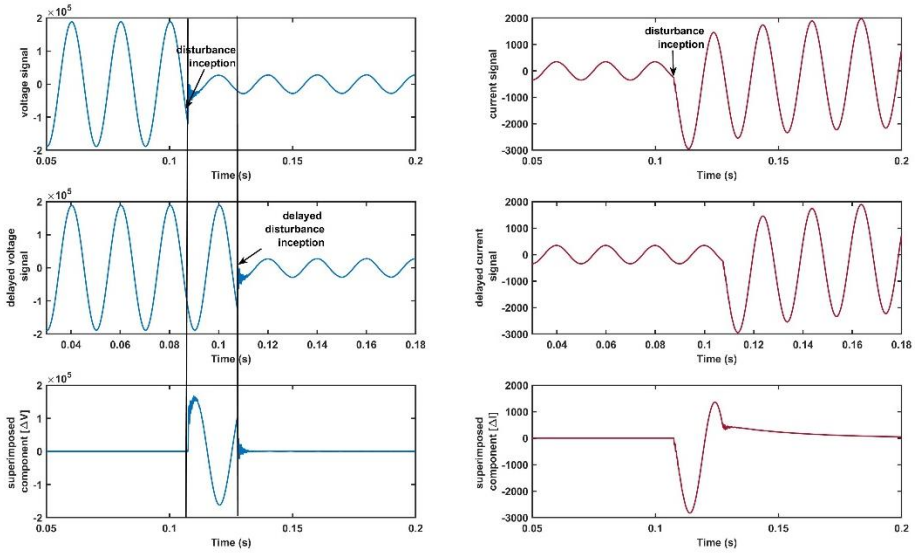

Figure 5.1 Superimposed component: arcing voltage and current signals

In Figure 5.2, k represents the number of samples per window. The calculated values of $\Delta I, \Delta V$ are compared to the thresholds for a duration of $\frac{k}{10}$ samples, implemented with count1 in Figure 5.2.

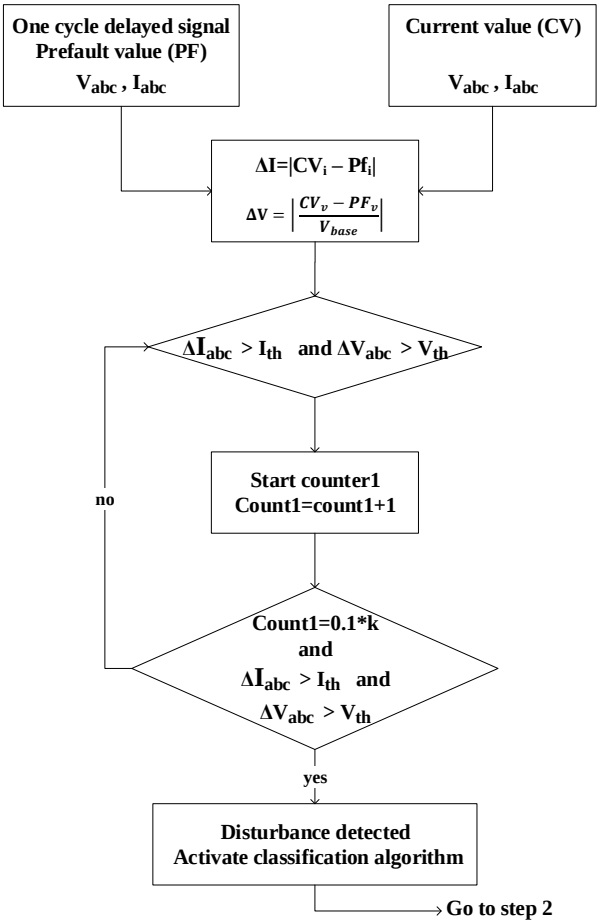

Figure 5.2 Disturbance detection scheme

When the superimposed components still present values above the threshold at the end of this period; the disturbance occurrence is confirmed and the second step is initiated.

The disturbances are classified in the second stage, step 2. Because the disturbances occur occasionally in power systems, this easy detection scheme is expected to reduce the computational burden and save memory. Therefore, the DWT and other features are extracted when the *Go to step 2* signal in Figure 5.2 is activated.

5.2 Classification of disturbances

The phase after the detection is the classification of the disturbances into their corresponding classes. Figure 5.3 shows the step-by-step approach adopted in this study. The features considered in the study are discussed in detail in Chapter 4. These features are used in the first phase of the classification algorithm to generate the datasets.

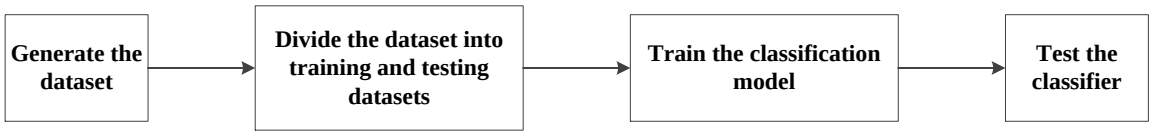

Figure 5.3 Flow chart of classification algorithm development

5.2.1 Datasets for classification

Datasets are generated from set of samples (patterns) from the disturbances of interest in order to design and evaluate the pattern recognition algorithm. The objective of the algorithm is to classify the disturbances, and therefore the data samples representing the disturbance duration are used to train the classifier. The steady-state signals and post disturbance signals are removed from the simulation results; only the extracted disturbance data samples are used to generate the datasets. The signals are pre-processed with the FFT, especially the ferroresonance signals, as discussed in Chapter 4 in order to assign class label to each disturbance data. The data labels are generated using the name of each disturbance. The extracted disturbance signal lengths are in the range of 0.35 s to 2 s. In order to reduce the length of the time series and obtain compact forms of the signals without losing their properties, the signals are partitioned into a shorter length of one cycle (200 samples at $f_s = 10$ kHz) with an overlap of 5 ms (50 samples at $f_s = 10$ kHz). These set of sequences provide information at different interval of the original signal that are used as training dataset to classify the different disturbances. The data is normalized in order to prevent the occurrence of numerical errors in the design and implementation stage of the algorithm. Three normalization techniques are implemented in the algorithm. These are:

1. Normalization with the mean and the standard deviation

$$x_{new}(i) = \frac{x(i) - \bar{X}}{\sigma} \tag{5.4}$$

2. Normalization with the base voltage and current (p.u method)

$$v_{new}(i) = \frac{v(i)}{V_{base}} \; ; \; i_{new}(i) = \frac{i(i)}{I_{base}} \tag{5.5}$$

3. Normalization with the minimum and the maximum value

$$x_{new} = \frac{x - X_{min}}{X_{max}} \tag{5.6}$$

The user can select the normalization of interest during the feature generation stage. It should be noted that the same normalization scheme used in the training phase should be adopted in the testing phase. The columns of the datasets represent the features while the rows represent the observations. Figure 5.4 depicts the steps in the dataset generation algorithm. The sampling frequency, the overlap percentage and the level of decomposition of the DWT are the required inputs. The window size is also specified as an input to the algorithm. In order to avoid signal overlap between different disturbances, the feature generation's start and end points for each extracted disturbance data j are conditioned to be an integer. In Figure 5.4, j represents the index of each simulation. For instance, assuming there are 20 simulations of the fundamental ferroresonance disturbance in ATPDraw, then j=1,2,…,n and therefore, $n = 20$ and j=2 for the second extracted disturbance. Each simulation (j) extracted disturbance data must be conditioned to be an integer taking the window size and the overlap into consideration.

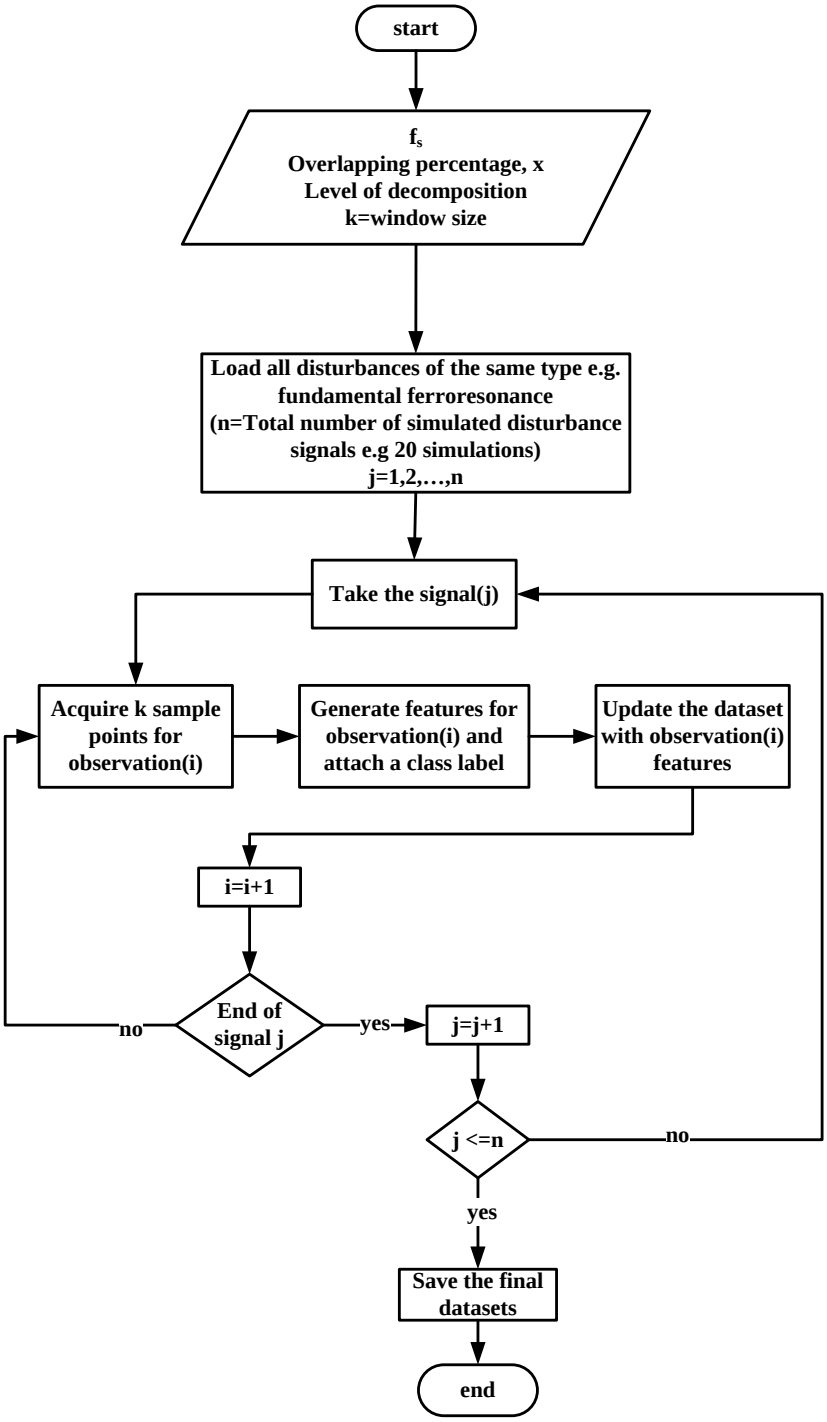

Figure 5.4 Step-by-step approach to generate dataset for all disturbances.

The classes of disturbances considered in this project are: three-phase fundamental ferroresonance, three-phase chaotic ferroresonance, AB fundamental ferroresonance, BC fundamental ferroresonance, single phase elongated air arc, secondary arc, no ferroresonance. Figure 5.4 represents the dataset generation for one class. A data of specified length k is acquired at every point and features are generated. It should be noted that only a x % data overlap exists between consecutive windows. This runs continuously until the end of the last data sample ($j = n$) in the corresponding class. The process depicted in Figure 5.4 is repeated for all the classes to obtain the total dataset of N rows (observations) and M columns (features). The total dataset used in training the classifier has 32 columns, the first 31

columns represent the features while the last column represents the class label. Since the datasets are generated sequentially, the rows of matrix are arranged randomly. Then, the dataset is divided into 2 parts: a training dataset (75 %) and a testing dataset (25 %). The training set is used for training the algorithm while the testing dataset is used to test the performance of the trained algorithm. It is better to test the algorithm with the dataset different from the training set to accurately evaluate the classifier performance. This will prevent the memorization of the input in order to classify the data.

5.2.2 Classification algorithm design

There are many types of classifier used for pattern recognition. The common ones are support vector machine (SVM), decision tree (DT), k-nearest neighbor (kNN), naïve bayes classifier, ensemble bagged trees etc. There is no single rule for selecting a classifier for an application. Some of the important factors to consider are the datasets, the objective of the classification, the type of applications, the speed and accuracy, the memory consumption and so on. Since the disturbances and the corresponding types (class) are known, supervised learning is adopted for this study. In this work, different classifiers are trained with the generated training dataset using the classification leaner app in MATLAB to determine the best fit. Three out of these SVM, k-NN and DT are selected and evaluated for the proposed algorithm. New datasets are predicted by feeding the data, in the same format as training dataset, into the classifier. It is assumed that only one disturbance class occurs at a time. One of the objectives of this work is to determine whether this algorithm is well suited for real-time applications. In order to ensure this, the speed of prediction of new data samples and memory consumption are crucial. Another factor to consider is the size of the features, reducing the dimensionality of the features will reduce the computational burden and time. After careful observations and several training processes, 7 out of the initial 31 features are found to be sufficient to classify the signals. After considering all options and conditions described above, the decision tree is selected as the final classifier for the project. It is the preferred classifier for this problem due to its speed and training time, simplicity, accuracy and ease of understanding. It gives similar accuracy compares to the k-NN and SVM classifier, but the fast prediction speed makes it a more convenient choice for real-time applications evaluation.

5.2.3 Decision tree and performance metrics of classification algorithm

The decision tree can be combined with fuzzy logic approach to make it more robust and immune to noise [15]. The decision tree split criteria used in MATLAB classification learner app are the Gini's diversity index, the twoing rule and the maximum deviance reduction split criteria. The tree starts with a root, then the nodes which are interconnected by the branches. The last nodes of the tree are called leaves, and these represent the final class of the disturbances. At the first node, the classifier analyses all the available features and compare them with the trained model to split the node. The number of tree branches also affect the complexity of the tree. Here, it is set to a maximum of 20 to reduce the complexity of the tree. Another concern about using the decision tree is overfitting of data due to sharp requirements used at every node. This can be overcome by using different decision trees bagged together as ensemble trees. However, ordinary decision tree gives a good result for this problem. The confusion matrix that shows the true positive rate of each disturbances is depicted in Figure 5.5. The overall accuracy of the model is 99.8%.

The *k*-fold cross validation is used to validate the accuracy of the classifier while training. In the *k*-fold cross validation approach adopted in this model, the data is partitioned into *k*-folds and the accuracy is estimated on each fold; therefore, the overall accuracy of the model is the average of all fold's accuracies. This method helps in fine tuning the performance of the classifier to avoid overfitting. The performance is evaluated by the overall accuracy, specificity and sensitivity. Sensitivity, also called the true positive rate, is a metric that measures the number of actual disturbances that are correctly classified as disturbances.

$$Sensitivity = \frac{True\ Positive}{True\ positive + False\ negative} \tag{5.7}$$

While specificity, true negative, measures the percentage of actual negatives that are classified as negatives. The specificity of the classifier is given as:

$$Specificity = \frac{True\ Negative}{True\ negative + False\ positive} \tag{5.8}$$

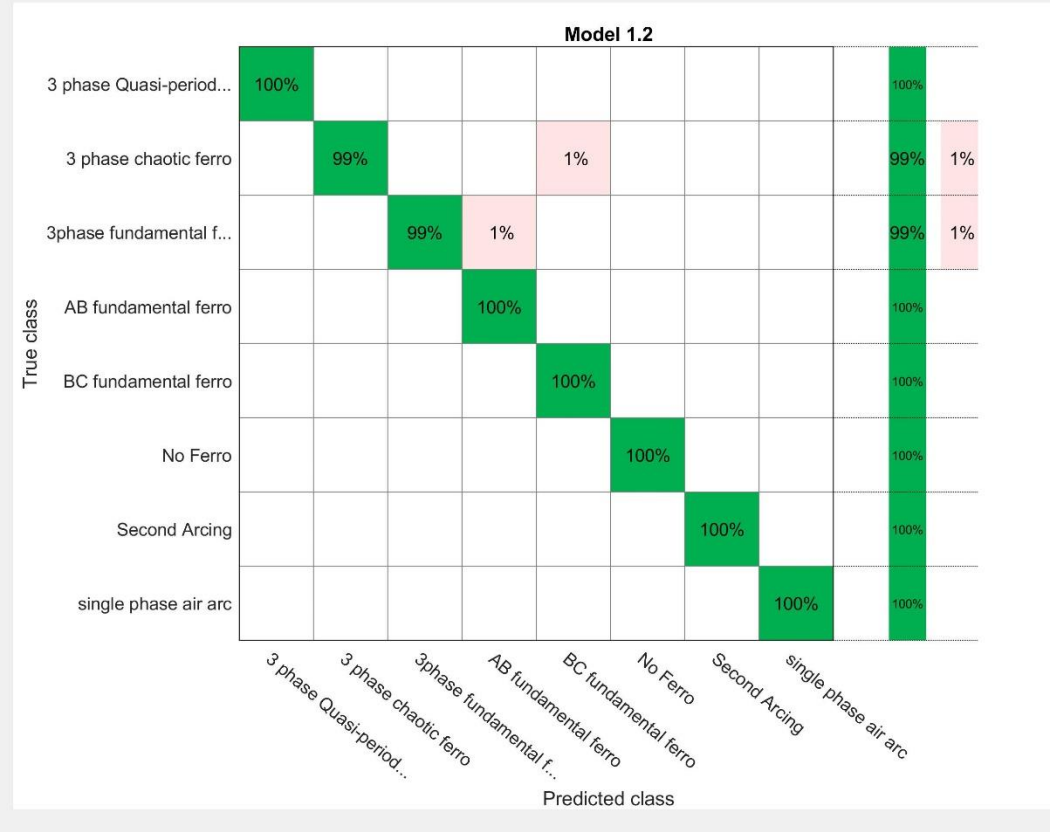

Figure 5.5 Confusion matrix of trained decision tree for all disturbance classes

The important metrics to evaluate the performance of the classifier is dependent on the objective of the classification algorithm. False tripping or no detection of disturbances can create issues in the network. The major objective of this project is monitoring, the capability can be improved in future for control activities in the network. Consequently, the overall accuracy, sensitivity and specificity, evaluation results are used for measuring the performance of the classifier. Since the focus of the proposed algorithm is on ferroresonance and arcing faults, other types of disturbances in the network are not considered.

5.3 Final detection and classification approach

This study is aimed at developing a detection scheme that detect the disturbances using the voltage and current signals. The detection and classification are built in MATLAB, and the data used are extracted from EMTP simulations. One classifier is trained for both disturbances. Superimposed components are used to detect the disturbance inception period in order to save computational space. The system is evaluated with new sets of data, not included in the design and testing of the classifier, in order to evaluate the system performance in the simulated the real-time scenario with MATLAB for-loop. This is to ensure the disturbance detection are accurate when the signal has steady-state and post fault signals. A classifier must be able to map an unlabeled time series data to a set of defined classes in order to

classify new data. For a real-time application, the computation workload, speed and memory are some of the concerns. In the implementation of the proposed algorithm, the algorithm is optimized to reduce redundant data and avoid unnecessary computation. The final algorithm implementation is divided into 5 steps, the first step is the detection of the disturbance as described above. Other steps are explained below.

5.3.1 Step 2: Classification of the disturbance

After the disturbance is detected in step 1, the classification is performed for a specified window of three cycles. The two major steps at this stage are the feature generation and new sample prediction. During this period, a sliding window is used to collect the signal data used as the input to the classifier. This step is optimized by reducing the evaluation rate to 4 times per defined window, a signal length of one cycle *k* is acquired four times per window. This is implemented by using the decision block marked 2 in Figure 5.6. This approach is adopted, instead of a sliding window of one data point increment, to reduce the computational burden. Consequently, 4 predictions are obtained per window and the final output is the common predicted class from the four predictions. This is to ensure correct classification and reduce the false positive rate with the assumption that one disturbance occurs at a time. The classTime in Figure 5.6 indicates the number of windows over which the classification is continuously done. It is set to three cycles, as such three different results are obtained from this step. This shows the first indication of the disturbance type. The expected result from the secondary and primary arcing detection is to determine the arc extinction time, as such, the classification window of three cycles is too small to evaluate this. Moreover, continuous computation over the duration of the signal will provide redundant data and consume memory. This leads to the next step where an adaptive time is proposed as a solution to this problem.

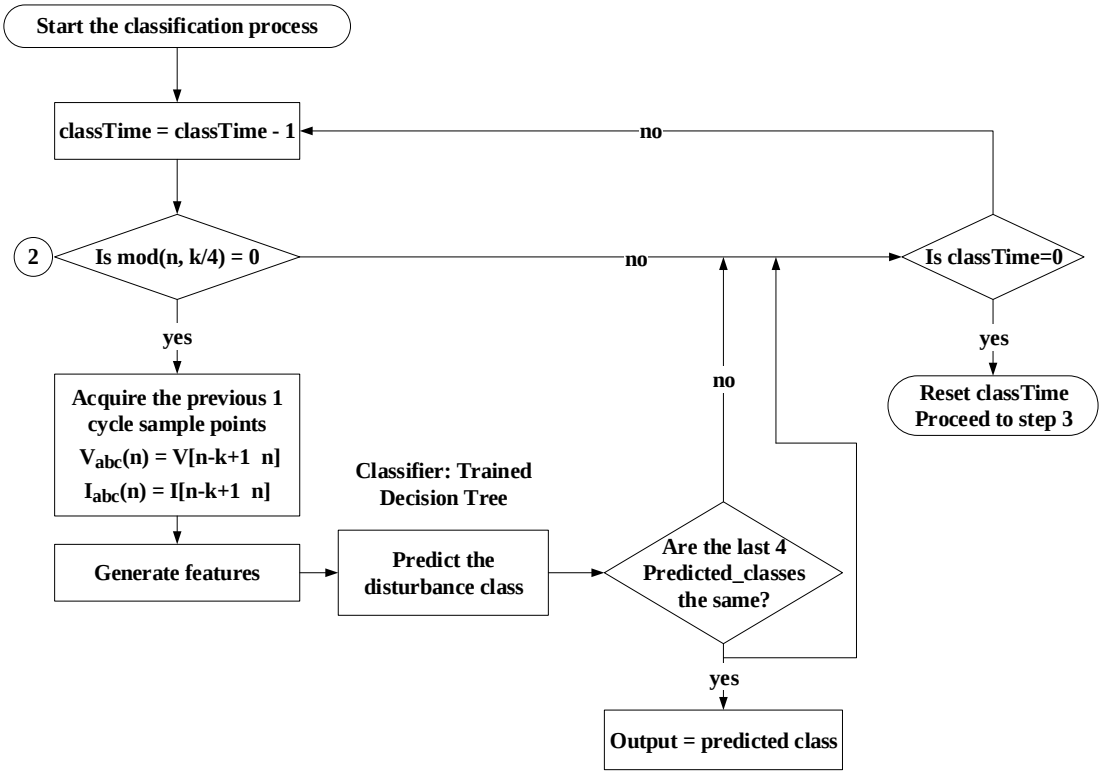

Figure 5.6 Flowchart of the classification

5.3.2 Step 3: Dead time after initial classification

At this stage, a dead time of ten cycles is introduced in which no computation is done. The algorithm does not search for a new disturbance, and this stage is achieved with the use of a counter. It is assumed that the ferroresonance transient will last for ten cycles (based on simulated data), after which the sustained ferroresonance can be classified correctly. For a ferroresonance signal, the waveform could alternate between different modes. The classification in this thesis is based on the sustained period; the author does not consider that transient signals as input to the classification algorithm. During the first few cycles, some of the modes are classified as QP or chaotic ferroresonance. This is because the signals have some non-periodic intervals before settling to the sustained modes. Considering the arcing fault signal, the minimum de-ionization interval is given in equation (3.31). This shows that the arcing signal last for more than ten cycles, therefore a dead time of ten cycles is acceptable. At the end of the pre-set time, step one is initiated again. This is to reconfirm the presence of the disturbance after the dead period. When the disturbance is still present, classification is done again for a shorter window. This process is shown in Figure 5.7 where deadTime indicates the period of no computation.

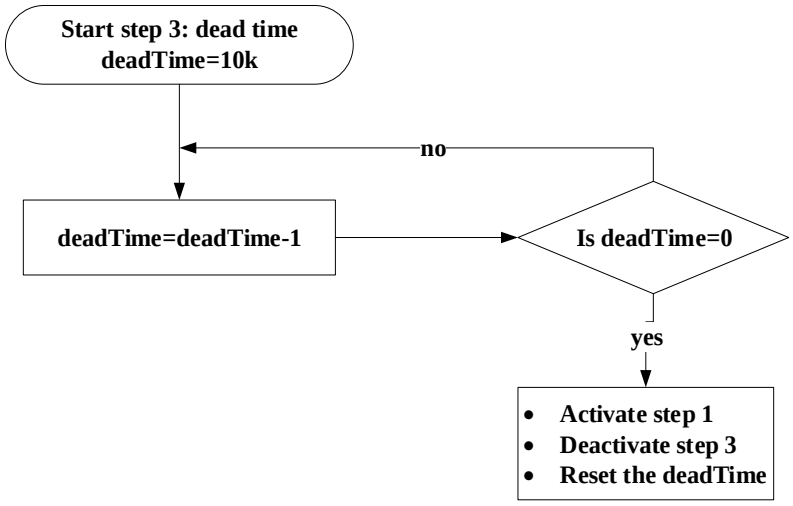

Figure 5.7 Flowchart showing Step 3: the duration of no computation

5.3.3 Step 4: Adaptive dead time for ferroresonance signal

After the first dead time in step 3, an adaptive dead period is set for the arcing and the ferroresonance detection. After the general dead time of ten cycles for all disturbances, a dead time of five cycles is proposed for ferroresonance. The five cycles dead time reduces the redundant data generation. This is because the sustained period especially for fundamental ferroresonance does not change unless there is a change in the system configuration like introducing external losses or switching off the source. This step is activated only after the first dead time elapsed and if the last predicted signal is ferroresonance. Otherwise step 5 is activated. The flow chart in Figure 5.8 shows the proposed dead time implementation while Figure 5.9 depicts the signal progression at each step during ferroresonance detection and classification.

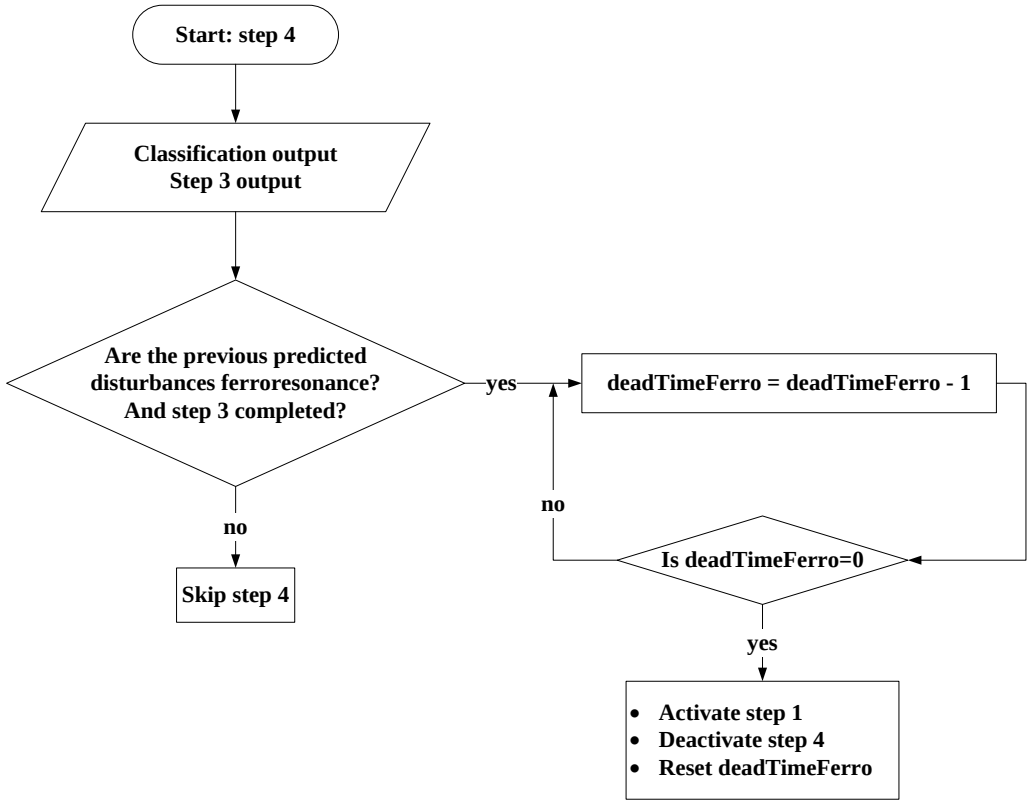

Figure 5.8 Adaptive dead time for ferroresonance classification

After the point marked h_2 Figure 5.9, the dead time of five cycles is continuously applied for n times (user specific) after which the algorithm is terminated. The process can also be terminated at h_2 depending on what the user wants; the algorithm is flexible.

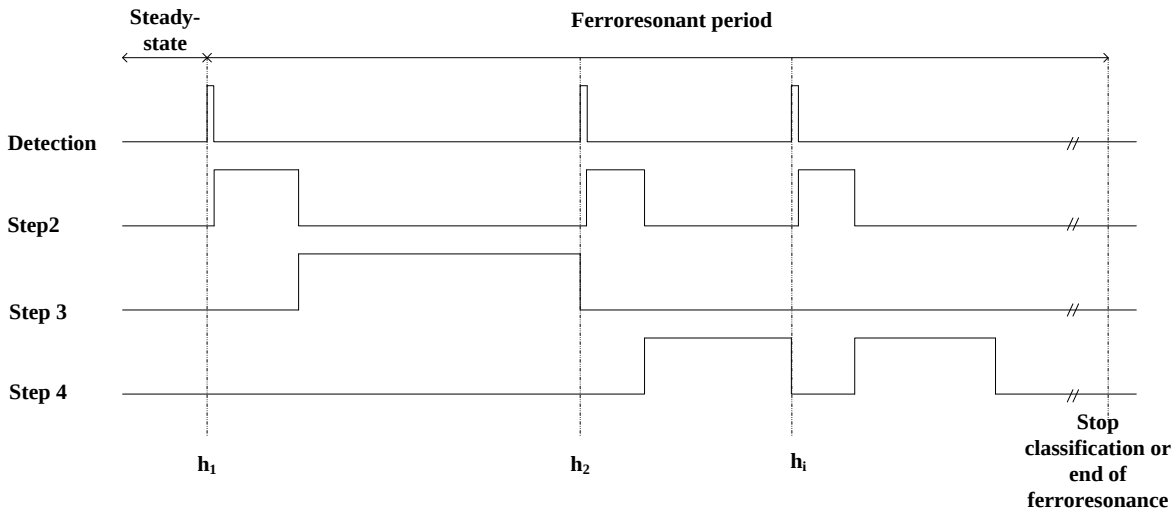

Figure 5.9 Adaptive ferroresonant classification and detection to reduce computational burden

5.3.4 Step 5: Adaptive dead time and classification window for arcing faults

A dead time of two cycles is proposed for the arcing fault signal to ensure fast detection of arc extinction. This is implemented in a similar way as done in step 4. The flow chart for the dead time implementation is shown in Figure 5.10. The signal progression during the detection and classification of the arcing fault

is shown in Figure 5.11 where L_2 is the initial classification window, L_3 is the first dead time and L_5 is the duration of adaptive arcing dead time.

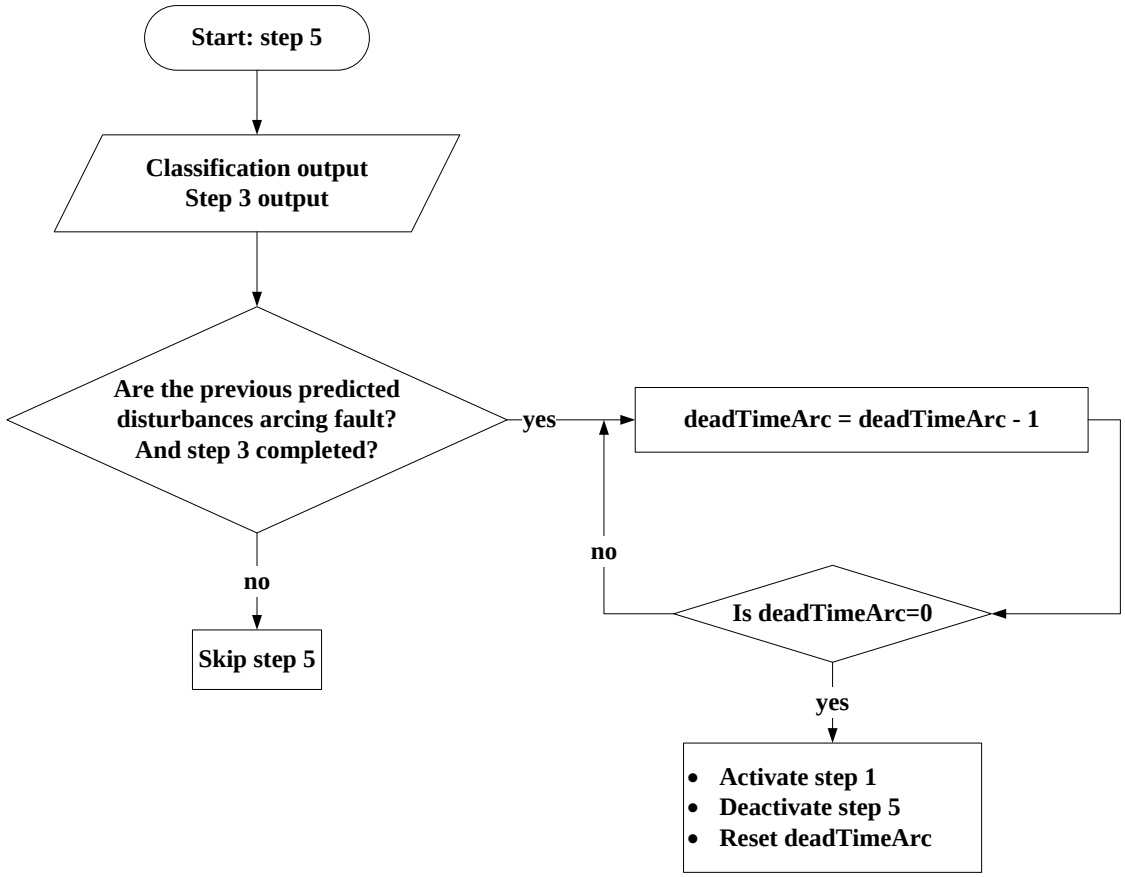

Figure 5.10 Adaptive dead time for arcing fault classification

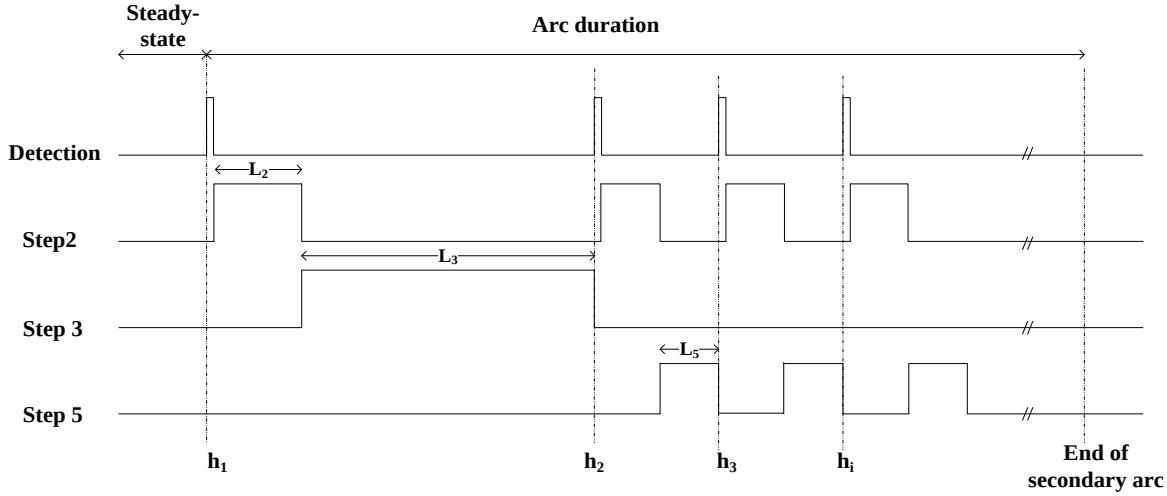

Figure 5.11 Adaptive arc detection and classification scheme

Assuming *k* is the number of samples per window size, the detection and the classification algorithm is summarized as follows:

1. Compute $|\Delta I|$ and $|\Delta V|$ at current time step *h*
2. Compare the values of $|\Delta I|$ and $|\Delta V|$ to the pre-set thresholds in order to detect the occurrence of a disturbance. When this presents a value above the threshold up to $h + \frac{k}{10}$ sample points, the

classification algorithm is activated. The algorithm stops the search for a new disturbance inception during this period.

3. The classification is done for a period of 3*k* sample points. New features are extracted four times for each window; they are presented as input to the classifier in order to obtain a unique predicted disturbance per window size. This results in three different outputs during the classification interval.
4. A dead time of ten cycles is proposed after the first classification interval in which no computation is done. At the end of this period, the existence of disturbance is checked again by comparing $|\Delta I|$ and $|\Delta V|$ to the threshold. When the disturbance is detected, the steps described in number 3 are repeated. Otherwise the other steps in the algorithm are aborted. If step 3 is repeated after the dead time, the classified disturbance group (arcing fault or ferroresonance) determines the next step. The classification is done for a period of $2k$ after this stage.
5. If the disturbance from the step described in number 4 is ferroresonance, a dead time of 5*k* is applied. This is followed by step 1 and then step 2 repeatedly for n times, the presence of the disturbance is checked at the end of each steps. The number of times n is flexible and can be changed depending on the system and user. The classification process is terminated afterwards. The algorithm is designed for monitoring purpose, the disturbance can be terminated earlier in the loop depending on what the user wants.
6. However, if the disturbance from the step described in number 4 is an arcing fault, a dead time of 2*k* is applied. Before the start of each dead time, the sum of the superimposed component of the zero-sequence current is compared to a threshold. This is followed by step 1 and then step 2 repeatedly until no disturbance is detected in step 1.

5.4 Testing the algorithm and system evaluation

The classification error is analyzed using the formula

$$P = \sum_{i}^{n} P(\omega_i) \frac{m_i}{N_i} \tag{5.9}$$

where m_i is the number of misclassified vectors and N_i is the total number of vectors from class ω_i. The confusion matrix in Figure 5.5 extracted from MATLAB after training the classifier presents a value of $P = 0$ for all classes except the three-phase fundamental ferroresonance and the three-phase chaotic ferroresonance. This shows that the classifier is accurate enough to classify the disturbances. Additional evaluation is done with separate signals to verify the result obtained from the training process and to validate the adaptive timing. The results are presented below.

Figure 5.12 presents the result obtained when the fundamental ferroresonance signal is tested with proposed algorithm. Each step is activated when the value is 1 otherwise, it is not active. As can be observed from Figure 5.12, the adaptive dead time for ferroresonance is initiated after the general dead time of length 10*k* samples period. The obtained signal is similar to the signal progression presented in Figure 5.9. The arcing dead time presents a value of zero for this test because the detected disturbance is ferroresonance.

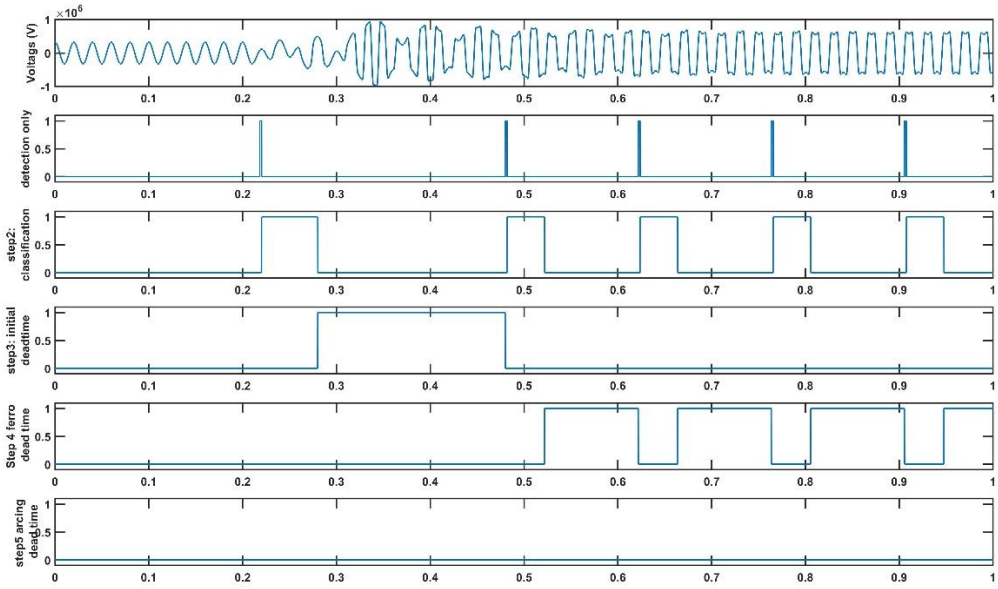

Figure 5.12 Algorithm evaluation with fundamental ferroresonance signal

As stated earlier, the first few cycles of fundamental ferroresonance are classified as quasi-periodic ferroresonance as shown in Figure 5.13

```
fault is 3 phase Quasi-periodic ferro at 0.240
fault is 3 phase Quasi-periodic ferro at 0.260
fault is 3phase fundamental ferro at 0.500
fault is 3phase fundamental ferro at 0.520
fault is 3phase fundamental ferro at 0.640
fault is 3phase fundamental ferro at 0.660
fault is 3phase fundamental ferro at 0.785
fault is 3phase fundamental ferro at 0.805
fault is 3phase fundamental ferro at 0.925
fault is 3phase fundamental ferro at 0.945
```

Figure 5.13 Classification result: Fundamental ferroresonance

Figure 5.14 and Figure 5.15 present the evaluation of the algorithm with an arcing fault signal.

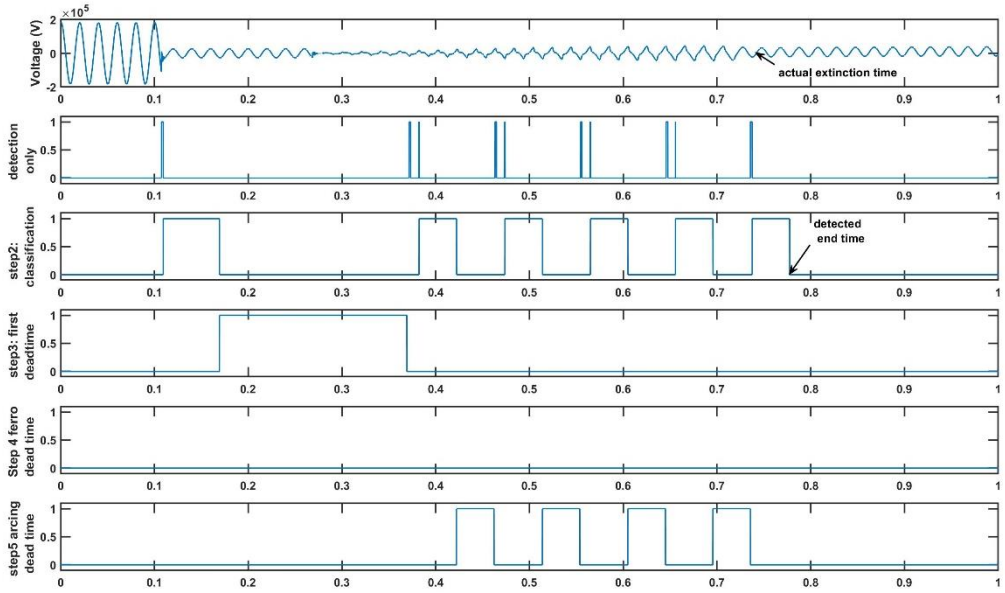

Figure 5.14 Algorithm evaluation with arcing fault signal

The actual arc extinction time is 0.7410 s while the proposed algorithm extinction time is 0.775 s. This is equivalent to 34 ms which can be further improved by reducing the dead time. This can be reduced by checking for disturbance (step 1) beginning of every cycle.

```
fault is secondary arc on phaseA at 0.145
fault is secondary arc on phaseA at 0.165
fault is secondary arc on phaseA at 0.400
fault is secondary arc on phaseA at 0.420
fault is secondary arc on phaseA at 0.490
fault is secondary arc on phaseA at 0.510
fault is secondary arc on phaseA at 0.585
fault is secondary arc on phaseA at 0.605
fault is secondary arc on phaseA at 0.675
fault is secondary arc on phaseA at 0.695
fault is secondary arc on phaseA at 0.755
fault is secondary arc on phaseA at 0.775
```

Figure 5.15 Classification result: Fundamental ferroresonance

5.5 Conclusion

The proposed algorithm, which uses a DT with an accuracy of 99.8 %, is able to detect and classify ferroresonance and arcing faults with good results and performance. The fast prediction speed and low memory requirement makes the trained DT a convenient choice for real-time applications. The adaptive dead time adopted in the algorithm helps in reducing the computational burden and redundant data. The algorithms developed for features extraction, dataset generation and classification can be expanded with new data. The algorithm is flexible and easy to use. It should be noted that the same conditions used for generating the features for training the DT must be used in the testing phase to avoid classification error.

6 Conclusions and Recommendations

The main objective of this research is to develop an algorithm that can detect ferroresonance and arcing faults. The proposed algorithm is based on the application of the DWT and pattern recognition in detecting and classifying the disturbances. It is crucial to understand these phenomena in order to detect them, therefore, EMTP models of the disturbances are used for comprehensive study of their major attributes and for data extraction. The parameters of an existing three phase ferroresonance model in ATPDraw are changed to generate different modes of ferroresonant oscillations. The simulation results show the impact of source voltage, capacitance and resistance on ferroresonance modes and are discussed in detail. The four common modes of ferroresonance discussed are fundamental, subharmonic, chaotic and quasi-periodic ferroresonance. The frequency spectrum of the voltage and current signals are used to categorize the signals into different ferroresonant modes. The best defense against this disturbance occurrence is to avoid system configurations that support the formation of a ferroresonant circuit.

A model of the primary and secondary arc when a single phase to ground fault occurs on phase A is modelled in ATP-EMTP. The interaction between the arc phenomenon and the power network has been studied in ATPDraw by using TACS devices and black-box thermal arc equations programmed in MODELS language. The results obtained from the arc model are verified by comparing with the experimental results published in literature. Therefore, the model captures the characteristics of a primary and secondary arc phenomenon.

Features are extracted from the DWT coefficients of the three-phase voltage and current signals and their zero-sequence components. The time localization property of DWT is utilized in the algorithm to indicate the disturbance inception time and progression over its duration. This is not possible with FFT. This successful time localization can give more insight on the average duration of arcing faults and can be utilized in further improvement of the adaptive timing of the SPAR. In order to optimize the algorithm and further reduces the computational burden, the absolute value of the superimposed component of voltage and current are compared to a pre-set threshold to detect the disturbance inception. As such, the DWT, feature extractions and classification are initiated when the disturbance is detected. This makes the proposed algorithm appropriate for real-time application where the computation burden is crucial.

These features are further processed to reduce the dimensionality through series of training and testing of the classifier in MATLAB. The reduced feature space reduces the execution time of the code and thus reduces the computational burden during the detection and the classification of the disturbances. The database generated is divided into 2 sets, 75 % for training and 25 % for testing and evaluation of the trained classifier. After series of training and tuning of several classifiers, the decision tree with an accuracy of 99.8 % is selected as the proposed classifier. Its fast prediction speed, simplicity, overall accuracy and small memory requirement makes it a convenient choice for a real-time application.

A step-wise implementation and adaptive dead-time has been proposed to reduce redundant data and save computational space. An adaptive time of two cycles has been proposed for arcing faults while five cycles is proposed ferroresonance. Aside from the classifier evaluation with 25 % test dataset, the full algorithm has been tested with more than 20 cases of disturbances having a combination of steady-state and post fault data. For all cases, the algorithm detected the transient inception in less than a cycle, and subsequently classified them correctly. This further verified the performance of the classifier. The

method shows a high accuracy in detecting the disturbances with the trained classifier. A reduced computational speed is observed when the adaptive time is longer. The method is flexible and can easily accommodate more phenomenon without memory increase. The conclusions highlighted below can be drawn from this research work:

- The algorithm is able to detect and classify the disturbances within 100 ms.
- The adaptive time is successfully applied to ferroresonance and arcing signal.
- The extinction time of secondary arc is detected with maximum of three cycles delay.
- The computational memory is reduced by increasing the dead time interval.
- The classification accuracy of 99.8 % is observed during system evaluation in MATLAB.

6.1 Recommendations and Future work

The following points are suggested as follow up works for this project:

- The detection and classification algorithm should be expanded to include other faults like high impedance faults.
- The proposed algorithm should be validated with real measurements.
- Frequency spectrum of the ferroresonant signals are used for the classification of ferroresonant modes in this thesis. The other available options like bifurcation diagram, Poincare method should be explored for distinguishing subharmonic, quasi-periodic and chaotic ferroresonance.

References

[1] J.-h. Yang, H.-y. Fang, R.-c. Zhang and K. Yang, "An arc fault diagnosis algorithm using multiinformation fusion and support vector machines," *Royal Society open science*, vol. 5, no. 9, p. 180160, 2018.

[2] Z. Ali, "Development of numerical algorithms for ferroresonance monitoring," in *Doctoral thesis. The University of Manchester, Faculty of Engineering and Physical Science* , 2015.

[3] CIGRE Working Group C4.307, Resonance and Ferroresonance in Power Networks, CIGRE, 2014.

[4] G. Preston, "The location and analysis of arcing faults on overhead transmission lines using synchronized measurement technology," 2012.

[5] J. F. Piñeros, J. A. Vélez and D. Rodr\'\iguez, "Ferroresonance in a 115 kV Network due to a Single Line Fault," in *International Conference on Power Systems Transients*, 2015.

[6] S. P. Ang, "Ferroresonance simulation studies of transmission systems," 2010.

[7] P. Boucherot, "{\'E}xistence de deux r{\'e}gimes en ferror{\'e}sonance," *Rev. Gen. de L'{\'E}lec*, vol. 8, no. 24, pp. 827--828, 1920.

[8] D. A. N. Jacobson, "Examples of ferroresonance in a high voltage power system," in *2003 IEEE Power Engineering Society General Meeting (IEEE Cat. No. 03CH37491)*, 2003.

[9] B. A. Mork, "Understanding and dealing with ferroresonance," 2006.

[10] P. Ferracci, "Ferroresonance–Cahier technique Schneider no. 190," *Groupe Schneider*, 1998.

[11] N. a. P. B. a. O. H. Thanomsat, "Analysis of Ferroresonance Phenomenon in 22 kV Distribution System with a Photovoltaic Source by PSCAD/EMTDC," *Energies*, vol. 11, no. 7, p. 1742, 2018.

[12] S. P. Ang, Z. D. Wang, P. Jarman and M. Osborne, "Power transformer ferroresonance suppression by shunt reactor switching," in *2009 44th International Universities Power Engineering Conference (UPEC)*, 2009.

[13] G. Mokryani, P. Siano and A. Piccolo, "Identification of ferroresonance based on S-transform and support vector machine," *Simulation Modelling Practice and Theory*, vol. 18, no. 9, pp. 1412-1424, 2010.

[14] G. Mokryani, M.-R. Haghifam and J. Esmaeilpoor, "Identification of ferroresonance based on wavelet transform and artificial neural network," *European Transactions on Electrical Power*, vol. 19, no. 3, pp. 474-486, 2009.

[15] S. Beheshtaein, "Application of wavelet-base method and DT in detection of ferroresonance from other transient phenomena," in *2012 International Symposium on Innovations in Intelligent Systems and Applications*, 2012.

[16] B. Zhang and T. Lu, "On the use of wavelet decomposition for ferroresonance detection in power system," in *2009 Asia-Pacific Power and Energy Engineering Conference*, 2009.

[17] G. Mokryani and M.-R. Haghifam, "Application of wavelet transform and MLP neural network for Ferroresonance identification," in *2008 IEEE Power and Energy Society General Meeting-Conversion and Delivery of Electrical Energy in the 21st Century*, 2008.

[18] M. V. Escudero, I. Dudurych and M. A. Redfern, "Characterization of ferroresonant modes in HV substation with CB grading capacitors," *Electric Power Systems Research,* vol. 77, no. 11, pp. 1506-1513, 2007.

[19] D. A. N. Jacobson, D. R. Swatek and R. W. Mazur, "Mitigating potential transformer ferroresonance in a 230 kV converter station," in *Proceedings of 1996 Transmission and Distribution Conference and Exposition*, 1998.

[20] Wikipedia, *Arc Flash.*

[21] N. I. Elkalashy and others, Modeling and detection of high impedance arcing fault in medium voltage networks, Helsinki University of Technology, 2007.

[22] A. A. Montanari, M. C. Tavares, C. M. Portela and A. Câmara, "Secondary arc voltage and current harmonic content for field tests results," in *Proc. 2009 International Conference on Power Systems Transients*, 2009.

[23] V. V. Terzija and H.-J. Koglin, "On the modeling of long arc in still air and arc resistance calculation," *IEEE Transactions on Power Delivery,* vol. 19, no. 3, pp. 1012-1017, 2004.

[24] G. Bizjak, P. Zunko and D. Povh, "Circuit breaker model for digital simulation based on Mayr's and Cassie's differential arc equations," *IEEE Transactions on Power Delivery*, vol. 10, no. 3, pp. 1310-1315, 1995.

[25] V. Terzija, G. Preston, M. Popov and N. Terzija, "New static “airarc” EMTP model of long arc in free air," *IEEE Transactions on Power Delivery,* vol. 26, no. 3, pp. 1344-1353, 2011.

[26] L. Prikler, G. Ban, M. Kizlicay, G. Tari, A. Tombor and J. Zerenyi, "Influence of the Secondary Arc on the Operation of Single Phase Autoreclosure of the 400 kV interconnection between Hungary and Croatia," *Energija,* vol. 59, no. 1-4, p. 0, 2010.

[27] A. A. Montanari, M. C. Tavares and C. M. Portela, "Adaptative single-phase autoreclosing based on secondary arc voltage harmonic signature," *parameters,* vol. 6, p. 7, 2009.

[28] S. Dadda, T. Bouthiba and S. Seghir, "Primary Arc Modeling in Transmission Line," in *2018 International Conference on Electrical Sciences and Technologies in Maghreb (CISTEM)*, 2018.

[29] Q. Lu, Z. Ye, Y. Zhang, T. Wang and Z. Gao, "Analysis of the Effects of Arc Volt–Ampere Characteristics on Different Loads and Detection Methods of Series Arc Faults," *Energies,* vol. 12, no. 2, p. 323, 2019.

[30] Q. Lu, T. Wang, B. He, T. Ru and D. Chen, "A new series arc fault identification method based on wavelet transform," in *IECON 2017-43rd Annual Conference of the IEEE Industrial Electronics Society*, 2017.

[31] P. Muller, S. Tenbohlen, R. Maier and M. Anheuser, "Characteristics of series and parallel low current arc faults in the time and frequency domain," in *2010 Proceedings of the 56th IEEE Holm Conference on Electrical Contacts*, 2010.

[32] A. Lazkano, J. Ruiz, L. A. Leturiondo and E. Aramendi, "High impedance arcing fault detector for three-wire power distribution networks," in *2000 10th Mediterranean Electrotechnical Conference. Information Technology and Electrotechnology for the Mediterranean Countries. Proceedings. MeleCon 2000 (Cat. No. 00CH37099)*, 2000.

[33] H. W. (Louis), "Study of High Impedance Fault Characteristics and Detection," Master thesis. School of Electrical Engineering and Telecommunications, Sydney, Australia, 2015.

[34] L. der Sluis, Transients in power systems, John Wiley & Sons, 2001.

[35] L. Prikler, M. Kizilcay, G. Bán and P. Handl, "Improved secondary arc models based on identification of arc parameters from staged fault test records," in *14th PSCC,* 2002.

[36] M. Kizilcay and T. Pniok, "Digital simulation of fault arcs in power systems," *European Transactions on Electrical Power,* vol. 1, no. 1, pp. 55-60, 1991.

[37] H. Wihartady, "Modeling of short circuit fault arc in 150 kV system and its influence on the performance of distance protection," 2009.

[38] T. Gonen, Electrical power transmission system engineering: analysis and design, CRC press, 2015.

[39] J. L. Blackburn and T. J. Domin, Protective relaying: principles and applications, CRC press, 2014.

[40] MATLAB, *Fast Fourier transform.*

[41] Wikipedia, *Daubechies wavelet.*

[42] R. Polikar, "The wavelet tutorial part iii," IOWA State University, USA.

[43] S. C. Shiralashetti, "An application of the Daubechies Orthogonal Wavelets in Power system Engineering," *International Journal of Computer Applications,* vol. 975, p. 8878, 2014.

[44] H. A. Darwish, M. H. Farouk, A. I. Taalab and N. M. Mansour, "Investigation of real-time implementation of DSP-based DWT for power system protection," in *IEEE/PES Transmission and Distribution Conference and Exposition*, 2006.

[45] J. Morlet, "Sampling theory and wave propagation," *Geophysics*, vol. 47, pp. 203-236, 1982.

[46] S. Santoso, E. J. Powers, W. M. Grady and P. Hofmann, "Power quality assessment via wavelet transform analysis," *IEEE transactions on Power Delivery,* vol. 11, no. 2, pp. 924-930, 1996.

[47] L. Angrisani, P. Daponte, M. D'apuzzo and A. Testa, "A measurement method based on the wavelet transform for power quality analysis," *IEEE Transactions on Power Delivery,* vol. 13, no. 4, pp. 990-998, 1998.

[48] S. Santoso, E. J. Powers and W. M. Grady, "Power quality disturbance data compression using wavelet transform methods," *IEEE Transactions on Power Delivery,* vol. 12, no. 3, pp. 1250-1257, 1997.

[49] T. Croes, C. Gherasim, J. den Keybus, J. Ghijselen, J. Driesen and R. Belmans, "Power measurement using the wavelet transform of analytic signals," in *2004 11th International Conference on Harmonics and Quality of Power (IEEE Cat. No. 04EX951)*, 2004.

[50] W.-K. Yoon and M. J. Devaney, "Power measurement using the wavelet transform," *IEEE Transactions on Instrumentation and Measurement,* vol. 47, no. 5, pp. 1205-1210, 1998.

[51] C. H. Kim and R. Aggarwal, "Wavelet transforms in power systems. II. Examples of application to actual power system transients," *Power Engineering Journal,* vol. 15, no. 4, pp. 193-202, 2001.

[52] D. C. Robertson, O. I. Camps, J. S. Mayer and W. B. Gish, "Wavelets and electromagnetic power system transients," *IEEE Transactions on Power Delivery,* vol. 11, no. 2, pp. 1050-1058, 1996.

[53] W. A. Wilkinson and M. D. Cox, "Discrete wavelet analysis of power system transients," *IEEE Transactions on Power systems,* vol. 11, no. 4, pp. 2038-2044, 1996.

[54] I. Baqui, I. Zamora, J. Mazón and G. Buigues, "High impedance fault detection methodology using wavelet transform and artificial neural networks," *Electric Power Systems Research,* vol. 81, no. 7, pp. 1325-1333, 2011.

[55] C.-H. Kim, H. Kim, Y.-H. Ko, S.-H. Byun, R. K. Aggarwal and A. T. Johns, "A novel fault-detection technique of high-impedance arcing faults in transmission lines using the wavelet transform," *IEEE Transactions on Power Delivery,* vol. 17, no. 4, pp. 921-929, 2002.

[56] T. M. Lai, L. A. Snider, E. Lo and D. Sutanto, "High-impedance fault detection using discrete wavelet transform and frequency range and RMS conversion," *IEEE Transactions on Power Delivery*, vol. 20, no. 1, pp. 397-407, 2005.

[57] A.-R. Sedighi, M.-R. Haghifam, O. P. Malik and M.-H. Ghassemian, "High impedance fault detection based on wavelet transform and statistical pattern recognition," *IEEE Transactions on Power Delivery*, vol. 20, no. 4, pp. 2414-2421, 2005.

[58] P.-Y. Guo, C.-Z. Li, S. Yan, J. Liangcheng and J.-Y. Zhang, "Application of wavelet transform in ferroresonance detection," in *2011 2nd International Conference on Artificial Intelligence, Management Science and Electronic Commerce (AIMSEC)*, 2011.

[59] MATLAB, *Fast Wavelet Transform (FWT) Algorithm.*

[60] S. G. Mallat, "A theory for multiresolution signal decomposition: the wavelet representation," *IEEE Transactions on Pattern Analysis & Machine Intelligence*, no. 7, pp. 674-693, 1989.

[61] "Pattern Recognition," in *Power Systems Signal Processing for Smart Grids*, John Wiley & Sons, Ltd, 2014, pp. 321-354.

[62] P. H. a. S. Swain, "Using superimposed principles (Delta) in protection techniques in an increasingly challenging power network," in *2017 70th Annual Conference for Protective Relay Engineers (CPRE)*, Texas, 2017.